



National Library
of Canada

Bibliothèque nationale
du Canada

Canadian Theses Service

Service des thèses canadiennes

Ottawa, Canada
K1A 0N4

NOTICE

The quality of this microform is heavily dependent upon the quality of the original thesis submitted for microfilming. Every effort has been made to ensure the highest quality of reproduction possible.

If pages are missing, contact the university which granted the degree.

Some pages may have indistinct print especially if the original pages were typed with a poor typewriter ribbon or if the university sent us an inferior photocopy.

Reproduction in full or in part of this microform is governed by the Canadian Copyright Act, R.S.C. 1970, c. C-30, and subsequent amendments.

AVIS

La qualité de cette microforme dépend grandement de la qualité de la thèse soumise au microfilmage. Nous avons tout fait pour assurer une qualité supérieure de reproduction.

S'il manque des pages, veuillez communiquer avec l'université qui a conféré le grade.

La qualité d'impression de certaines pages peut laisser à désirer, surtout si les pages originales ont été dactylographiées à l'aide d'un ruban usé ou si l'université nous a fait parvenir une photocopie de qualité inférieure.

La reproduction, même partielle, de cette microforme est soumise à la Loi canadienne sur le droit d'auteur, SRC 1970, c. C-30, et ses amendements subséquents.

**Noncontact Position and Orientation Measurement
Techniques for Real-Time Systems**

Nicholas Krouglicof

**A Thesis
in
The Department
of
Mechanical Engineering**

**Presented in Partial Fulfilment of the Requirements
for the Degree of Doctor of Philosophy at
Concordia University
Montreal, Quebec, Canada**

February 1991

© Nicholas Krouglicof, 1991



National Library
of Canada

Bibliothèque nationale
du Canada

Canadian Theses Service Service des thèses canadiennes

Ottawa, Canada
K1A 0N4

The author has granted an irrevocable non-exclusive licence allowing the National Library of Canada to reproduce, loan, distribute or sell copies of his/her thesis by any means and in any form or format, making this thesis available to interested persons.

The author retains ownership of the copyright in his/her thesis. Neither the thesis nor substantial extracts from it may be printed or otherwise reproduced without his/her permission.

L'auteur a accordé une licence irrévocable et non exclusive permettant à la Bibliothèque nationale du Canada de reproduire, prêter, distribuer ou vendre des copies de sa thèse de quelque manière et sous quelque forme que ce soit pour mettre des exemplaires de cette thèse à la disposition des personnes intéressées.

L'auteur conserve la propriété du droit d'auteur qui protège sa thèse. Ni la thèse ni des extraits substantiels de celle-ci ne doivent être imprimés ou autrement reproduits sans son autorisation.

ISBN 0-315-64644-6

Canada

ABSTRACT

Noncontact Position and Orientation Measurement Techniques for Real-Time Systems

Nicholas Krouglicof, Ph.D.

Concordia University, 1991.

The need to accurately determine the position and orientation of a rigid body in space arises in a number of disciplines. In the field of robotics, for example, many researchers have realized the implications of precise noncontact measurement with regard to manipulator design and control.

This thesis reviews the difficulties inherent in acquiring accurate spatial information in real-time from conventional image sensors. The fundamental performance limiting factors such as spatial resolution, photon noise, target contrast, and volume of data to be processed are discussed. A novel sensor which satisfies the conflicting requirements of high accuracy and real-time response is then described and analyzed. The conception and design of a noncontact, six degree-of-freedom position measurement system incorporating this sensor are then presented.

As with most imaging devices, the sensor used in this study provides only enough information to compute the line of sight passing from the target point to the focal center of the lens. Additional "depth cues" are required to determine range. Two different techniques are presented.

In the case of the stereoscopic technique, the target points are viewed from two different locations and a triangulation scheme is used to determine the three-dimensional cartesian coordinates of each point. The rotational parameters which best describe the orientation of the rigid body are then determined by applying least squares analysis to an overdetermined system of equations.

An iterative technique for determining the absolute position and orientation of the rigid body from a single perspective view is also presented. This technique is based on the assumption of rigidity, that is, that the distance between any two body-fixed points remains constant independent of time or configuration.

A critical evaluation of the influence of various parameters on system performance is conducted assuming a stereoscopic approach. Based on this evaluation, techniques for improving the performance of the measurement system are presented.

ACKNOWLEDGEMENTS

The author would like to express his gratitude to his friends and thesis supervisors, Dr. J.V. Svoboda and the late Dr. M. McKinnon, for their guidance throughout his graduate studies.

The cooperation, technical assistance, and financial support of CAE Electronics Ltd. of Montreal is also highly appreciated.

TABLE OF CONTENTS

LIST OF FIGURES.....	ix
LIST OF TABLES.....	xii
NOMENCLATURE.....	xiii
 CHAPTER 1	 INTRODUCTION
1.1	General..... 1
1.2	Fiber Optic Helmet Mounted Display..... 3
1.3	Review of "Line-of-Sight" Sensing Systems.. 6
	1.3.1 Honeywell/Polhemus System..... 8
	1.3.2 Marconi System..... 10
	1.3.3 Summary..... 12
1.4	Thesis Outline..... 13
 CHAPTER 2	 MECHANICAL POSITION MEASUREMENT SYSTEM
2.1	Introduction..... 15
2.2	Translation Measurement..... 17
2.3	Rotation Measurement..... 21
2.4	Data Acquisition and Processing..... 27
2.5	Performance..... 29
 CHAPTER 3	 IMAGE SENSORS
3.1	Introduction..... 31
3.2	The Vidicon Camera..... 31
3.3	Solid-State Image Sensors..... 36
3.4	Summary..... 37
3.5	Position Sensor Head..... 38
	3.5.1 Principle of Operation..... 39
	3.5.2 Analog Position Processing Circuit.. 41
	3.5.3 Linearity..... 44
	3.5.4 Resolution..... 49
	3.5.5 Shot Noise..... 49
	3.5.6 Quantum Efficiency..... 51

3.6	Sensitivity to Modifying and Interfering Inputs.....	54
3.6.1	Background Illumination.....	54
3.6.2	Intensity of the Light Spot.....	56
3.6.3	Size of the Light Spot.....	57
3.7	Response.....	58
3.8	Summary.....	59
CHAPTER 4	OPTICAL POSITION MEASUREMENT SYSTEM - SYSTEM DESCRIPTION	
4.1	Introduction.....	60
4.2	Target Light Source.....	60
4.3	Intensity Control System.....	66
4.3.1	Light-Emitting Diode.....	66
4.3.2	N-Channel, Enhancement Mode MOSFET..	67
4.3.3	Optics and Geometry.....	73
4.3.4	Position Sensitive Detector.....	74
4.3.5	Analog Position Processing Circuit..	75
4.3.6	Control Strategy.....	75
4.4	Simulation Results.....	78
4.4.1	Nonlinear Control Strategy.....	80
4.5	System Configuration.....	86
CHAPTER 5	LENS-SENSOR MODEL	
5.1	Introduction.....	90
5.2	Perspective Geometry.....	92
5.3	Sensing Range.....	94
5.3.1	Sensing Range by Triangulation.....	95
5.4	Summary.....	102
CHAPTER 6	FORMULATION OF ALGORITHMS	
6.1	Introduction.....	104
6.2	The Rodrigues Formulas.....	107
6.3	The Vector Equation Method.....	115
6.4	The Schut Method.....	118
6.4.1	Derivation of the Schut Equations..	121
6.4.2	Solution by the Method of Least Squares.....	126
6.5	Translation Measurement.....	131

6.6	Formulation in Terms of Euler Parameters.	131
6.7	Numerical Considerations.....	134
CHAPTER 7	SINGLE CAMERA RESECTION	
7.1	Introduction.....	135
7.2	Formulation of Single-Camera Algorithm...	135
7.3	Convergence of Algorithm.....	140
CHAPTER 8	PERFORMANCE EVALUATION	
8.1	Introduction.....	142
8.2	Program Description.....	144
8.3	Analysis of Results.....	155
8.4	Experimental Results.....	157
8.5	Summary.....	158
CHAPTER 9	CONCLUSIONS AND RECOMMENDATIONS FOR FUTURE WORK	
9.1	General.....	159
9.2	Summary.....	160
9.3	Recommendations for Future Work.....	164
	9.3.1 Enhancements.....	164
	9.3.2 Applications.....	170
REFERENCES.....		172
APPENDIX 1	MECHANICAL POSITION MEASUREMENT SYSTEM: LISTING OF ROUTINES.....	183
APPENDIX 2	CALIBRATION OF POSITION SENSOR HEAD: MAP OF THE SENSITIVE SURFACE.....	188
APPENDIX 3	INTENSITY CONTROL CIRCUIT: LISTING OF THE MIMIC SIMULATION PROGRAM.....	190
APPENDIX 4	OPTICAL POSITION MEASUREMENT SYSTEM: STATISTICAL SIMULATION PROGRAM	193
APPENDIX 5	OPTICAL POSITION MEASUREMENT SYSTEM: SAMPLE CALIBRATION DATA.....	202

LIST OF FIGURES

Figure	Page
1.1 Schematic representation of the Fiber Optic Helmet Mounted Display (FOHMD).....	5
1.2 Installation Detail of Honeywell/Polhemus Helmet Position Sensing System.....	9
1.3 Block Diagram of Honeywell/Polhemus System.....	9
1.4 Installation Detail of Marconi Helmet Position Sensing System.....	11
1.5 Schematic of V Slit Camera.....	11
2.1 Schematic representation of Mechanical Position Measurement System showing fixed and movable coordinate systems.....	16
2.2 Schematic representation of coordinate transformations at Joints 1, 2, and 3.....	19
3.1 Schematic Representation of Position-Sensitive Detector (PSD).....	40
3.2 Block Diagram of the Analog Position Processing Circuit.....	42
3.3 Schematic diagram of Intensity Control Circuit used in calibration.....	47
4.1 Relative Radiant power output, Φ_{EREL} , versus wavelength, λ , for the TIES16A Light Emitting Diode.....	64
4.2 MOSFET and LED connected in the common-source configuration.....	70
4.3 Forward current, I_F , versus Gate-to-Source voltage, V_{GS} , for the LED-MOSFET combination shown in Figure 4.2.....	72
4.4 Block Diagram of the Intensity Control Circuit....	76

Figure	Page
4.5 Step Response of the Intensity Control Circuit with Proportional Control.....	79
4.6 Step Response of the Intensity Control Circuit with Integral Control.....	81
4.7 Simplified representation of circuit used to implement the nonlinear control strategy.....	83
4.8 Step Response of the Intensity Control Circuit with Nonlinear Control.....	85
4.9 Block diagram of Optical Position Measurement System.....	87
4.10a Intensity Output Signal, Σ_1 , of PSH 1.....	89
b Intensity Output Signal, Σ_2 , of PSH 2.....	89
c Position Output Signal, V_{x1} , of PSH 1.....	89
d Position Output Signal, V_{y2} , of PSH 1.....	89
5.1 Schematic representation of lens-sensor assembly..	91
5.2 General configuration of the Optical Position Measurment System.....	98
6.1 Schematic representation of Euler's theorem.....	110
6.2 Normal view of the plane PQRS.....	111
8.1 Schematic representation of the LED pattern used in this study.....	145
8.2 Two-dimensional perspective projection of the LED pattern as viewed from Sensor 1.....	146
8.3 Probability distributions generated by the simulation program for Yaw assuming 3 and 6 LEDs and a resolution of 9 bits.....	150
8.4 Probability distributions generated by the simulation program for Yaw assuming 3 and 6 LEDs and a resolution of 10 bits.....	151
8.5 Probability distributions generated by the simulation program for Yaw assuming 3 and 6 LEDs and a resolution of 11 bits.....	152

Figure		Page
9.1	Alternative sensor configuration which minimizes the number of secondary noise sources.....	166
9.2	Proposed enhancements to the Intensity Control Circuit.....	169

LIST OF TABLES

Table	Page
2.1 Performance Summary of Mechanical Position Measurement System.....	30
3.1 Calibration of Position Sensor Head: Summary of Results.....	48
7.1 Convergence of Single-Camera Algorithm.....	141
8.1 Summary of Results Obtained from the Statistical Simulation Program.....	154
A2.1 X Output Voltage Signal Recorded at 1mm Intervals across Detector Surface.....	189
A2.2 Y Output Voltage Signal Recorded at 1mm Intervals across Detector Surface.....	189
A5 Sample Calibration Data.....	203

NOMENCLATURE

$\{1, \vec{i}, \vec{j}, \vec{k}\}$	basis of a vector space V of dimension 4 over the set of real numbers
$[A]$	matrix of coefficients of rotational parameters of order $4n$ by 4
$[A], [B], [C]$	matrices of direction cosines relating adjacent coordinate systems
a_i	positive angle of rotation about the Z axis for joint i
A_p	entrance pupil area of the lens
a_R	relative aperture of the lens
B_{CL}	operational amplifier closed-loop bandwidth
b_i	positive angle of rotation about the X axis for joint i
c_i	positive angle of rotation about the Y axis for joint i
D	mark-space ratio or duty cycle
E_p	energy per incident photon
E_R	irradiance at a distance r from an ideal point source
GBW	operational amplifier gain-bandwidth product
f	frequency of incident light
G_x, G_y	sensitivity of the Position Sensor Head in the X_D and Y_D directions
h	Planck's constant (6.63×10^{-34} J / Hz)

I_D	MOSFET drain current
I_{FMAX}	maximum-rated continuous forward current for the target LED
I_F	forward current through LED-MOSFET combination
$\vec{i}_i, \vec{j}_i, \vec{k}_i$	orthogonal unit vectors of link i
I_P	magnitude of photocurrent generated by Position Sensitive Detector
I_P	peak current through target LED
J	Jacobian matrix
K	MOSFET constant: dependent on material properties and dimensions
K_I	gain of current-to-voltage converter (V/A)
K_i	gains of the various stages of the Analog Position Processing Circuit ($i=1,2,3,4$)
L_F	focal length of the lens
$[M]$	set of normal equations resulting from the matrix multiplication $[J]^T [J]$
N	number of "noise-free" bits provided by the A/D converter
\vec{n}	unit vector defining the axis of rotation of the rigid body
\bar{n}_e	mean number of electrons accumulated in a time interval Δt
\bar{n}_p	mean number of photons accumulated in a time interval Δt

q	quaternion: linear combination of the elements of the vector space $\{1, \vec{i}, \vec{j}, \vec{k}\}$
q^{-1}	reciprocal of the quaternion q
q^*	conjugate of the quaternion q
\vec{q}	vector representing the component of \vec{r} normal to \vec{n}
Q	quantum efficiency of the target LED
\bar{Q}	three-dimensional mean of the measured points
\mathcal{R}	range of uncertainty
\vec{r}	vector defining the position of the point P prior to rigid body rotation
\vec{r}'	vector defining the position of the point P after rigid body rotation
\vec{R}_1, \vec{R}_2	vector defining the position of the LED with respect to the fixed coordinate system
R_e	responsivity of the Position Sensitive Detector
$\vec{R}_{s1}, \vec{R}_{s2}$	vector defining the position of the LED with respect to the sensor coordinate system
r_s	diode series resistance
$[S]$	symmetric matrix of order four resulting from the matrix multiplication $[A]^T [A]$
S'	distance from the sensitive surface of the detector to the principle plane of the lens
$(S/N)_p$	theoretical signal to noise ratio based on photon noise

$(S/N)_s$	theoretical signal to noise ratio based on shot noise
$[T]$	matrix of direction cosines relating body coordinate system to fixed coordinate system
$[T_1], [T_2]$	matrix of direction cosines relating sensor coordinate system to fixed coordinate system
\vec{V}_B	vector joining the focal centers of the two lenses
\vec{V}_{BA}	vector representing link B of Mechanical Position Measurement System
\vec{V}_{CB}	vector representing link C of Mechanical Position Measurement System
V_{DD}	d.c. supply voltage
V_{DS}	MOSFET drain-to-source voltage
V_F	forward voltage across the target LED
V_{GS}	MOSFET gate-to-source voltage
V_{GSAT}	MOSFET gate-to-source voltage which results in saturation
V_J	junction voltage for the target LED
\vec{V}_{OC}	vector constant
V_T	MOSFET turn-on or threshold voltage
V_x, V_y	position signals generated by Analog Position Processing Circuit
V_{xi}, V_{yi}	output signals from current-to-voltage converters ($i=1,2$)

x_{D1}, y_{D1}	image coordinates of the target LED with respect to sensor i (i=1,2)
$X^{(K)}$	K^{th} approximation to the unknown parameters
α, β, γ	Euler angles commonly referred to as Yaw, Roll and Pitch
$\alpha_s, \beta_s, \gamma_s$	angles formed by the vector R and the X_s , Y_s , and Z_s axes respectively
$[\beta]$	column vector of parameters
χ^2	random variable for the Chi-Squared Test
δ_i	error term
$[\delta]$	column vector of residuals
$\overrightarrow{\Delta r}$	vector defining the displacement of the point P following the rotation of the rigid body
Δt	time interval or integration time
ϵ_i	sequence of random number uniformly distributed across the interval from 0 to 1
Φ_E	radiant power output for the target LED
Φ_{EREL}	relative radiant power output for the target LED
Φ_s	radiant flux incident on the sensitive surface of the Position Sensitive Detector
η	quantum efficiency of the Position Sensitive Detector
λ	wavelength of incident light

θ	angle of rotation about the unit vector \vec{n}
$\vec{\rho}$	Rodrigues vector: direction \vec{n} , magnitude $\text{TAN}(\theta/2)$
Σ	intensity signal generated by Analog Position Processing Circuit
Σ_{SP}	intensity setpoint
σ_e	sample standard deviation
τ	time constant of low-pass filter
τ	transmittance of the lens-filter combination
τ_A	operational amplifier time constant
τ_D	time constant of the Position Sensitive Detector

CHAPTER 1

INTRODUCTION

1.1 General

Determining the position and orientation of a rigid body in space is a critical task with many applications, particularly if it can be accomplished with minimal delays and with a high degree of accuracy. One potential application is in the field of robotics.

Conventional robot control strategies rely on a kinematic model to predict the end-effector position and orientation from the joint angles. Secondary considerations such as gear backlash, friction, link compliance, encoder resolution, and manufacturing errors are generally neglected. As a direct result, industrial robots are designed to be highly accurate and repeatable to match assembly tolerances [1,2].

Many researchers have studied kinematic modeling, identification, and control of industrial robots in an effort to improve positioning accuracy. Sensory feedback techniques, however, offer the greatest potential. If, for example, the position and orientation of the robot's end-effector could be precisely measured and rapidly fed back to the robot control computer, a potentially lighter,

more compliant robot could be realized without sacrificing repeatability or positioning accuracy. The greatest difficulty to date has been the accurate, real-time measurement of the end-effector's position and orientation.

In the area of flight simulator visual systems, a recent trend is towards high resolution, area-of-interest displays which are head (or, ideally, eye) slaved. Such displays need only project the "instantaneous" image currently within the pilot's field of view. This approach significantly reduces the amount of imagery which must be generated at any instant. However, in order for the image to appear stationary in spite of head movements, the position and orientation of the pilot's helmet must be known in all six degrees-of-freedom, with a resolution comparable to the acuity of the human eye, and at a frame rate at least equal to that of the image generator (60 hz).

This thesis focuses on precise noncontact position and orientation measurement techniques for such exacting applications. The original motivation behind this work was noncontact measurement for an area-of-interest display. Consequently, helmet tracking remains the primary application addressed in this thesis. Since the performance criteria are particularly rigorous, both in terms of accuracy and speed, helmet tracking is a suitable case study. Other considerations are primarily environmental

(i.e. how the system behaves under different ambient lighting conditions or in a poorly controlled industrial environment). Such considerations are significant and will be addressed.

1.2 Fiber Optic Helmet Mounted Display

Simulation of the view, as seen by the pilot through the windscreens of a cockpit, is the most difficult problem in simulation technology. Commercial aircraft simulators with computer generated imagery displayed on one or more Cathode Ray Tubes (CRTs) have reached a satisfactory stage of development and are now widely used. However, the simulation of a wide field of view of terrain in high detail as is needed for air-to-air combat training remains a difficult and expensive problem [3].

The current approach to providing high resolution, wide field of view display is to split the field between a number of displays surrounding the pilot. Each display requires its own channel of computer image generation. Images of equal quality must be generated in each display regardless of where the pilot is looking. This is costly both in terms of hardware and computer time. By projecting the image directly onto the visor of the pilot's helmet, a significant cost saving can be realized. Since the field of view is greatly

reduced, both the quality of the image (i.e. resolution) and the frame rate can be improved. The field of view is head slaved in order to provide an image which is instantaneously limited to the pilot's viewing area but can be redirected to permit the pilot to look in any direction. A further development is to track eye position or point of regard and provide a high resolution insert slaved to the eye's foveal area. In such a system, the pilot perceives high resolution imagery wherever he looks, but instantaneously the system is only required to produce images over a 15° cone.

Supported by a joint U.S./Canada cost sharing program, CAE Electronics Ltd. of Montreal has developed the Fiber Optic Helmet Mounted Display (FOHMD) which provides high resolution imagery over what is effectively an extremely wide field of view. The prototype system was integrated into the Combat Mission Trainer at the Human Resources Laboratory of Williams Air Force Base in Arizona.

Figure 1.1 illustrates the FOHMD developed by CAE. High resolution General Electric Lightvalves project full colour computer generated images through coherent fiber optic cables to the helmet mounted Pancake Windows®. The Pancake Windows provide the pilot with a collimated view of the "virtual" world which is combined with the direct view of internal cockpit. The instantaneous field of view is comparable to that available to the pilot wearing a standard

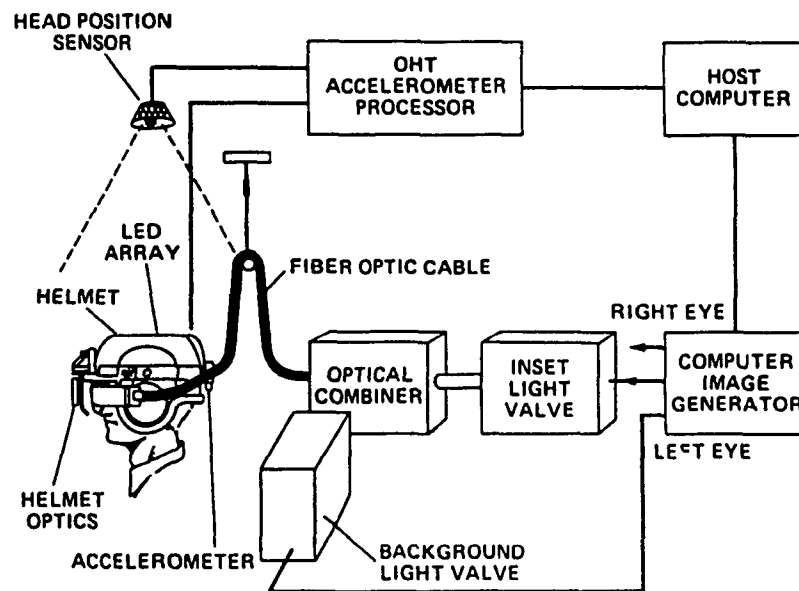
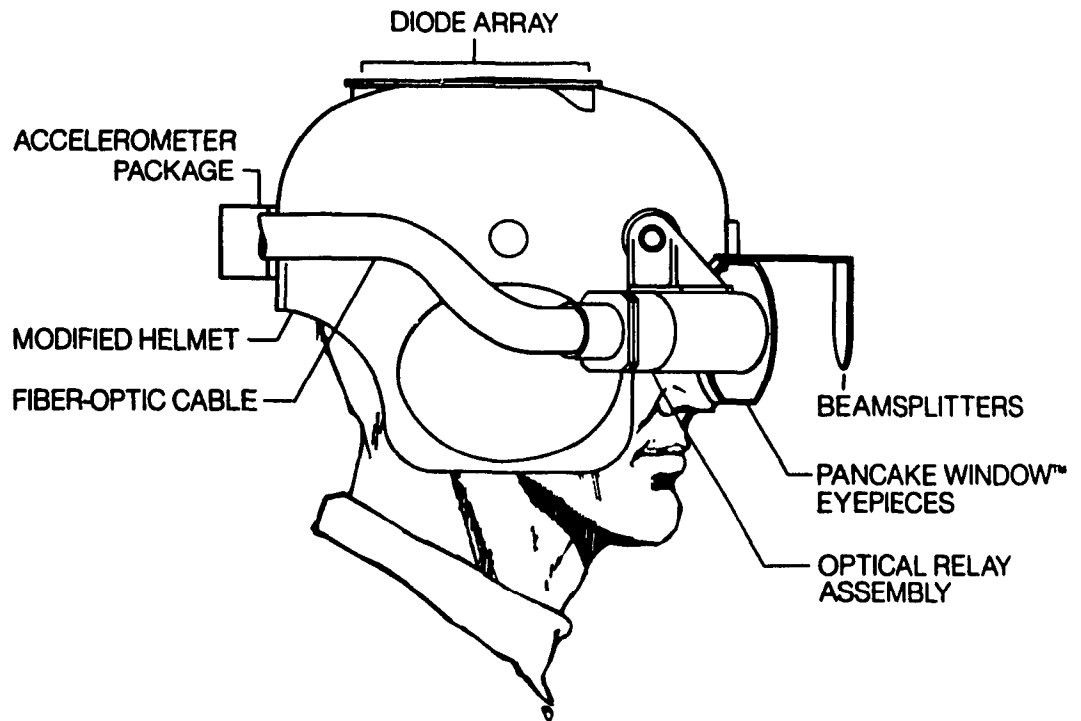


Figure 1.1: Schematic representation of the Fiber Optic Helmet Mounted Display (FOHMD) [4].

flight helmet [4] [5].

The main difficulties associated with the use of the FOHMD are the cockpit blanking and the maintenance of image stability. In order for the computer generated image of the "virtual" world to remain stationary as the pilot moves his head, the position of the pilot's helmet must be known relative to the simulator's fixed axes. This position is defined by three translation parameters (X, Y, Z) and three rotation parameters (Euler Angles). This information must also be known to align the computer generated image with the frame of the windscreen.

Therefore, an integral part of the FOHMD is the helmet position and orientation measurement system. As stated above, the performance criteria are particularly rigorous. The position and orientation of the pilot's helmet must be known in all six degrees-of-freedom, with a resolution comparable to the acuity of the human eye (2 to 3 arc minutes), and at a frame rate at least equal to that of the image generator (60 hz).

1.3 Review of "Line-of-Sight" Sensing Systems

A number of "line-of-sight" sensing systems have been developed for use on combat aircraft. They provide the pilots of such aircraft with a fast "heads up" means of

directing on-board sensors and weapons. The pilot need only move his head to superimpose the sighting reticle on the target and depress an action switch. The entire process requires only a few seconds and is a very positive, direct method of pointing the driven device at the selected target.

The accepted norm is to represent the accuracy of "line-of-sight" sensing systems by the Circular Error Probability or CEP. CEP represents the angle of the cone within which the measured "line-of-sight" will fall with a 50% confidence interval. Depending upon the installation, available systems have an accuracy of 0.5° CEP. This is acceptable in helmet aiming systems where the pilot's ability to track and mark a target is severely limited by the optical distortion caused by the canopy as well as the vibration experienced in high speed flight at low altitudes. These factors can induce errors of as much as 2° . An

Two widely used "line-of-sight" sensing systems are described in some detail below. Other available systems only provide angular information in two degrees-of-freedom (i.e. elevation and train) and have therefore been excluded from this discussion.

1.3.1 Honeywell/Polhemus System

This system utilizes a three-dimensional magnetic field produced by an orthogonal set of radiating coils. These coils are fixed to the airframe at a point on the longitudinal axis just above and behind the pilot's head. The radiating coils excite the windings of a second set of coils remotely located on the pilot's helmet. The output of the sensing coils can be used to calculate the position of the pilot's helmet relative to the fixed axes of the radiator [6] [7].

The Honeywell/Polhemus System does not function properly in environments containing metallic structures. The magnetic fields generated by the radiating coils produce circulating currents in nearby conductive material thereby generating secondary magnetic fields which distort the measurement. Metallic structures that are fixed in position and orientation with respect to the source produce field distortion that is constant at any given position. Compensation for the field distortion is therefore possible. Moving metallic structures such as those which mount directly on the helmet are significantly more difficult to deal with, particularly if they fall between the sensor and radiator. The use of certain metallic devices which must be helmet mounted (i.e. the display hardware) precludes the use of the Honeywell/Polhemus System in the FOHMD system.

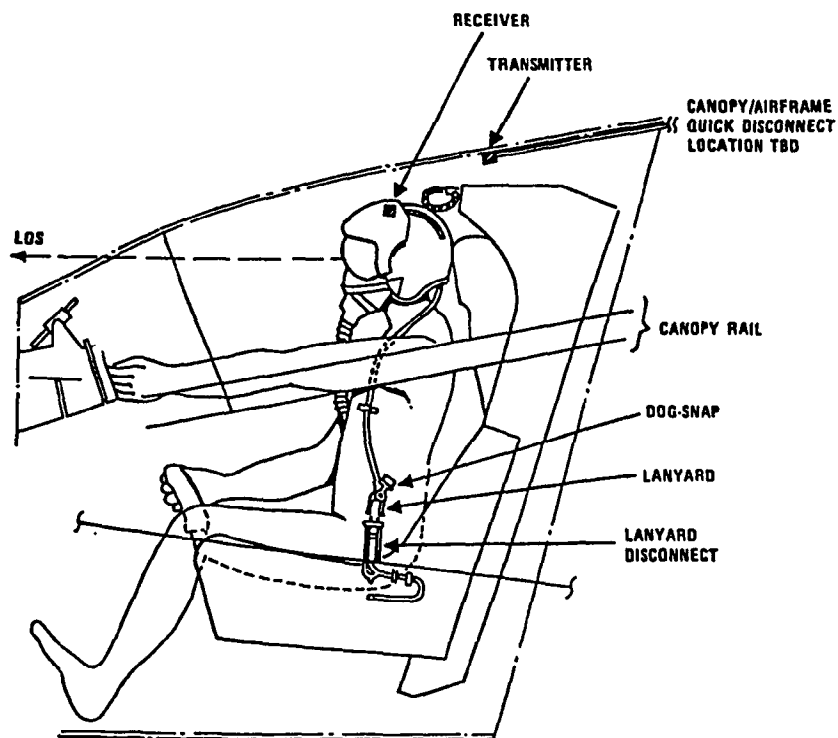


Figure 1.2: Installation Detail of Honeywell/Polhemus Helmet Position Sensing System [7].

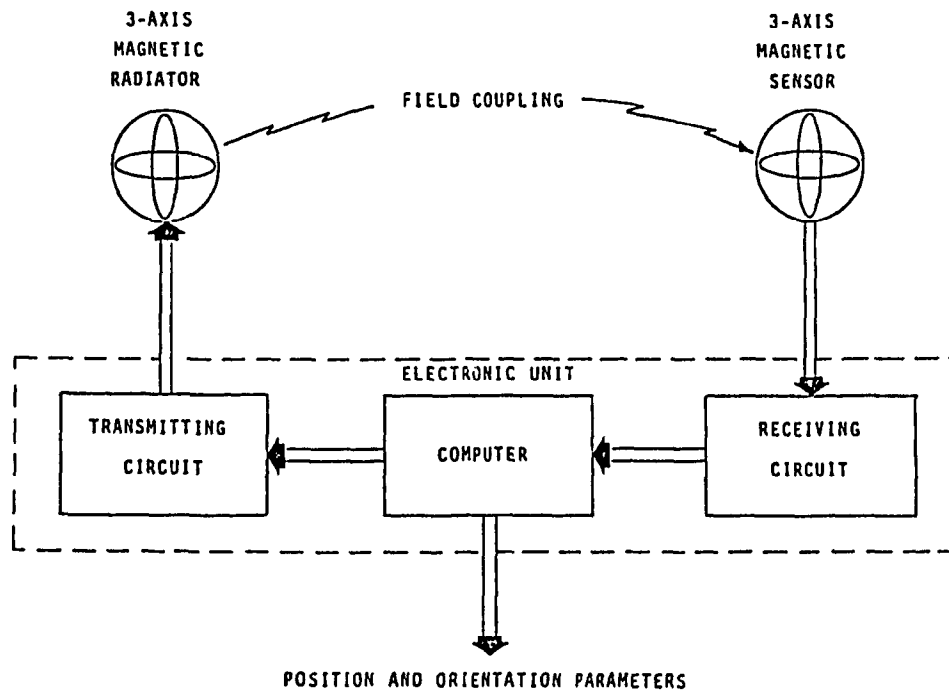


Figure 1.3: Block Diagram of Honeywell/Polhemus System [7].

1.3.2 Marconi System

The heart of this system is the cockpit-mounted V slit camera. This camera is directed at a triad of infrared Light Emitting Diodes (LEDs) which are fixed to the side of the pilot's helmet. When one of the three LEDs is flashed on, infrared light enters the camera through a narrow 0.008 inch V slit and creates an image across a high resolution linear charge coupled device (CCD). This device consists of 1728 discrete photosensitive elements. The analog signals from these elements are transferred out of the CCD serially at a rate of 2.5 MHz. The resulting output waveform consists of a series of pulses, amplitude modulated with the optical information. It takes approximately 0.7 milliseconds for one complete scan of all the elements in the array.

The position of an LED can be determined in both the horizontal and vertical planes from the two points where the V image intersects the CCD. Lateral translation of the LED causes the two points to move across the CCD without changing their separation. The separation changes when the LED is moved longitudinally. The intersection points correspond to peaks in the CCD output waveform.

In order to determine the helmet position and orientation, the V slit camera first samples and stores the background illumination with the helmet LEDs switched off. The LEDs are then flashed on in sequence and the CCD output

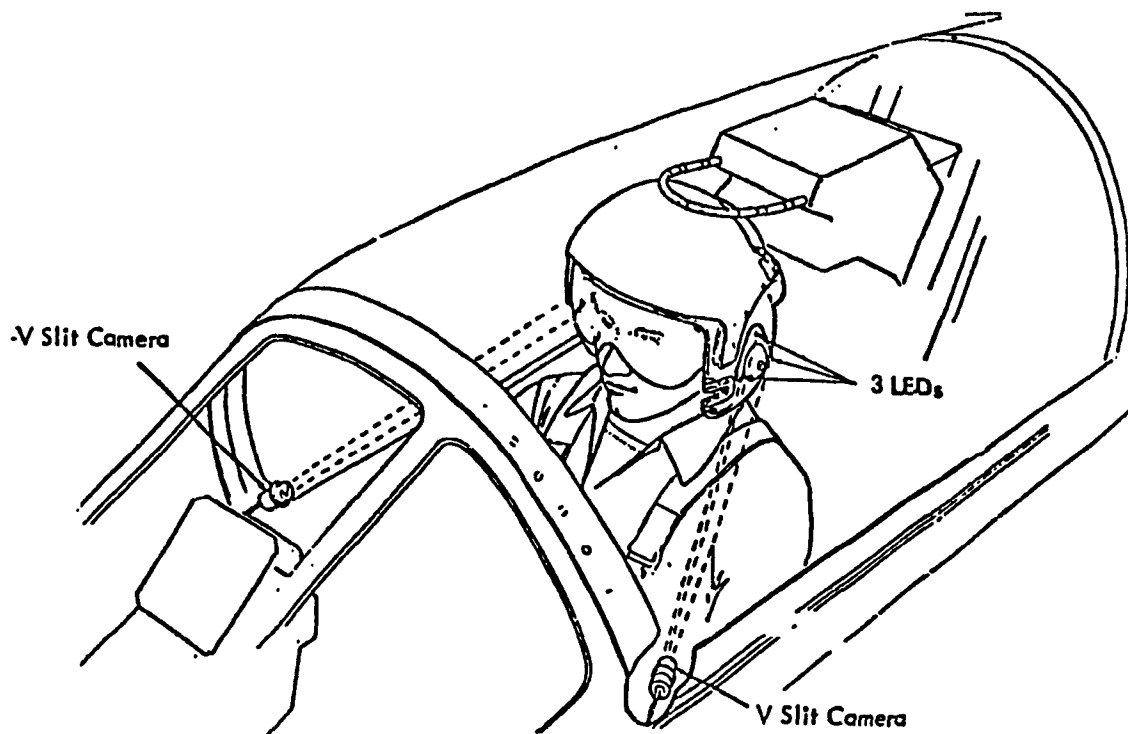


Figure 1.4: Installation Detail of Marconi Helmet Position Sensing System [8].

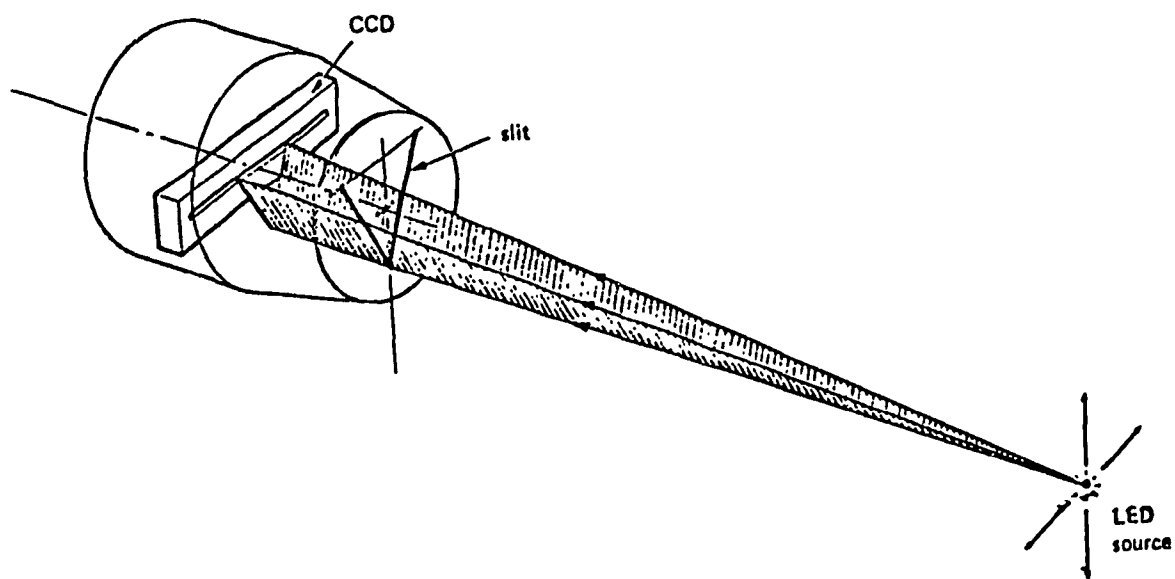


Figure 1.5: Schematic of V Slit Camera [8].

waveform is subtracted from the background illumination. This is done in order to improve the definition of the LED peaks. By using the corrected waveform to gate counters, the location of each peak is determined. The raw data, in the form of two binary numbers per LED, is then transferred via the interface circuit to the system computer which performs the line-of-sight computation. Although a single camera provides sufficient information to compute helmet orientation in roll, pitch and yaw, a second camera and another set of LEDs are necessary to cover all the possible head positions. The Marconi Helmet Position Sensing System is accurate to about 0.5° CEP in most installations [8] [9] [10].

1.3.3 Summary

Commercially available "line-of-sight" sensing systems are unable to meet the demanding requirements of the FOHMD program. In order for the FOHMD to function satisfactorily, a ten fold improvement in accuracy is required.

Other possible approaches include the use of accelerometers to detect motion. By integrating the accelerometer output signal, a position signal can theoretically be derived. Practically, such a signal is subject to drift.

Ultrasonic "time-of-flight" devices are ultimately

limited by the speed of sound which in turn is a function of temperature, humidity, altitude, frequency, barometric pressure, and air flow.

In summary, no currently available measurement system can meet the demanding performance requirements of the FOHMD program.

1.4 Thesis Outline

This thesis deals with techniques for determining, in real-time and with a high degree of accuracy, the absolute position and orientation of a rigid body in space.

Chapter 2 describes a highly effective, mechanical, six degree-of-freedom, position measurement system which provides an accurate, low cost alternative to sophisticated ultrasonic or optical noncontact measurement systems. The main disadvantage of this system is that the rigid body whose position and orientation is to be determined is effectively "tethered" by a mechanical linkage.

The difficulties inherent in acquiring accurate spatial information in real-time from conventional image sensors (Charge-Coupled Devices, Vidicons, etc.) are described in Chapter 3. Fundamental performance limitations such as spatial resolution, photon noise, target contrast, and volume of data to be processed are discussed. A novel sensor

capable of meeting the conflicting requirements of high accuracy and real-time response is introduced and analyzed.

Chapter 4 deals with the hardware aspects of the noncontact, six degree-of-freedom position measurement system developed for the FOHMD. Emphasis is placed on the target selection and implementation.

A mathematical model of the lens-sensor assembly is presented in Chapter 5. Algorithms for computing the position and orientation of a rigid body in space from one or more perspective views are formulated in chapter 6 and 7.

Chapter 8 is a critical evaluation of the influence of various parameters on system performance. Concluding remarks and future work are presented in Chapter 9.

CHAPTER 2

MECHANICAL POSITION MEASUREMENT SYSTEM

2.1 Introduction

Figure 2.1 is a schematic representation of the mechanical, six degree-of-freedom, position measurement system developed for the prototype area-of-interest display described in Chapter 1. In many applications, such a mechanical system can provide an accurate, low cost alternative to sophisticated ultrasonic or optical noncontact measurement systems.

Although inherently unacceptable for the FOHMD program, the Mechanical Position Measurement System served a twofold purpose. As a "research vehicle" it provided a means of establishing a firm set of performance criteria for the more complex Optical Position Measurement System. Secondly, it permitted a rigorous evaluation of the FOHMD early in the development stages.

The mechanical system is basically a six degree-of-freedom mechanism consisting of two links. Link C is connected to the fixed reference frame through joint 3 which has one degree-of-freedom. Link B is coupled to the rigid body whose position and orientation is to be determined via joint 1 and to link C via joint 2. Joints 1

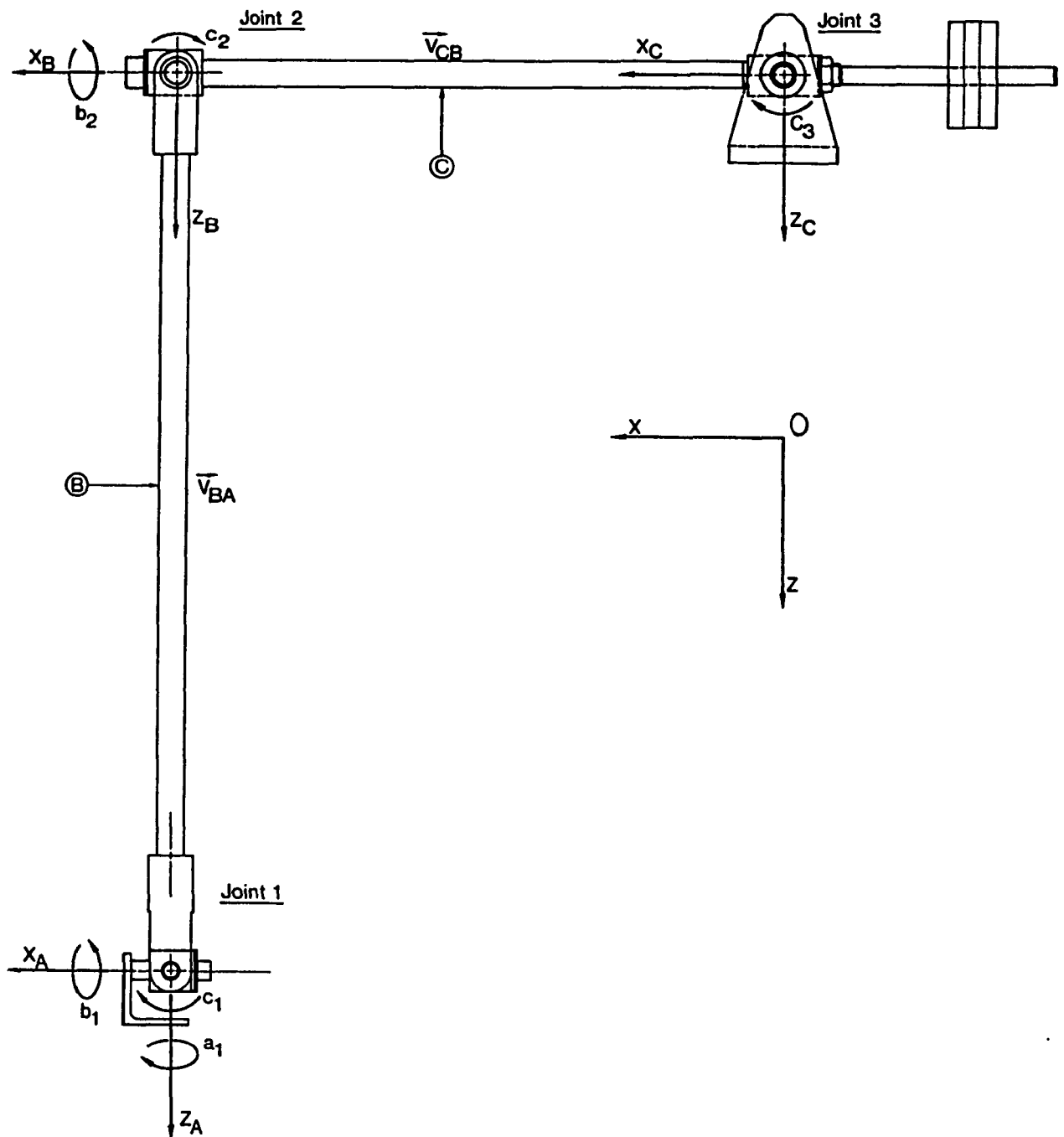


Figure 2.1: Schematic representation of Mechanical Position Measurement System showing fixed and movable coordinate systems.

and 2 have three and two degrees of freedom respectively. The analysis which follows relates the general displacement of the rigid body to the six measurable angles of the mechanism.

2.2 Translation Measurement

The translation of the rigid body is defined by the vector joining point A with the origin of the fixed coordinate system. This vector denoted by \vec{V}_{OA} , is the resultant of vectors \vec{V}_{OC} , \vec{V}_{CB} , and \vec{V}_{BA} .

\vec{V}_{OC} is a vector constant used to relocate the origin of the fixed coordinate system to the nominal rigid body position.

$$\vec{V}_{OC} = \begin{bmatrix} -17.25 \\ 0. \\ -25. \end{bmatrix}^T \begin{bmatrix} \vec{i} \\ \vec{j} \\ \vec{k} \end{bmatrix} \quad (2.1)$$

\vec{V}_{OC} can be adjusted to suit the installation.

\vec{V}_{CB} is the vector representing link C of the mechanism. Since joint 3 has only one degree of freedom, link C is constrained to move in the X-Z plane. A single angle, c_3 , defines the position of link C. \vec{V}_{CB} , which is of length 17.25 in (0.43815 m), is given by:

$$\vec{V}_{CB} = (17.25) \begin{bmatrix} \cos(c_3) \\ 0. \\ -\sin(c_3) \end{bmatrix}^T \begin{bmatrix} \vec{i} \\ \vec{j} \\ \vec{k} \end{bmatrix} \quad (2.2)$$

\vec{V}_{BA} is the vector representing link B of the mechanism. Joint 2 has two degrees of freedom, hence two angles, b_2 and c_2 , are required to define the position of link B with respect to link C. The orthogonal axes fixed to link C are denoted by X_c , Y_c , Z_c . As shown in figure 2.2, a right-handed rotation about X_c in the amount b_2 defines Y_c' and Z_c' . With respect to these axes, vector \vec{V}_{BA} can be expressed as:

$$\vec{V}_{BA} = (25.) \begin{bmatrix} \sin(c_2) \\ 0. \\ \cos(c_2) \end{bmatrix}^T \begin{bmatrix} \vec{i}_c' \\ \vec{j}_c' \\ \vec{k}_c' \end{bmatrix} \quad (2.3)$$

The unit vectors \vec{i}_c' , \vec{j}_c' , \vec{k}_c' can be written in terms of \vec{i}_c , \vec{j}_c , \vec{k}_c as follows:

$$\begin{aligned} \vec{i}_c' &= (1.)\vec{i}_c + (0.)\vec{j}_c + (0.)\vec{k}_c \\ \vec{j}_c' &= (0.)\vec{i}_c + \cos(b_2)\vec{j}_c + \sin(b_2)\vec{k}_c \\ \vec{k}_c' &= (0.)\vec{i}_c - \sin(b_2)\vec{j}_c + \cos(b_2)\vec{k}_c \end{aligned}$$

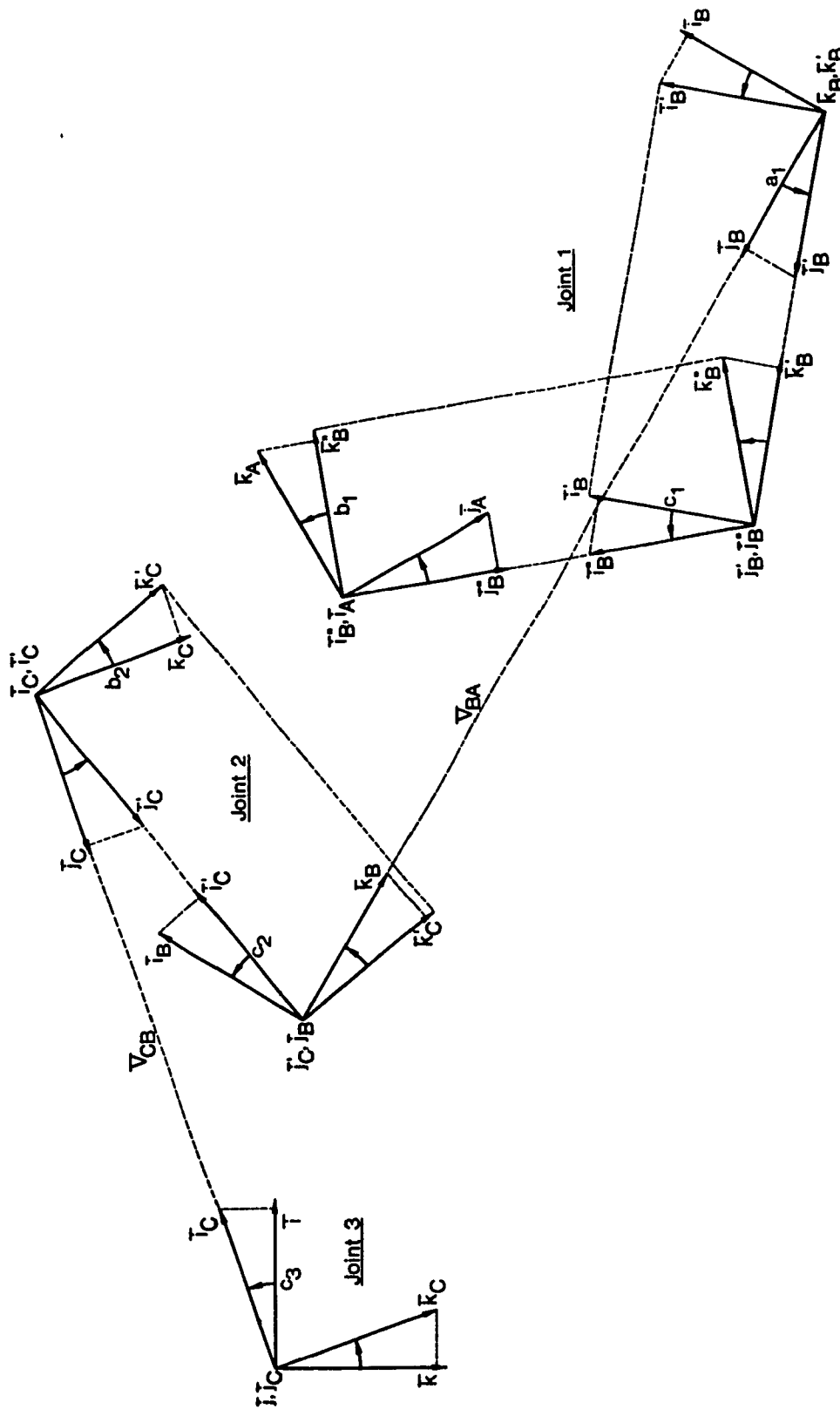


Figure 2.2: Schematic representation of coordinate transformations at Joints 1, 2, and 3.

$$\begin{bmatrix} \vec{i}_c' \\ \vec{j}_c' \\ \vec{k}_c' \end{bmatrix} = \begin{bmatrix} 1. & 0. & 0. \\ 0. & \cos(b_2) & \sin(b_2) \\ 0. & -\sin(b_2) & \cos(b_2) \end{bmatrix} \begin{bmatrix} \vec{i}_c \\ \vec{j}_c \\ \vec{k}_c \end{bmatrix} \quad (2.4)$$

The components of vector \vec{v}_{BA} with respect to the x_c , y_c , z_c coordinate system can be found by combining equations 2.3 and 2.4:

$$\vec{v}_{BA} = (25.) \begin{bmatrix} \sin(c_2) \\ 0. \\ \cos(c_2) \end{bmatrix}^T \begin{bmatrix} 1. & 0. & 0. \\ 0. & \cos(b_2) & \sin(b_2) \\ 0. & -\sin(b_2) & \cos(b_2) \end{bmatrix} \begin{bmatrix} \vec{i}_c \\ \vec{j}_c \\ \vec{k}_c \end{bmatrix}$$

$$\vec{v}_{BA} = (25.) \begin{bmatrix} \sin(c_2) \\ -\cos(c_2)\sin(b_2) \\ \cos(c_2)\cos(b_2) \end{bmatrix}^T \begin{bmatrix} \vec{i}_c \\ \vec{j}_c \\ \vec{k}_c \end{bmatrix} \quad (2.5)$$

An additional transformation matrix is needed to carry vector \vec{v}_{BA} into the fixed coordinate system. This matrix, denoted by $[C]$, relates the orthogonal unit vectors of link C to those of the fixed coordinate system, i.e.

$$\begin{aligned} \vec{i}_c &= \cos(c_3)\vec{i} + (0.)\vec{j} - \sin(c_3)\vec{k} \\ \vec{j}_c &= (0.)\vec{i} + (1.)\vec{j} + (0.)\vec{k} \\ \vec{k}_c &= \sin(c_3)\vec{i} + (0.)\vec{j} + \cos(c_3)\vec{k} \end{aligned}$$

$$\begin{bmatrix} \vec{i}_c \\ \vec{j}_c \\ \vec{k}_c \end{bmatrix} = \begin{bmatrix} \cos(c_3) & 0. & -\sin(c_3) \\ 0. & 1. & 0. \\ \sin(c_3) & 0. & \cos(c_3) \end{bmatrix} \begin{bmatrix} \vec{i} \\ \vec{j} \\ \vec{k} \end{bmatrix} \quad (2.6)$$

By combining equations 2.5 and 2.6, vector \vec{v}_{BA} can be written in terms of the fixed unit vectors $\vec{i}, \vec{j}, \vec{k}$.

$$\begin{aligned} \vec{v}_{BA} &= (25.) \begin{bmatrix} \sin(c_2) \\ -\cos(c_2)\sin(b_2) \\ \cos(c_2)\cos(b_2) \end{bmatrix}^T \begin{bmatrix} \cos(c_3) & 0. & -\sin(c_3) \\ 0. & 1. & 0. \\ \sin(c_3) & 0. & \cos(c_3) \end{bmatrix} \begin{bmatrix} \vec{i} \\ \vec{j} \\ \vec{k} \end{bmatrix} \\ \vec{v}_{BA} &= (25.) \begin{bmatrix} \sin(c_2)\cos(c_3) + \cos(c_2)\cos(b_2)\sin(c_3) \\ -\cos(c_2)\sin(b_2) \\ -\sin(c_2)\sin(c_3) + \cos(c_2)\cos(b_2)\sin(c_3) \end{bmatrix}^T \begin{bmatrix} \vec{i} \\ \vec{j} \\ \vec{k} \end{bmatrix} \quad (2.7) \end{aligned}$$

\vec{v}_{OA} , the vector defining the X, Y, Z position of the rigid body is defined by:

$$\vec{v}_{OA} = \vec{v}_{OC} + \vec{v}_{CB} + \vec{v}_{BA} \quad (2.8)$$

where \vec{v}_{OC} , \vec{v}_{CB} , and \vec{v}_{BA} are defined by equations 2.1, 2.2, and 2.7 respectively [11] [12].

2.3 Rotation Measurement

In the previous section, the origin of the rigid body

coordinate system was located with respect to the fixed coordinate system. Since a rigid body with one point fixed has three degrees-of-freedom, three additional independent rotations are needed to describe the general displacement of the body. These rotations are defined by the Euler angles. The Euler angles can be obtained from the matrix of direction cosines, $[T]$, which relates the rigid body coordinate system to the fixed coordinate system.

$$[T] = [A][B][C] \quad (2.9)$$

$[A]$, $[B]$, and $[C]$ are the matrices of direction cosines relating adjacent coordinate systems. For example, matrix $[C]$ relates the orthogonal unit vectors of link C (\vec{i}_C , \vec{j}_C , \vec{k}_C) to those of the fixed cockpit coordinate system.

$$\begin{aligned} \begin{bmatrix} \vec{i}_A \\ \vec{j}_A \\ \vec{k}_A \end{bmatrix} &= [A] \begin{bmatrix} \vec{i}_B \\ \vec{j}_B \\ \vec{k}_B \end{bmatrix} \\ \begin{bmatrix} \vec{i}_B \\ \vec{j}_B \\ \vec{k}_B \end{bmatrix} &= [B] \begin{bmatrix} \vec{i}_C \\ \vec{j}_C \\ \vec{k}_C \end{bmatrix} \\ \begin{bmatrix} \vec{i}_C \\ \vec{j}_C \\ \vec{k}_C \end{bmatrix} &= [C] \begin{bmatrix} \vec{i} \\ \vec{j} \\ \vec{k} \end{bmatrix} \end{aligned} \quad (2.10)$$

Matrix [C] appears in the derivation of vector \vec{V}_{BA} and is given by equation 2.6.

$$[C] = \begin{bmatrix} \cos(c_3) & 0. & -\sin(c_3) \\ 0. & 1. & 0. \\ \sin(c_3) & 0. & \cos(c_3) \end{bmatrix} \quad (2.11)$$

Figure 2.2 graphically illustrates the coordinate transformations at joint 2. Since joint 2 has two degrees of freedom, two angles are required to define the orthogonal unit vectors of link B in terms of those on link C. A right-handed rotation about X_c in the amount b_2 defines Y_c' and Z_c' . With respect to these axes, the orthogonal unit vectors of link B can be expressed as:

$$\begin{aligned} \vec{i}_B &= \cos(c_2)\vec{i}_c' + (0.)\vec{j}_c' - \sin(c_2)\vec{k}_c' \\ \vec{j}_B &= (0.)\vec{i}_c' + (1.)\vec{j}_c' + (0.)\vec{k}_c' \\ \vec{k}_B &= \sin(c_2)\vec{i}_c' + (0.)\vec{j}_c' + \cos(c_2)\vec{k}_c' \end{aligned}$$

$$\begin{bmatrix} \vec{i}_B \\ \vec{j}_B \\ \vec{k}_B \end{bmatrix} = \begin{bmatrix} \cos(c_2) & 0. & -\sin(c_2) \\ 0. & 1. & 0. \\ \sin(c_2) & 0. & \cos(c_2) \end{bmatrix} \begin{bmatrix} \vec{i}_c' \\ \vec{j}_c' \\ \vec{k}_c' \end{bmatrix} \quad (2.12)$$

Equation 2.4 relates the unit vectors \vec{i}_c' , \vec{j}_c' , \vec{k}_c' to those of link C.

$$\begin{bmatrix} \vec{i}_c' \\ \vec{j}_c' \\ \vec{k}_c' \end{bmatrix} = \begin{bmatrix} 1. & 0. & 0. \\ 0. & \cos(b_2) & \sin(b_2) \\ 0. & -\sin(b_2) & \cos(b_2) \end{bmatrix} \begin{bmatrix} \vec{i}_c \\ \vec{j}_c \\ \vec{k}_c \end{bmatrix} \quad (2.13)$$

Matrix [B], the matrix relating the orthogonal unit vectors on link B to those of link C, can be found by substituting equation 2.13 into equation 2.12.

$$\begin{aligned} [B] &= \begin{bmatrix} \cos(c_2) & 0. & -\sin(c_2) \\ 0. & 1. & 0. \\ \sin(c_2) & 0. & \cos(c_2) \end{bmatrix} \begin{bmatrix} 1. & 0. & 0. \\ 0. & \cos(b_2) & \sin(b_2) \\ 0. & -\sin(b_2) & \cos(b_2) \end{bmatrix} \\ [B] &= \begin{bmatrix} \cos(c_2) & \sin(c_2)\sin(b_2) & -\sin(c_2)\cos(b_2) \\ 0. & \cos(b_2) & \sin(b_2) \\ \sin(c_2) & -\cos(c_2)\sin(b_2) & \cos(c_2)\cos(b_2) \end{bmatrix} \quad (2.14) \end{aligned}$$

Matrix [A] relates the rigid body coordinate system to the orthogonal unit vectors of link B. Since joint 1 has three degrees of freedom, matrix [A] is a function of three angles. As shown in figure 2.2, a right-handed rotation about Z_B in the amount a_1 defines X_B' and Y_B' . A second rotation about Y_B' in the amount c_1 defines Z_B'' and X_B'' . A final rotation about X_B'' in the amount b_1 yields the rigid body coordinate axes X_A, Y_A, Z_A .

$$\begin{aligned}
\vec{i}_A &= (1.)\vec{i}_B'' + (0.)\vec{j}_B'' + (0.)\vec{k}_B'' \\
\vec{j}_A &= (0.)\vec{i}_B'' + \cos(b_1)\vec{j}_B'' + \sin(b_1)\vec{k}_B'' \\
\vec{k}_A &= (0.)\vec{i}_B'' - \sin(b_1)\vec{j}_B'' + \cos(b_1)\vec{k}_B''
\end{aligned}$$

$$\begin{bmatrix} \vec{i}_A \\ \vec{j}_A \\ \vec{k}_A \end{bmatrix} = \begin{bmatrix} 1. & 0. & 0. \\ 0. & \cos(b_1) & \sin(b_1) \\ 0. & -\sin(b_1) & \cos(b_1) \end{bmatrix} \begin{bmatrix} \vec{i}_B'' \\ \vec{j}_B'' \\ \vec{k}_B'' \end{bmatrix} \quad (2.15)$$

$$\begin{aligned}
\vec{i}_B'' &= \cos(c_1)\vec{i}_B' + (0.)\vec{j}_B' - \sin(c_1)\vec{k}_B' \\
\vec{j}_B'' &= (0.)\vec{i}_B' + (1.)\vec{j}_B' + (0.)\vec{k}_B' \\
\vec{k}_B'' &= \sin(c_1)\vec{i}_B' + (0.)\vec{j}_B' + \cos(c_1)\vec{k}_B'
\end{aligned}$$

$$\begin{bmatrix} \vec{i}_B'' \\ \vec{j}_B'' \\ \vec{k}_B'' \end{bmatrix} = \begin{bmatrix} \cos(c_1) & 0. & -\sin(c_1) \\ 0. & 1. & 0. \\ \sin(c_1) & 0. & \cos(c_1) \end{bmatrix} \begin{bmatrix} \vec{i}_B' \\ \vec{j}_B' \\ \vec{k}_B' \end{bmatrix} \quad (2.16)$$

$$\begin{aligned}
\vec{i}_B' &= \cos(a_1)\vec{i}_B + \sin(a_1)\vec{j}_B + (0.)\vec{k}_B \\
\vec{j}_B' &= -\sin(a_1)\vec{i}_B + \cos(a_1)\vec{j}_B + (0.)\vec{k}_B \\
\vec{k}_B' &= (0.)\vec{i}_B + (0.)\vec{j}_B + (1.)\vec{k}_B
\end{aligned}$$

$$\begin{bmatrix} \vec{i}_B' \\ \vec{j}_B' \\ \vec{k}_B' \end{bmatrix} = \begin{bmatrix} \cos(a_1) & \sin(a_1) & 0. \\ -\sin(a_1) & \cos(a_1) & 0. \\ 0. & 0. & 1. \end{bmatrix} \begin{bmatrix} \vec{i}_B \\ \vec{j}_B \\ \vec{k}_B \end{bmatrix} \quad (2.17)$$

Matrix [A], the matrix relating the orthogonal unit vectors of the rigid body to those of link B can be found by

combining equations 2.15, 2.16, and 2.17.

$$[A] = \begin{bmatrix} 1. & 0. & 0. \\ 0. & \cos(b_1) & \sin(b_1) \\ 0. & -\sin(b_1) & \cos(b_1) \end{bmatrix} \begin{bmatrix} \cos(c_1) & 0. & -\sin(c_1) \\ 0. & 1. & 0. \\ \sin(c_1) & 0. & \cos(c_1) \end{bmatrix} \begin{bmatrix} \cos(a_1) & \sin(a_1) & 0. \\ -\sin(a_1) & \cos(a_1) & 0. \\ 0. & 0. & 1. \end{bmatrix}$$

$$A_{11} = \cos(c_1) \cos(a_1)$$

$$A_{12} = \cos(c_1) \sin(a_1)$$

$$A_{13} = -\sin(c_1)$$

$$A_{21} = \sin(b_1) \sin(c_1) \cos(a_1) - \cos(b_1) \sin(a_1)$$

$$A_{22} = \sin(b_1) \sin(c_1) \sin(a_1) + \cos(b_1) \cos(a_1) \quad (2.18)$$

$$A_{23} = \sin(b_1) \cos(c_1)$$

$$A_{31} = \cos(b_1) \sin(c_1) \cos(a_1) + \sin(b_1) \sin(a_1)$$

$$A_{32} = \cos(b_1) \sin(c_1) \sin(a_1) - \sin(b_1) \cos(a_1)$$

$$A_{33} = \cos(b_1) \cos(c_1)$$

Since Euler angles are defined by the same sequence of rotations as followed for joint 1 [13], equation 2.18 is also the matrix of direction cosines expressed in terms of Euler angles. The absolute rotation of the rigid body (i.e. with respect to the fixed coordinate system) can be

determined by equating matrix [T] with equation 2.18 and solving for the Euler angles, α , β , γ .

$$\begin{aligned}\alpha &= \text{ATAN2}(T_{12}, T_{11}) \\ \beta &= \text{ATAN2}(T_{23}, T_{33}) \\ \gamma &= \text{ASIN}(-T_{13})\end{aligned}\tag{2.19}$$

Angles α , β , γ are more commonly referred to as yaw, roll, and pitch respectively [13].

2.4 Data Acquisition and Processing

Data processing tasks for the mechanical, six degree-of-freedom, position measurement system are performed by an Intel 8086 based single board computer (iSBC 86/14). The Intel 8087 Numeric Processor, which is capable of performing hardware floating point arithmetic, is used to improve the execution speed of the algorithm.

In the prototype area-of-interest display described in chapter 1, aircraft dynamics are modeled on a GOULD SEL 32/55 computer. Position and orientation data are transferred from the INTEL 86/14 to the SEL 32/55 host computer through a MULTIBUS-SELBUS Controller (MBSEL). The MBSEL board is an intelligent DMA controller which communicates with the SELBUS via a High Speed Data Interface Board (HSD). Data transfers are transparent to both the SEL

and 8086 processors.

Joints 2 and 3 of the mechanical, six degree-of-freedom, position measurement system are instrumented with Rotary Variable Differential Transformers (RVDTs) which have a full-scale range of ± 30 degrees. Potentiometers with a full-scale range of ± 160 degrees are used to instrument the three angles of joint 1. The analog signals from these transducers are digitized by a National Semiconductor BLC 711 Analog Input Board. This board is based on a 12-bit, 50 kHz A/D converter.

The MBSEL board, the analog I/O board, and the single board computer are housed in an INTEL iSBC 660 System Chassis. This chassis is 7 inches high and mounts in a standard 19-inch rack. It can accommodate up to eight cards.

The subroutine which calculates the position and orientation from the six measurable angles of the mechanism is written in FORTRAN-86 (Appendix 1). All the other routines including the MBSEL and analog I/O board drivers, the interrupt handler, and the 86/14 initialization routines, are written in ASSEMBLER-86. The final, error-free software resides on four 2732 EPROMS and is executed automatically on RESET.

2.5 Performance

Performance parameters for the Mechanical Position Measurement System are summarized in Table 2.1. The operating envelope covers the entire range of helmet movement possible within the cockpit of a tactical aircraft simulator. The relatively large standard error in rotation is attributable to the poor linearity of the potentiometers used to instrument joint 1. The rotational resolution of the system is limited by the A/D converter and is in the order of 0.08° .

The computational effort required to determine position and orientation can be significantly reduced by instrumenting the mechanism with resolvers which provide the sine and cosine of the measured angle. This would eliminate the need to evaluate 12 transcendental functions at every iteration. The primary concern is the availability of compact, light weight resolvers.

The main disadvantage of the Mechanical Position Measurement System is that the rigid body whose position and orientation is to be determined is "tethered" by a mechanical linkage. Although the mechanism is counterbalanced to compensate for the static load, the added inertia of the linkage can be significant in some applications.

Table 2.1: Performance summary of Mechanical Position Measurement System.

PARAMETER	TRANSLATION	ROTATION
Operating Envelope	±300 mm X ±300 mm Y ±150 mm Z	±160° ROLL ±160° PITCH ±160° YAW
Standard Error	0.081 mm	0.15°
Iteration Rate	60 Hz	60 Hz

CHAPTER 3

IMAGE SENSORS

3.1 Introduction

A number of noncontact electro-optical measurement systems have been developed for robotic applications. In most of these systems, the visual sensory information is acquired by means of a scanning-type device such as the vidicon camera or a solid-state image sensor based on a CCD, CID, or photodiode array [14]. The principle of operation and the inherent limitations of these imaging devices are outlined below.

3.2 The Vidicon Camera

The absorption of light by a photoconductor results in the generation of charge carriers which contribute to the electrical conductivity of the material. In the vidicon camera, the visual image creates a charge pattern across a photoconductive surface. This surface is scanned by an electron beam which deposits a sufficient number of electrons to neutralize the accumulated charges. The analog video signal is based on the current flowing across the photoconductive surface as a function of time.

The electron beam scans the image at a constant velocity along a set of equally spaced parallel lines. The two-dimensional cartesian coordinates of each picture element (pixel) can be determined from the position of the electron beam. The number of scan lines defines the vertical position of the pixel while the elapsed time from the horizontal synchronization pulse specifies the position in the horizontal direction. The instantaneous amplitude of the video signal is proportional to the total luminous flux received at the pixel being scanned over a period of one frame [15] [16].

In machine vision applications, the video signal is sampled at a finite number of points along each scan line. The digital image is stored as a two-dimensional array of intensity values. If each intensity value occupies 8 bits of storage, then a single frame of standard video requires 247,800 bytes of memory (525 lines by 472 pixels). Ideally, this information should be processed within one-thirtieth of a second (i.e. the frame rate of the camera). Clearly this is beyond the capabilities of most minicomputers. In general, commercially available robot vision systems, operating on suitably constrained images with appropriate lighting, can be expected to process approximately 5 images per second [17] [18].

The volume of data required to describe the analog video signal can be reduced by representing the intensity of each pixel by a single bit. The resulting "binary" images are useful for identifying and determining the orientation of objects which have a high contrast ratio with respect to the background. In order to operate reliably, binary vision systems require high contrast lighting and a carefully structured viewing area [19].

In reference 20, Pinkney describes the development of a noncontact measurement system for real-time three-dimensional control. A vidicon camera is used to track a pattern of circular black targets on a highly reflective white background. Because of the high contrast ratio, the targets can be discriminated from the background by simply monitoring the level of the video signal. The centroid of the two-dimensional image of each target is computed by a dedicated processor. The position and orientation of the pattern with respect to the camera are determined from the centroid data [21]. A specially designed target and illumination system ensure adequate target to background contrast.

If the vision system is expected to operate under a wide range of lighting conditions, then gray scale imaging is required. This technique, which involves resolving the image into various shades of gray, increases the versatility

of the vision system but usually at the expense of speed. At present, full gray scale image processing is not possible at a rate suitable for machine control tasks [17] [22].

Although imaging devices such as the vidicon camera can be used with passive targets (e.g. black circles on a white background), the degree of illumination necessary to achieve an adequate signal to noise ratio can be difficult to realize. The signal to noise ratio is limited at low light levels by the photon noise [23]. This phenomenon is attributable to the quantum nature of light and is not a property of the imaging device. The output signal of any image sensor is a function of the average number of photons accumulated by the sensor over the integration time, Δt . The photon noise is equal to the standard deviation from this average value. Since the emission of photons from any source is a stochastic process which follows a Poisson distribution, the standard deviation of the random variable (i.e. the number of photons in a time interval Δt) is equal to the square root of the mean [24]. Therefore, the theoretical signal to noise ratio (S/N) of an imaging device is given by:

$$S/N = \frac{\bar{n}}{\sqrt{\bar{n}}} = \sqrt{\bar{n}} \quad (3.1)$$

where \bar{n} is the mean number of photons accumulated.

The signal to noise ratio can be improved by increasing the integration time, however, this is impractical in a real-time measurement system. Not only would the speed of the system be reduced but moving targets would appear blurred. The only viable method of improving the signal to noise ratio is to increase the target illumination. In general, obtaining the correct lighting conditions represents one of the most difficult problems in the implementation of a machine vision system [19].

If the signal to noise ratio is sufficiently high then the performance of the vision system is limited by the spatial resolution of the sensor, that is, the sensor's ability to discriminate between closely spaced points on the imaging surface. The spatial resolution of the vidicon camera is limited in the vertical direction by the number of scan lines, and in the horizontal direction by the rate at which the video signal is digitized. High resolution (1024 by 1024), computer compatible vidicon cameras are commercially available, however, the volume of data that must be processed during each video frame is prohibitive. At present most robot vision systems are based on cameras with a spatial resolution of 256 lines by 256 pixels.

3.3 Solid-State Image Sensors

In the vidicon camera the location of each picture element is defined by the position of the electron beam. In order to avoid distortions in the digital image, the electron beam must scan at a constant velocity. The horizontal scan lines must be parallel and equally spaced. In solid-state image sensors the location of each picture element is fixed in a silicon matrix so that precise geometric accuracy is guaranteed.

The latest generation of solid-state image sensors is based on the Charge-Coupled Device (CCD). The CCD consists of an array of discrete photosensitive elements. A lens is used to focus the image onto this array. By virtue of the photoelectric effect, the incident light causes the generation of free electrons in each element of the array. These electrons accumulate in a quantity proportional to the radiant energy absorbed in the vicinity of each element. After an appropriate exposure time, the individual "charge-packets" are transferred out of the CCD serially by the external manipulation of voltages. The resulting output waveform consists of a sequence of electrical pulses, the amplitude of each being directly proportional to the charge collected by a single photosensitive element [25]. In order to provide a television compatible video signal, most CCD

based cameras operate at a 30 Hz frame rate delivering two vertically interlaced fields per frame [26].

Due to their solid-state nature, CCD based image sensors are well suited to robot vision applications. In addition to precise geometric accuracy, they offer good reliability, low power consumption, and small size. In terms of resolution they have yet to match the performance of the vidicon camera, however, the spatial resolution of the sensor is not the limiting factor in most robot vision systems. In a highly dynamic control application the visual feedback must be derived in real-time and with a minimal delay. As a result, high resolution sensors are seldom used because of the volume of data that must be processed during each iteration. Commercially available CCD based image sensors, which have a maximum spatial resolution of 488 by 380 photosensitive elements, are adequate for most applications.

3.4 Summary

The performance criteria presented in chapter 1 are particularly rigorous, both in terms of accuracy and speed. Real-time measurement systems based on conventional image sensors (CCDs, vidicons, etc) are either not accurate enough because of the limited resolution of the sensor, or not fast enough because of the volume of data that must be processed.

These systems can be used with passive targets, however, at low light levels the fundamental limitation to performance is the photon noise. In the primary application addressed in this thesis, position sensing for a helmet mounted display, only relatively low levels of illumination can be tolerated.

3.5 Position Sensor Head

The Position Sensor Head is a compact device capable of accurately detecting the position of a light source in two dimensions. It was originally developed to provide measurement data for a gait pattern analysis system. This system is used to quantitatively evaluate the progress of the handicapped during rehabilitation. The Position Sensor Head has other industrial and scientific applications including vibrational and surface flatness measurement, solar tracking, and laser beam alignment. Unlike conventional image sensors, this device can meet the conflicting requirements of high accuracy and fast response at low levels of illumination.

3.5.1 Principle of Operation

The Position Sensor Head is not a true imaging device in that it does not create an electronic replica of a visual image. The photosensitive element used in this device is a silicon Position-Sensitive Detector (PSD). The PSD (Figure 3.1). is a planar type PIN photodiode with very uniform resistive layers formed over both the top and bottom surfaces. When a light spot is projected onto the sensitive surface of the PSD, electron-hole pairs are generated in the depletion layer directly under the light spot. The electric field in the I-layer causes the electrons and holes to separate, electrons moving to the N-layer, holes to the P-layer. The electrons are then collected by two opposing electrodes located on the resistive surface of the N-layer. The current flowing to each electrode is a function of both the intensity and the X position of the light spot. The holes are collected in a similar manner by two electrodes located on the surface of the P layer. In this case the current flowing to each electrode is a function of the intensity and Y position of the light spot.

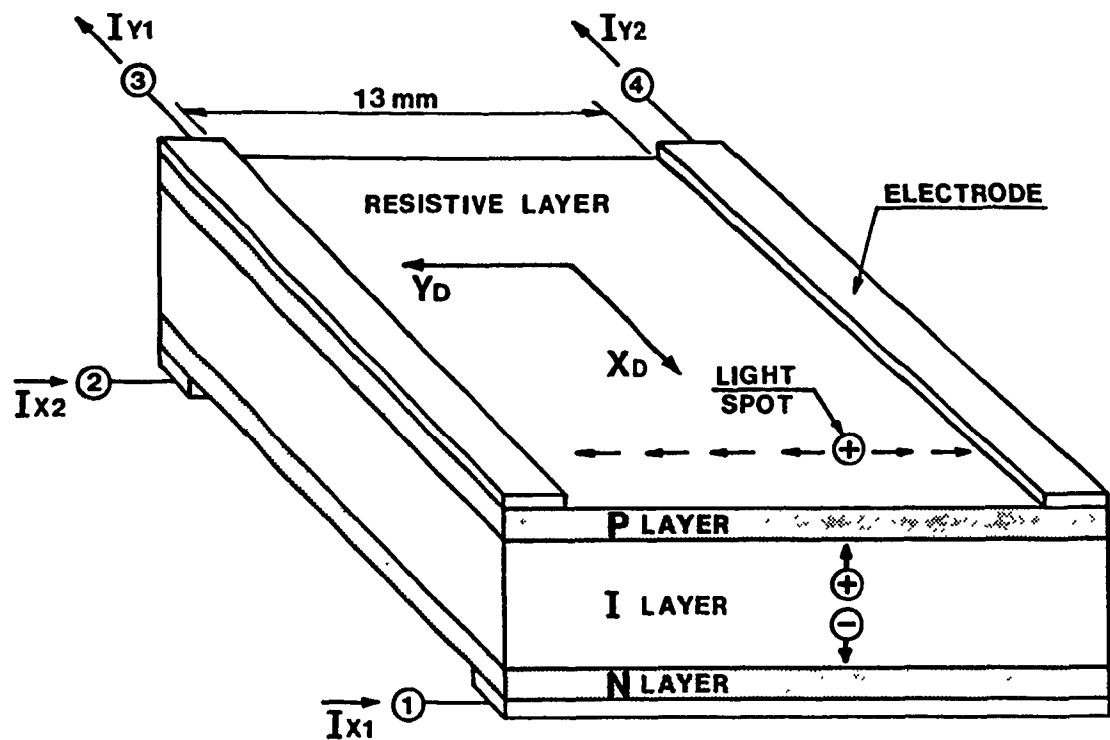


Figure 3.1: Schematic Representation of Position-Sensitive Detector (PSD).

3.5.2 Analog Position Processing Circuit

Ideally, the PSD should only respond to changes in the position of the light spot, not the intensity. In order to reduce the sensitivity of the PSD to variations in intensity, the output signals from the four electrodes are normalized by the Analog Position Processing Circuit shown in Figure 3.2. This circuit, which is located within the Position Sensor Head, also amplifies the low-level output signals of the PSD to a level consistent with data acquisition and recording devices. Since the amplified signals are less susceptible to electromagnetic interference, they can be transmitted over a longer distance.

In the first stage of the Position Processing Circuit, the current signals from the four electrodes are conditioned by a low-pass, first-order filter.

$$\frac{V}{I} = \frac{K_I}{1 + \tau_1 s} \quad (3.2)$$

where $K_I = -1.0 \times 10^5 \text{ V/A}$

$\tau_1 = 2.2 \text{ } \mu\text{sec.}$

The resulting voltage signals, V_{x1} , V_{x2} , V_{y1} , and V_{y2} , are used to derive the output signals, V_x , V_y , and Σ , provided by the Position Sensor Head. The intensity signal, Σ , is

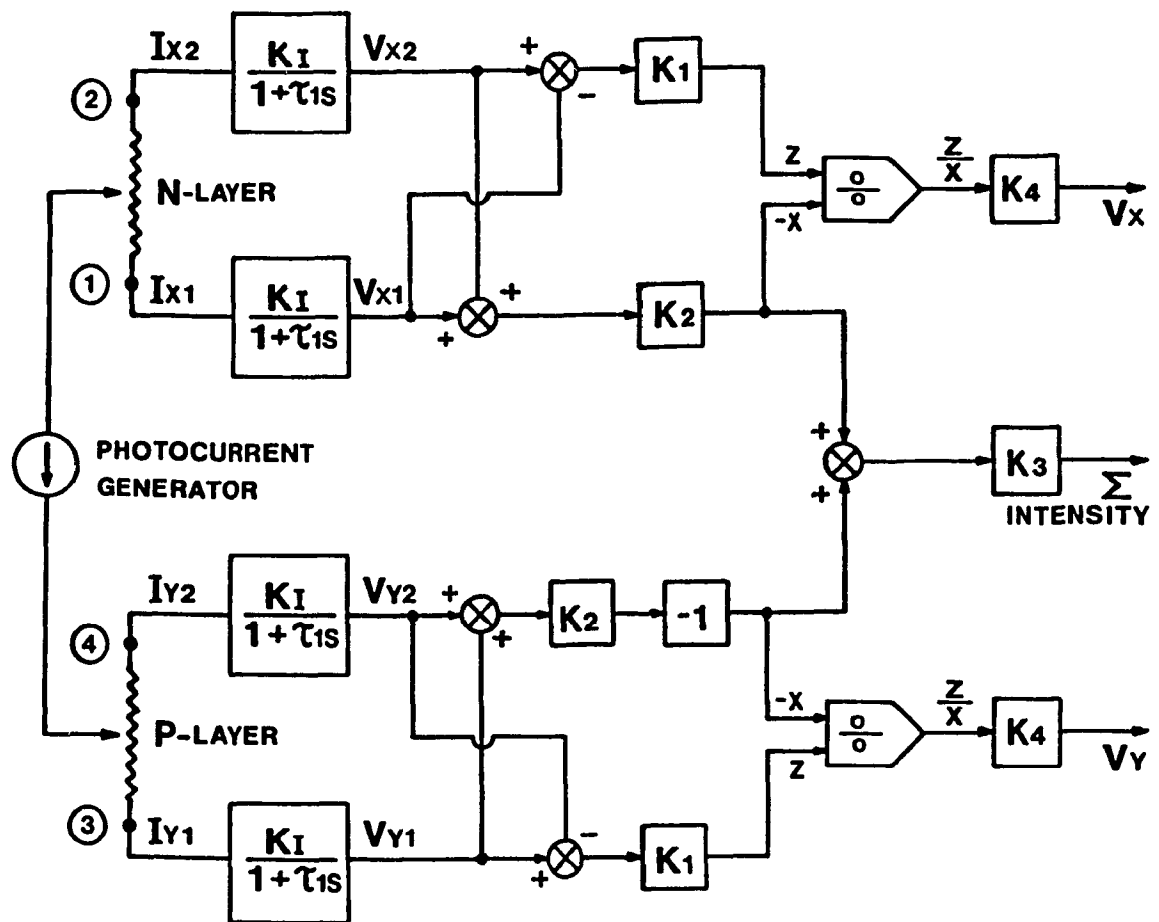


Figure 3.2: Block Diagram of the Analog Position Processing Circuit.

linearly related to the total current generated by the PSD.

$$\Sigma = K_3 K_2 \left[(V_{x1} + V_{x2}) - (V_{y1} + V_{y2}) \right] \quad (3.3)$$

where $K_2 = -20.0$

$K_3 = -0.47$

The intensity signal provides a measure of the total radiant flux incident on the sensitive surface of the PSD. This information can be used to predict the theoretical signal to noise ratio based on the photon noise.

As mentioned previously, both the top and bottom surfaces of the PSD are covered by a thin resistive layer. If this layer is of uniform thickness and constant resistivity, then the fraction of the total current flowing to a given electrode is inversely proportional to the distance between the electrode and the light spot. In this respect the PSD is analogous to a linear potentiometer with an ideal current source connected to the wiper. The X position signal, V_x , is based on the normalized current flowing from the light spot to each of the two opposing electrodes located on the surface of the N layer.

$$V_x = K_4 \left[\frac{K_1 (V_{x1} - V_{x2})}{K_2 (V_{x1} + V_{x2})} \right] \quad (3.4)$$

where $K_1 = -10.0$

$K_4 = 10.0$

The Y position signal, V_y , is derived in a similar manner.

$$V_y = K_4 \left[\frac{K_1 (V_{y1} - V_{y2})}{K_2 (V_{y1} + V_{y2})} \right] \quad (3.5)$$

In theory, the two position signals, V_x and V_y , are insensitive to variations in the intensity of the light spot. The sensitivity to variations in position is approximately 1 volt/mm.

3.5.3 Linearity

The linearity of the Position Sensor Head is not of prime importance in this study. Nonlinearities can be compensated for by means of a two-dimensional calibration table. Nevertheless, a straight-line relationship is preferable since considerably less computational effort is required if the position of the light spot is linearly related to the output signals, V_x and V_y .

Most commercially available PSD-type photodiodes

exhibit poor linearity particularly towards the extremities of the sensitive surface. In contrast to this the Position Sensor Head used in this study (Hamamatsu C1454-05) employs a highly linear PSD which provides accurate results based on a simple straight-line input-output relationship.

A calibration was performed in order to establish the linearity and sensitivity of the Position Sensor Head. A light spot was projected onto the sensitive surface of the PSD by means of a fiber optic emitter (Motorola MFOE102F). This particular source emits light through a narrow opening 0.2 mm in diameter. By holding the emitter within 0.5 mm of the sensitive surface, an extremely small light spot could be generated. For calibration purposes the Position Sensor Head was held in a micrometer controlled translation stage with a working accuracy of 1 μm (Newport Research Corporation Model 405).

Ideally, all interfering and modifying inputs must be held constant during calibration. In the case of the Position Sensor Head the most significant interfering input is the background illumination. This input was easily controlled by covering the calibration setup and reducing the ambient light level.

In theory, the output signals, V_x and V_y , are not affected by the intensity of the light spot. However, due to the inaccuracies inherent in performing an analog division,

the sensitivity of the Position Sensor Head to the desired input (i.e. the position of the light spot) is in some degree dependent on intensity. Intensity can therefore be regarded as a modifying input which must be held constant. A simple feedback control system (Figure 3.3) was implemented in order to maintain a constant intensity during calibration.

With the intensity constant and no background illumination, the output voltage signals, V_x and V_y , were recorded as the Position Sensor Head was displaced in precise 1 mm increments in both the X and Y directions. The resulting map of the sensitive surface is given in Appendix 2.

A reference straight line was fitted to the calibration data by the method of least squares. The linearity and sensitivity of the Position Sensor Head were then computed for both the X and Y output signals (Table 3.1). The quoted linearity is based on the maximum deviation of any point from the reference line expressed as a percent of full scale. The sensitivity is simply equal to the slope of the reference line.

In view of the highly linear characteristic exhibited by the Position Sensor Head, a two-dimensional calibration table was not implemented. A simple straight-line input-output relationship was found to be sufficiently accurate.

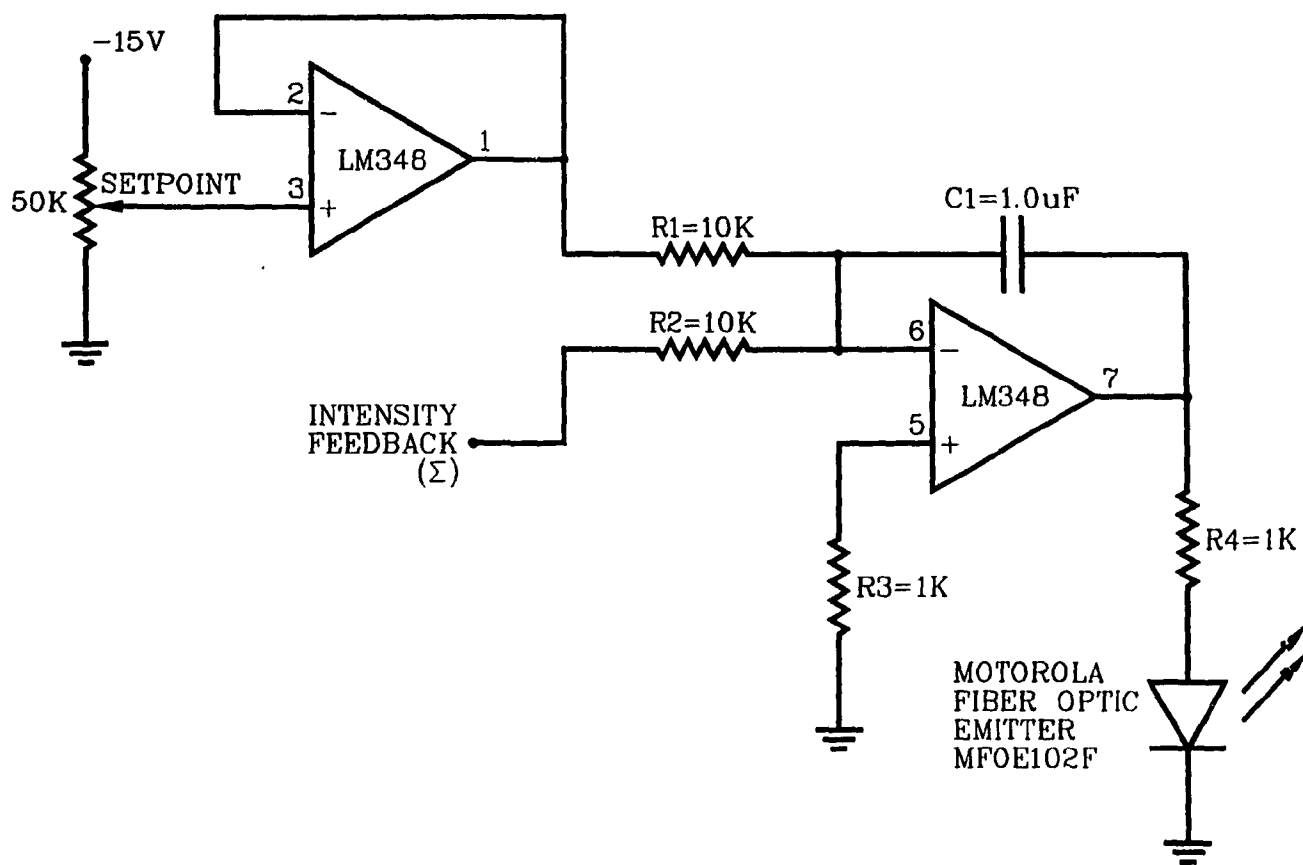


Figure 3.3: Schematic diagram of Intensity Control Circuit used in calibration.

Table 3.1: Calibration of Position Sensor Head: Summary of Results.*

Parameter	V _x output	V _y output	Units
Sensitivity	1.01569	1.01679	V/mm
Intercept	0.00662	0.00776	V
Linearity	0.56	0.28	%
Standard Error	0.020	0.011	V

*Conditions:

- 1.) Sensor Model Number: Hamamatsu C1454-05
(serial #81054767)
- 2.) Intensity of Light Spot: $\Sigma = 5.000$ V.
- 3.) No Background Illumination.

3.5.4 Resolution

The resolution of solid-state and scanning-type image sensors is ultimately limited by either the size of the photosensitive elements or the number of scan lines. This is not the case with the Position Sensor Head. Due to the continuous analog nature of the PSD, there is no definable geometric limitation on resolution. The resolution of the PSD is primarily noise limited. Noise is present due to the discrete nature of the incident light (photon noise) as well as the discrete nature of the photocurrent (shot current). Since the quantum efficiency of the PSD is less than 100%, the shot noise imposes a greater limitation on resolution. The intensity signal, Σ , is linearly related to the total current generated by the PSD and can be used to estimate the shot and photon noise.

3.5.5 Shot Noise

Under steady-state conditions, the total current generated by the PSD can be written in terms of the intensity signal, Σ , as follows:

$$\begin{aligned} (I_{x1} + I_{x2}) - (I_{y1} + I_{y2}) &= \frac{\Sigma}{K_3 K_2 K_1} \\ &= (-1.064 \times 10^{-6} \text{ A/V}) \Sigma \end{aligned} \tag{3.6}$$

Since electrons and holes are generated in equal numbers, the current flowing through the P layer is equal in magnitude and opposite in direction to the current flowing through the N layer.

$$(I_{y1} + I_{y2}) = -(I_{x1} + I_{x2}) = (0.532 \times 10^{-6} \text{ A/V}) \Sigma \quad (3.7)$$

In this study, the intensity signal, Σ , is actively maintained at 3.5 volts by a closed-loop control system (refer to chapter 4). The magnitude of the photocurrent, I_p , at this particular light level can be computed from 3.7 above.

$$I_p \Big|_{\Sigma=3.5} = 1.862 \times 10^{-6} \text{ A}$$

A current of 1 ampere represents a charge transfer, of 6.242×10^{18} electrons per second. Therefore,

$$I_p \Big|_{\Sigma=3.5} = 1.162 \times 10^{13} \text{ electrons/second}$$

The integration time, Δt , is approximately equal to the time constant of the PSD (10.47×10^{-6} seconds). The mean number of electrons accumulated during this time interval is denoted by \bar{n}_e and can be computed as follows:

$$\bar{n}_e = I_p \Delta t = 1.217 \times 10^8 \text{ electrons} \quad (3.8)$$

Since the number of electrons generated in a given time

interval follows a Poisson distribution, the theoretical signal to noise ratio based on the shot noise, $(S/N)_s$, is given by:

$$(S/N)_s = \sqrt{\bar{n}_e} = 11030 = 81 \text{ db} \quad (3.9)$$

3.5.6 Quantum Efficiency

Photon noise imposes an absolute limit on the resolution that can be attained at a particular light level and for a given integration time regardless of the image sensor. Most sensors fall short of ideal, photon noise limited performance because of the influence of other noise sources and because they have a quantum efficiency of less than 100 per cent. Quantum efficiency is defined as the fractional number of electron-hole pairs generated per incident photon.

In general, the quantum efficiency of an image sensor is dependent on the wavelength of the incident light. Therefore, for the purposes of this analysis, it is assumed that the light spot on the sensitive surface of the PSD is generated by a constant, monochromatic source. The light emitted from this source has a wavelength, λ , equal to $0.93 \text{ } \mu\text{m}$. At this particular wavelength, the ratio of the total current generated by the PSD to the incident radiant

flux is equal to 0.52 A/W. This ratio is referred to as the responsivity of the PSD at a wavelength of 0.93 μm .

The incident radiant flux can be converted from units of power to an equivalent, average number of photons per second. Each photon represents a quantity of energy, E_p , equal to Planck's constant, h , times the frequency of the incident light, f [27].

$$E_p = h f \quad (3.10)$$

where $h = 6.63 \times 10^{-34} \text{ J / Hz}$.

The product of frequency and wavelength equals the velocity of light, c . Therefore,

$$E_p = \frac{h c}{\lambda} \quad (3.11)$$

where $c = 3.00 \times 10^8 \text{ m/s}$.

At a wavelength of 0.93 μm , E_p is equal to $2.14 \times 10^{-19} \text{ J}$.

As stated previously, the responsivity of the PSD at 0.93 μm is equal to 0.52 A/W. One amp represents a charge transfer of 6.24×10^{18} electrons per second while one watt of radiant power is equal to $1/E_p$ or 4.68×10^{18} photons per second. Therefore, the quantum efficiency, η , of the PSD at 0.93 μm is equal to:

$$\begin{aligned} \eta &= \frac{(0.52) (6.24 \times 10^{18} \text{ electrons/second})}{(4.68 \times 10^{18} \text{ photons/second})} \\ &= 0.69 \text{ electrons/photon} \end{aligned}$$

By comparison, CCD image sensors exhibit a peak quantum efficiency of approximately 15%, while the efficiency of the human retina at low light levels is estimated at between 10 and 20% [28] [29].

The mean number of photons absorbed during the integration time, Δt , is denoted by \bar{n}_p and is given by:

$$\bar{n}_p = \bar{n}_e / \eta = 1.764 \times 10^8 \text{ photons} \quad (3.12)$$

Since the emission of photons from any source follows a Poisson distribution, the signal to noise ratio based on the photon noise is equal to the square root of \bar{n}_p .

$$(S/N)_p = \sqrt{\bar{n}_p} = 13281 = 82 \text{ db} \quad (3.13)$$

By virtue of its high quantum efficiency, the PSD approaches the fundamental limit of resolution imposed by the photon noise. A significant improvement in performance can only be achieved by increasing the number of incident photons, that is, increasing the intensity of the light spot or the integration time.

3.6 Sensitivity to Modifying and Interfering Inputs

3.6.1 Background Illumination

Since the PSD is essentially a silicon photodiode, it is sensitive to light in the range of 0.3 to 1.1 μm . Background light falling within this range represents an input to which the PSD is unintentionally sensitive (i.e. an interfering input). The undesirable effects of this input can best be reduced by simply darkening the surroundings. This is consistent with the operation of the Helmet Mounted Display where for reasons of image contrast and clarity only relatively low levels of background light can be tolerated. In other applications, however, the system may be required to operate under normal room light. Under these circumstances, an optical bandpass filter can be used to minimize the effects of background light. This type of filter transmits the incident radiation in one spectral region and blocks all other radiation. By placing the filter directly in front of the Position Sensor Head, accurate measurements can be taken under normal room light.

The bandpass filter must be spectrally matched to the target light source. In this study, the target light source has a peak emission wavelength of 0.93 μm which corresponds to the maximum responsivity of the PSD (0.52 A/W). This

wavelength is beyond the visible range (0.4 to 0.7 μm) yet distinguishable from the infrared radiation which is emitted from surfaces at ordinary temperatures. Most of the thermally generated photons incident on or emitted from a surface at room temperature are of a relatively long wavelength (greater than 10 μm). The ambient density of photons in the neighborhood of 0.93 μm is equivalent to a visible surface brightness of 10^{-11} foot-lambert which is far below the absolute threshold of human vision [29].

The amount of infrared radiation present under normal room illumination is dependent on the type of light source in use. In a typical manufacturing or laboratory environment the ambient illumination is provided by fluorescent tubes which emit little or no infrared radiation. In such an environment the introduction of an optical bandpass filter with a centre wavelength of 0.93 μm virtually eliminates the influence of background light.

Incandescent light sources present a greater problem since a large part of the energy emitted is in the form of infrared radiation. If the system is required to operate under incandescent lighting, the intensity of the target light source must be increased in order to ensure an adequate signal to noise ratio. Optical filtering can still be used to eliminate as much background light as possible.

3.6.2 Intensity of the Light Spot

The two position signals provided by the Position Sensor Head, V_x and V_y , are theoretically insensitive to variations in the intensity of the light spot. However, due to inherent inaccuracies in the Analog Position Processing Circuit, the sensitivity of the Position Sensor Head to the desired input (i.e. the position of the light spot) is in some degree dependent on intensity. This dependency was investigated experimentally. The Position Sensor Head was recalibrated at an intensity level of 2.5 volts which corresponds to a 50% reduction in the intensity of the light spot. This resulted in a 1% decrease in sensitivity for both the X and Y output voltage signals.

The calibration results indicate that significant measurement errors can arise if large variations in the intensity of the light spot are permitted. Such variations can be caused by either a pure rotation of the light source or a change in the distance between the light source and the Position Sensor Head. Since it affects the sensitivity of the Position Sensor Head to the desired input, the intensity of the light spot can be considered a modifying input. The only viable method of correction for this particular input is to introduce a closed-loop control system which actively maintains a constant intensity irrespective of the position

or orientation of the light source. The intensity signal, Σ , is available as a feedback for this control system.

3.6.3 Size of the Light Spot

In this study, a conventional camera lens is used to focus light from a remote source onto the sensitive surface of the PSD. For a given focal setting of the lens, the two-dimensional image of the light source will only be in focus if the light source lies in the plane conjugate to that of the sensitive surface. At a greater or lesser distance, the light source will appear somewhat blurred. The maximum deviation of the light source from the conjugate plane without causing serious deterioration of the image quality is referred to as the depth of field of the lens [30]. The depth of field can be increased by reducing the aperture of the lens however this is extremely costly in terms of light intensity.

In general, two conflicting requirements must be met in order to derive accurate spatial information from an image formed by a lens with a fixed focus. Firstly, a large aperture is required to intercept as much light as possible and ensure an adequate signal to noise ratio. Secondly, the depth of field must be large so that the image remains in focus as the object moves away from the conjugate plane.

Clearly both requirements cannot be met satisfactorily.

With a conventional image sensor, image processing techniques can be employed to partially compensate for a poorly focused image. If an object point lies outside the depth of field, it will not be imaged as a point, but as a small circle. The centroid of this circle closely approximates the image point of an ideal lens with the correct focal setting. Unfortunately, determining the centroid of the two-dimensional image of each object point involves significant computational effort. In contrast, the output signals provided by the Position Sensor Head, V_x and V_y , are proportional to the coordinates of the centroid of a two-dimensional light spot travelling over the surface of the detector. As a result, the Position Sensor Head is intrinsically insensitive to the size of the light spot or the sharpness of focus.

3.7 Response

Since the PSD is essentially a silicon PIN photodiode, its response time is extremely fast; in the order of 20 μsec . If a reverse bias is applied to the PSD, that is, if the cathode is made positive with respect to the anode, the dynamic performance of the device improves. With a reverse bias of 5 volts, the rise time of the PSD drops to 11 μsec .

Unfortunately, the application of reverse bias results in the flow of "dark current" which is defined as the current which flows through a photosensitive device when no radiant flux is applied. Dark current is indistinguishable from light current and can be considered an interfering input which varies exponentially with temperature. For this reason, the zero bias or photovoltaic mode of operation is usually preferred [28].

The PSD employed in the Position Sensor Head operates in the photovoltaic mode and therefore has a dynamic range of approximately 50 kHz. Unlike conventional image sensors, this permits accurate monitoring of even a rapidly moving light spot.

3.8 Summary

The Position Sensor Head provides continuous, two-dimensional position data on a light spot traveling over the detector surface. Unlike conventional image sensors which are limited by either the spatial resolution of the sensor or the volume of data that must be processed, the Position Sensor Head can meet the conflicting requirements of high accuracy and fast response at low levels of illumination.

CHAPTER 4

OPTICAL POSITION MEASUREMENT SYSTEM - SYSTEM DESCRIPTION

4.1 Introduction

It has been shown that the Position Sensor Head is capable of accurately monitoring the two-dimensional position of a light spot moving over the sensitive surface of the PSD. When combined with a conventional camera lens, the Position Sensor Head can also provide information on the position of a light source moving in three-dimensional space. The lens focuses light from the source onto the sensitive surface of the PSD. The resulting image is a two-dimensional perspective projection of the target light source. If a number of light sources are fixed to a rigid body, then the position and orientation of that body can be determined from the image coordinates of the body-fixed sources.

4.2 Target Light Source

Mathematically the light sources represent fixed points on a rigid body. This representation is accurate providing the light sources are point radiators. A point radiator is one in which the maximum dimension of the light emitting

surface is small in comparison with the distance to the detector.

Since the rigid body is free to assume a wide range of orientations within the viewing space, the light source should be visible from any viewing angle. Ideally, the radiant intensity distribution of the source should be spherical, that is, the intensity should be independent of the angle between the line of sight and the optical axis of the light source.

The undesirable effects of background illumination can be reduced through the use of an optical band pass filter. In order to maximize the effectiveness of this filter, the target light source should be virtually monochromatic; it should only emit light over a narrow spectral region. The peak emission wavelength should correspond to the point in the spectrum at which the responsivity of the PSD is maximum ($0.93 \mu\text{m}$).

Due to the continuous analog nature of the PSD, noise is the primary factor limiting resolution. As with all image sensors, the signal to noise ratio can be improved by increasing either the integration time or the intensity of the target light source. A long integration time is impractical in a real-time application, therefore the target light source must have a high radiant power output. This is particularly true if the radiant intensity distribution of

the source is spherical and the distance to the detector large. Under these circumstances, only a small portion of the total radiant power emitted ever reaches the detector.

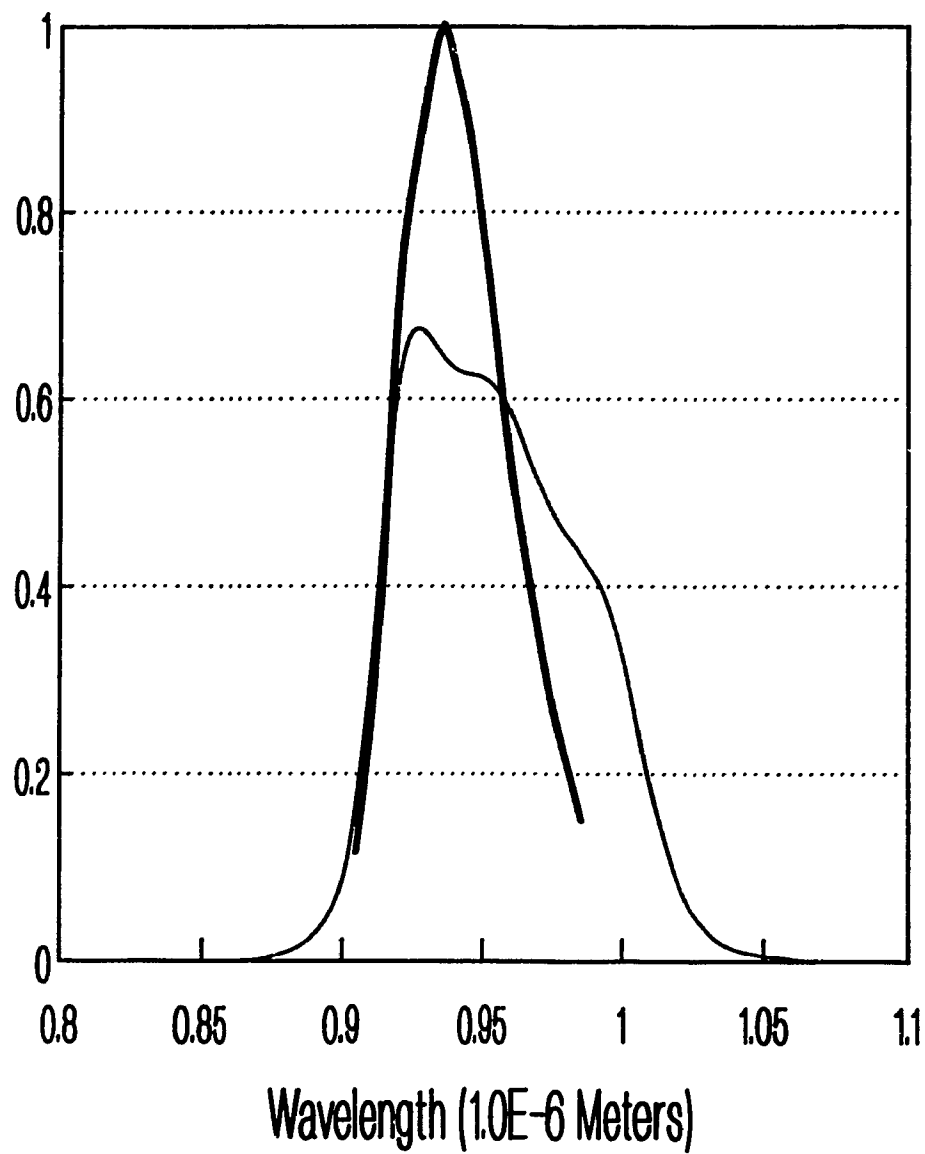
Ideally, the radiant flux incident on the sensitive surface of the PSD should remain constant as the distance between the light source and the detector varies. This can be accomplished by implementing a closed-loop control system which regulates the radiant power emitted from the light source based on a feedback signal from the detector. Since the light sources are illuminated sequentially, a certain delay must be incurred after each source is selected to allow for the settling time of the light source, detector and associated control circuitry. In order to minimize this delay, the light sources should exhibit fast rise and fall times and good controllability.

To summarize, the ideal target light source is a monochromatic point radiator with a peak emission wavelength of $0.93\ \mu\text{m}$, a spherical radiant intensity distribution, and a high radiant power output. In addition, it must exhibit fast switching times and good controllability. No currently available source can completely satisfy all of these requirements, however, a solid-state Light Emitting Diode (LED) is the most suitable in terms of dynamic response and controllability. The specific LED selected is a Gallium Arsenide infrared emitting diode (Texas Instruments TIES16A)

which has average rise and fall times of 250 and 300 nanoseconds respectively. The optical power produced is, to a first approximation, a linear function of the forward bias current [28].

The light emitting surface of this particular LED is a hemispherically shaped dome 0.072 inches (1.83 mm) in diameter. Since the distance to the detector is nominally 1 meter, this source can be considered a point radiator. In addition, the hemispherical shape of the light emitting surface results in a wide emission pattern. The emission pattern is generally characterized by the half intensity beam angle which refers to the angle within which the radiant intensity of the source is not less than half of the peak intensity. The half intensity beam angle of the TIES16A diode is 150° .

Figure 4.1 shows the relative radiant power output, Φ_{EREL} , as a function of wavelength, λ , for the TIES16A diode. The wavelength at peak emission is $0.933 \mu\text{m}$ which corresponds to the maximum responsivity of the PSD. The half power points occur at 0.956 and $0.911 \mu\text{m}$ which indicates that the radiant power output is concentrated in the vicinity of the optimum wavelength.



— Filter Transmittance — LED Relative Power

Figure 4.1: Relative Radiant power output, Φ_{EREL} , versus wavelength, λ , for the TIES16A Light Emitting Diode.

The maximum-rated continuous forward current, I_{FMAX} , for the TIES16A is 2 amps which provides a total radiant power output of 0.1 watts (minimum). The TIES16A can be operated in the pulse mode at considerably higher current levels providing that the duty cycle is limited. The peak current, I_p , can be approximated with reasonable accuracy by:

$$I_p = \frac{I_{FMAX}}{D} \quad (4.1)$$

where D is the mark-space ratio or duty cycle. With the diode at room temperature, the radiant power produced is a linear function of the forward bias current. An increase in temperature will cause the diode to become less efficient and thereby decrease the radiant power output for any given forward bias current. In order to maintain a high radiant efficiency at high current levels, the heat generated as a result of power loss must be conducted away from the diode junction. In the case of the TIES16A, the light emitting element is mounted on a copper stud header which provides a low-thermal-resistance path for efficient heat sinking.

In this study, the diode is operating in the pulse mode at a peak current of 15 amps and a duty cycle of 2.5% (400 μ sec. "on" time every 16.6 msec.). Since the average current is only 0.375 amps there is no appreciable increase in

temperature and the peak radiant power output is approximately 0.75 watts.

4.3 Intensity Control System

The purpose of the Intensity Control Circuit is to maintain the radiant flux incident on the sensitive surface of the PSD constant irrespective of the position or orientation of the LED. This is achieved by means of a closed loop control system which regulates the radiant power emitted from each LED based on a feedback signal from the detector. Since the LEDs are illuminated sequentially, the dynamic performance of this control system is critical.

In order to investigate a variety of control strategies, a mathematical model of the Intensity Control Circuit was formulated. This model includes the LED, the Intensity Control Circuit, the Position Sensitive Detector, and the optics and geometry of the system.

4.3.1 Light-Emitting Diode

When a Light-Emitting Diode (LED) is forward biased, electrons from the N region are injected into the P region and radiant energy is released through recombination. Infrared Emitting Gallium Arsenide Diodes have, to a first

approximation, a linear dependence of the radiant power output, Φ_E , on the diode forward current, I_F .

$$\Phi_E = Q \cdot I_F \quad (4.2)$$

Q is the quantum efficiency of the diode. For the TIES16A Q is equal to 0.05 W/A. The forward current, I_F , is a function of the forward voltage, V_F , the junction voltage, V_J , and the diode series resistance, r_s .

$$I_F = \frac{V_F - V_J}{r_s} \quad (4.3)$$

V_J and r_s are equal to 1.223 volts and 0.16 Ω respectively for the TIES16A.

4.3.2 N-Channel, Enhancement Mode MOSFET

The forward current through the LED is controlled by a power MOSFET (Metal-Oxide-Semiconductor Field-Effect Transistor). The specific device selected (International Rectifier IRF150) is an N-channel, enhancement mode MOSFET which exhibits low on-state resistance, high transconductance, and very fast switching times. These properties make it ideal for high energy pulse circuits.

In an enhancement mode MOSFET, the gate is insulated from the substrate by an oxide layer. As a result, the

output current is controlled by an input voltage rather than an input current. Within the active or normal operating region (i.e. above saturation), the drain current, I_D , is nearly independent of the drain-to-source voltage, V_{DS} , and the transfer characteristic is approximately parabolic.

$$\begin{aligned} I_D &= K \cdot (V_{GS} - V_T)^2 \\ V_T &\leq V_{GS} \leq (V_{DS} + V_T) \end{aligned} \quad (4.4)$$

V_{GS} is the input (Gate-to-Source) voltage, K is a constant which is dependent on the material properties and dimensions, and V_T is the turn-on or threshold voltage. For the IRF150, K and V_T are equal to 1.777 A/V^2 and 3.0 volts respectively.

The voltage-controlled-resistance region occurs when the MOSFET is operated below saturation (i.e. $V_{GS} \geq V_{DS} + V_T$). Within this region the drain current, I_D , is a function of both the gate-to-source voltage, V_{GS} , and the drain-to-source voltage, V_{DS} [31].

$$I_D = 2 \cdot K \cdot \left[(V_{GS} - V_T) \cdot V_{DS} - \frac{V_{DS}^2}{2} \right] \quad (4.5)$$

As shown in Figure 4.2, the MOSFET is connected in the common-source configuration with the LED between the d.c. supply voltage, V_{DD} , and the drain terminal of the MOSFET.

In this configuration the drain current, I_D , is equal to the forward current through the LED, I_F . The forward voltage drop across the LED, V_F , is given by:

$$V_F = V_{DD} - V_{DS} \quad (4.6)$$

Substituting this expression into the current-voltage characteristic of the LED (equation 4.3) yields an expression relating the drain current, I_D , to the drain-to-source voltage, V_{DS} .

$$I_D = I_F = \frac{V_{DD} - V_{DS} - V_J}{r_s} \quad (4.7)$$

If the MOSFET is operating above saturation, then the transfer characteristic of the MOSFET is given by equation 4.4 and an expression relating V_{DS} to the input voltage, V_{GS} , can be derived.

$$V_{DS} = V_{DD} - V_J - r_s \cdot K \cdot \left(V_{GS} - V_T \right)^2 \quad (4.8)$$

$$V_T \leq V_{GS} \leq (V_{DS} + V_T)$$

If the MOSFET is operating in the voltage-controlled-resistance region (i.e below saturation), then the governing characteristic is equation 4.5. In this case, V_{DS} is related to V_{GS} as follows:

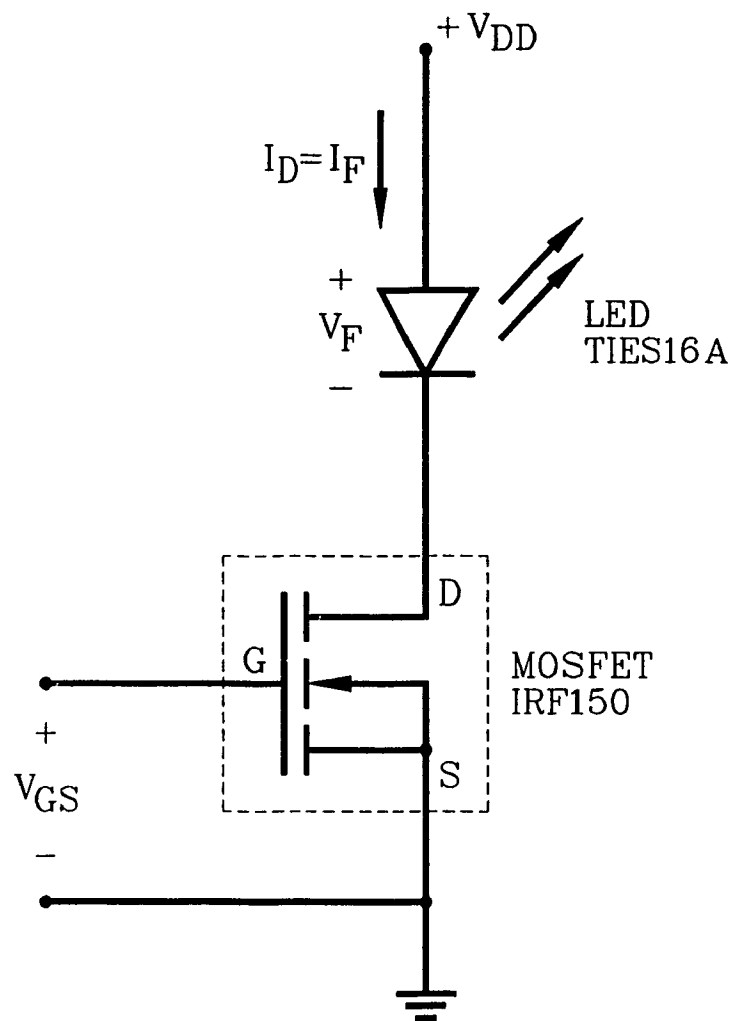


Figure 4.2: MOSFET and LED connected in the common-source configuration

$$V_{DS} = \frac{-b - \sqrt{b^2 - 4c}}{2} \quad (4.9)$$

$$b = - \left[2 \cdot (V_{GS} - V_T) + \frac{1}{k \cdot r_s} \right]$$

$$c = \frac{V_{CC} - V_J}{k \cdot r_s}$$

$$V_{GS} \geq V_{DS} + V_T$$

The value of V_{GS} at which saturation occurs can be found by substituting $V_{GS} = V_{DS} + V_T$ into either equation 4.8 or 4.9.

$$V_{GSAT} = 5.288 \text{ volts}$$

V_{DS} is evaluated from equation 4.8 if $V_T \leq V_{GS} \leq V_{GSAT}$ and from equation 4.9 if $V_{GS} \geq V_{GSAT}$. Once V_{DS} is known, the forward current, I_F , can be computed from equation 4.7.

Figure 4.3 is a graph of the forward current, I_F , versus the gate-to-source voltage, V_{GS} , for a supply voltage, V_{DD} , of 5 volts. The radiant power emitted from the LED, Φ_E , is equal to the product of the quantum efficiency, Q , and the forward current, I_F (equation 4.2). If the forward current exceeds the maximum-rated continuous forward current of the LED ($I_{FMAX} = 2 \text{ amps}$), then the duty cycle must be reduced accordingly (equation 4.1).

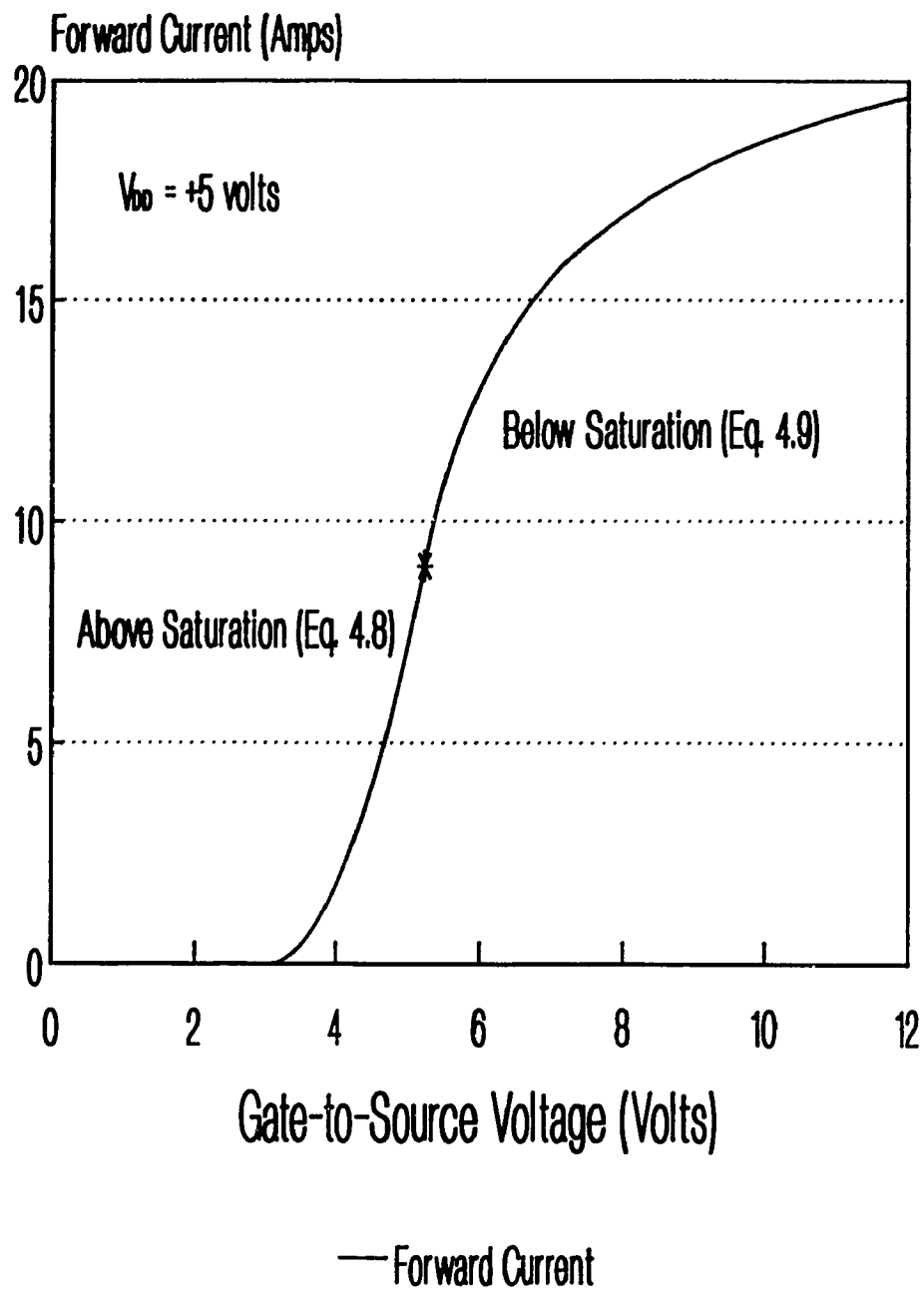


Figure 4.3: Forward current, I_F , versus Gate-to-Source voltage, V_{GS} , for the LED-MOSFET combination shown in Figure 4.2.

4.3.3 Optics and Geometry

The radiant intensity distribution of the LED is approximately hemispherical. This is necessary to ensure that the target LED is visible from any viewing angle. However, as a direct result, only a small fraction of the total radiant power emitted from the LED ever reaches the detector. This fraction is dependent on the distance between the target LED and detector, the geometry of the lens, and the transmittance of the lens-filter combination.

The irradiance, E_R , at a distance r from an ideal point source with a hemispherical radiant intensity distribution is given by:

$$E_R = \frac{\Phi_E}{2 \pi r^2} \quad (4.10)$$

where Φ_E is the total radiant power emitted from the source. The radiant flux incident on the sensitive surface of the PSD, Φ_S , is a function of the irradiance, E_R , the entrance pupil of the lens, A_p , and the transmittance of the lens-filter combination, τ , (approximately 0.5).

$$\Phi_S = E_R \cdot A_p \cdot \tau \quad (4.11)$$

The entrance pupil area, A_p , can be computed from the relative aperture, a_r , and the focal length, L_f , of the

lens.

$$A_p = \pi \left(\frac{L_F}{2 \cdot a_R} \right)^2 \quad (4.12)$$

The lens used in this study has a relative aperture of 1.6 and a focal length of 16 mm which yields an entrance pupil area of $7.854 \times 10^{-5} \text{ m}^2$.

4.3.4 Position Sensitive Detector

The Position Sensitive Detector (PSD) can be modeled as a first-order system with a time constant, τ_D , of 10.47 microseconds:

$$\frac{I_D}{\Phi_S} = \frac{R_e}{1 + \tau_D s} \quad (4.13)$$

The input, Φ_S , is the radiant flux incident on the sensitive surface of the PSD (equation 4.11); the output, I_p , is the total photocurrent generated; and the gain, R_e , is the responsivity of the PSD at a wavelength of $0.93 \text{ } \mu\text{m}$ (0.52 A/W).

4.3.5 Analog Position Processing Circuit

The intensity signal, Σ , which is generated by the Analog Position Processing Circuit, is related to the photocurrent, I_p , by a first-order transfer function (equations 3.2 and 3.3).

$$\frac{\Sigma}{I_p} = \frac{2 \cdot K_3 \cdot K_2 \cdot K_1}{1 + \tau_1 s} \quad (4.14)$$

Gains K_3 and K_2 are 0.47 and 20 respectively; K_1 is equal to 1.0×10^5 V/A and the time constant, τ_1 , is equal to 2.2 microseconds. The intensity signal, Σ , serves as a feedback to the intensity control circuit.

4.3.6 Control Strategy

A block diagram of the Intensity Control Circuit is shown in Figure 4.4. In the preceding sections, a mathematical model of each component of the circuit was formulated. Based on this model, a suitable control strategy can now be selected.

The simplest control strategy is proportional control whereby the Gate-to-Source voltage of the MOSFET, V_{GS} , is proportional to the difference between the feedback and setpoint signals.

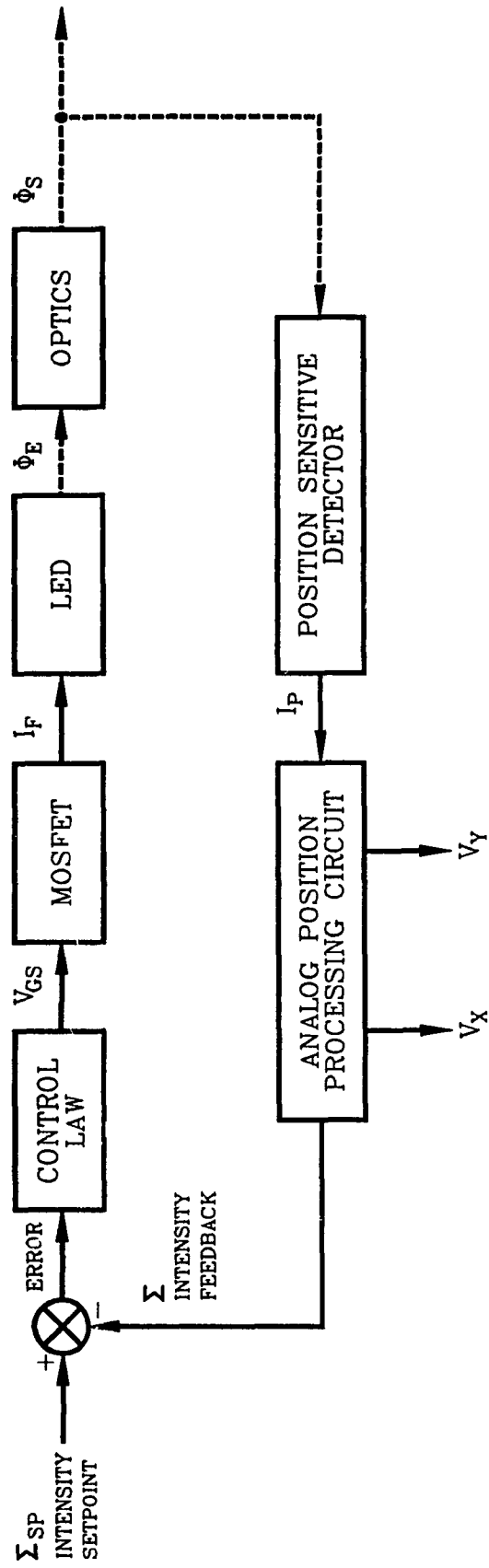


Figure 4.4: Block Diagram of the Intensity Control Circuit.

$$V_{GS} = K \cdot \left(\Sigma_{SP} - \Sigma \right) \quad (4.15)$$

In practice equation 4.15 is realized with an operational amplifier circuit. If the gain K is large or the frequency of operation high, then the dynamics of the operational amplifier (op amp) must be considered. The Gain-Bandwidth Product (GBW) of an op amp is defined as the frequency at which the open-loop gain equals unity. If the op amp is connected as a negative feedback amplifier with a gain of K , then the closed-loop bandwidth, B_{CL} , is given by:

$$B_{CL} = \frac{GBW}{K} \quad (4.16)$$

and the amplifier can be accurately modeled by the following first-order transfer function:

$$\frac{V_{OUT}}{V_{IN}} = \frac{K}{1 + \tau_A s} \quad (4.17)$$

where

$$\tau_A = \frac{1}{2\pi B_{CL}} \quad (4.18)$$

The op amp used in this study is a JFET input wide band amplifier with a gain-bandwidth product of 4.5 MHz (National Semiconductor LF356A).

4.4 Simulation Results

The MIMIC Digital Simulation Language was used to model the Intensity Control Circuit. The desired intensity signal, Σ_{SP} , was set at 3.5 volts. This is the highest value of intensity that can be readily maintained throughout the entire operating envelope of the system. The nominal LED forward current, I_F , corresponding to this value of intensity is 13.8 amps.

Figure 4.5 shows the time domain step response of the Intensity Control Circuit using proportional control with gain K equal to 10 and 30. A complete listing of the program used to generate these results appears in Appendix 3.

If a proportional gain of 10 is used, the settling time is excellent (approximately 30 microseconds). The steady-state error, however, is unacceptable (0.6 volts). If the gain is increased to 30, the steady-state error is accordingly reduced, however, this results in instability as shown in Figure 4.5.

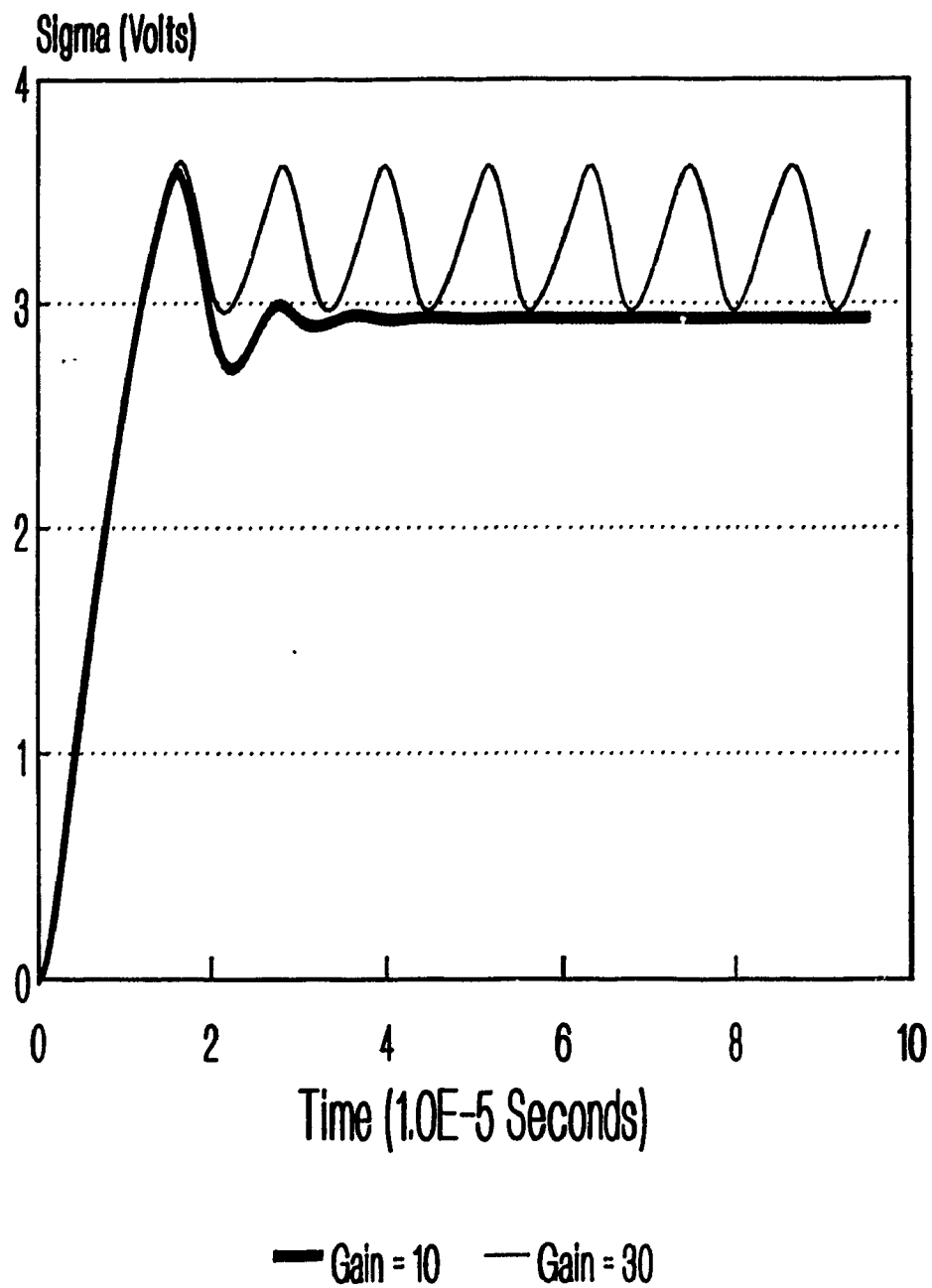


Figure 4.5: Step Response of the Intensity Control Circuit with Proportional Control.

An alternative means of reducing steady-state error is by introducing integral control whereby the Gate-to-Source voltage of the MOSFET, V_{GS} , is made proportional to the integral of the error between the feedback and setpoint signals:

$$V_{GS} = K \cdot \int \left(\Sigma_{SP} - \Sigma \right) dt \quad (4.19)$$

Figure 4.6 illustrates the response of the Intensity Control Circuit using integral control with gain K equal to 1×10^4 , 5×10^4 , and $1 \times 10^5 \text{ s}^{-1}$. This control strategy reduces the steady-state error to zero, however, it also increases the settling time to approximately 150 microseconds. Although this delay is tolerable, a control strategy can be implemented which effectively reduces the settling time without introducing steady-state error.

4.4.1 Nonlinear Control Strategy

Before any useful measurement data can be acquired, a certain delay must be incurred to allow for the settling time of the Intensity Control Circuit. Since the LEDs are pulsed sequentially, this delay accumulates and reduces the length of time available to calculate the position and orientation of the rigid body from the image coordinates of the body-fixed LEDs.

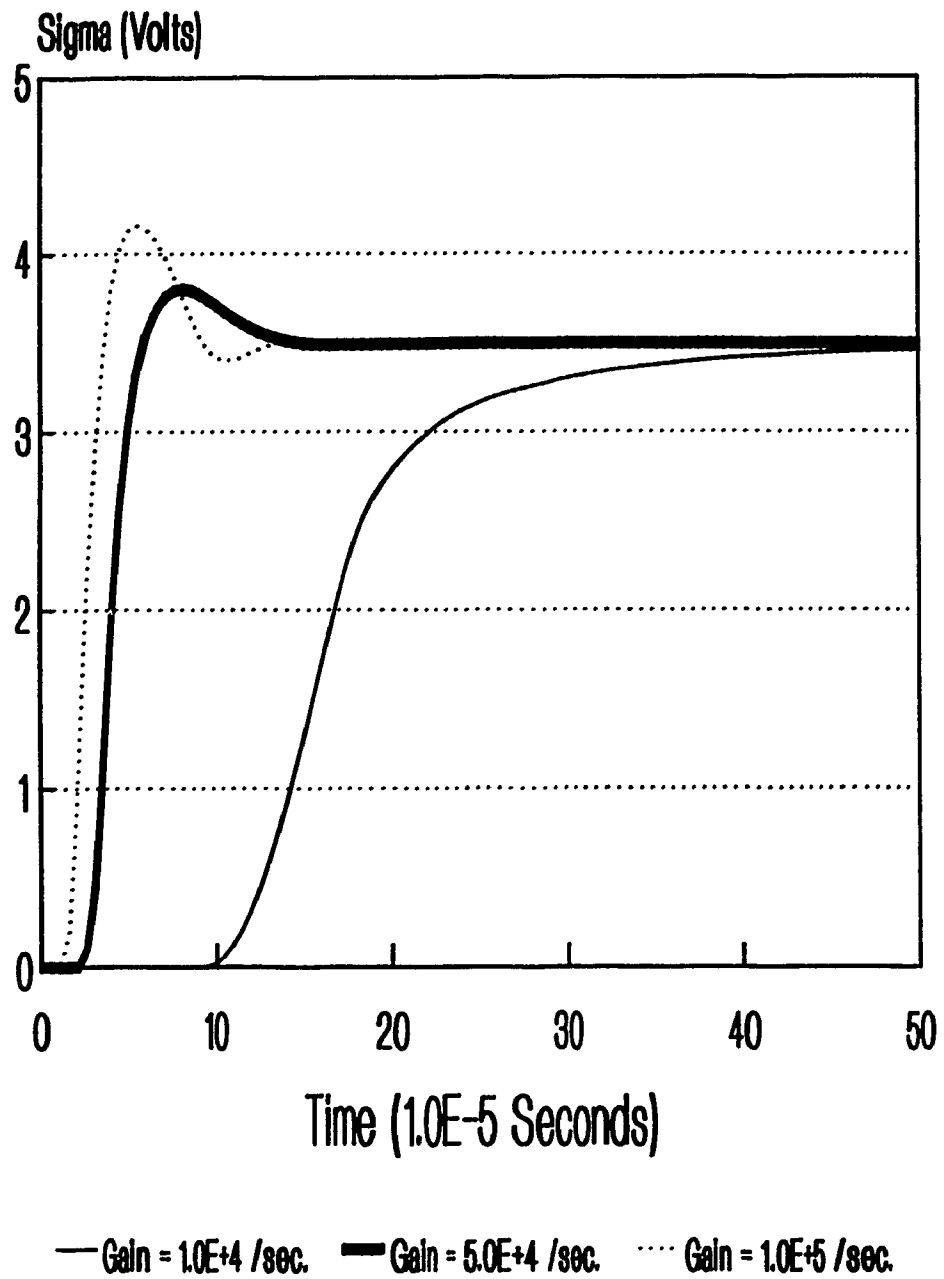


Figure 4.6: Step Response of the Intensity Control Circuit with Integral Control.

When an LED is selected, the Gate-to-Source voltage of the MOSFET, V_{GS} , must increase rapidly to the value required to maintain the Intensity Signal, Σ , at the setpoint value (i.e. 3.5 volts). If the motion of the rigid body is relatively slow, however, the steady-state value of V_{GS} does not vary significantly between successive pulses of the LED. Consequently, if the final value of V_{GS} is held during the interval of time that the LED is off, a significant improvement in the settling time of the Intensity Control Circuit can be achieved. An integral control strategy with a relatively low gain can be used since the controller does not have to integrate from zero but from the previous value of V_{GS} .

Figure 4.7 is a simplified representation of the circuit used to implement the nonlinear control strategy described above. When S_0 and S_1 are both in position 0, the Gate-to-Source voltage of the MOSFET, V_{GS} , is 0 and the LED is off. Since the inputs to the operational amplifier are disconnected, the charge on capacitor C_1 is held (neglect resistor R_3 for the time being). When S_0 and S_1 are switched to position 1, the output of the operational amplifier is applied to the gate terminal of the MOSFET resulting in a forward current through the LED. Resistors R_1 and R_2 are connected to the input of the operational amplifier and any discrepancy between the setpoint and feedback values is

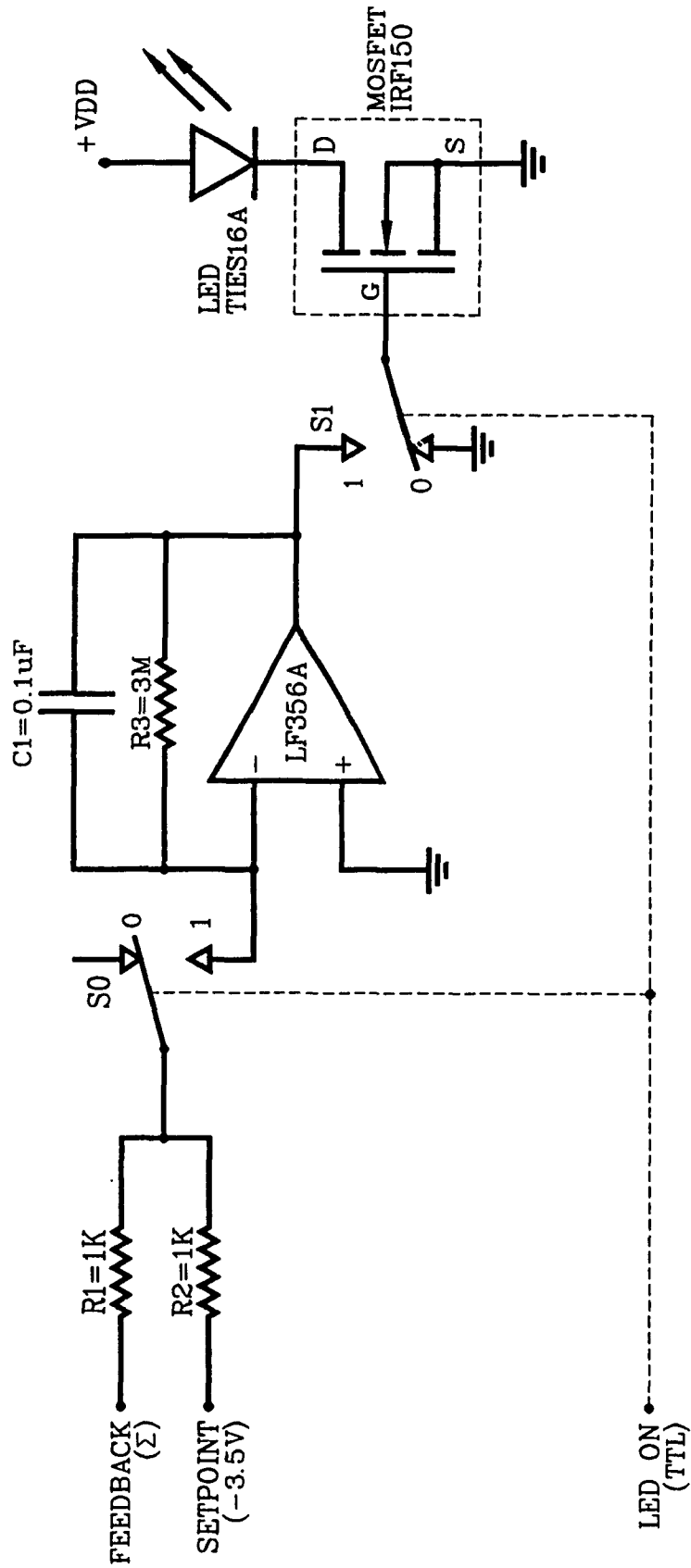


Figure 4.7: Simplified representation of circuit used to implement the nonlinear control strategy.

corrected by the integral action of the circuit.

Resistor R_3 is used to compensate for the time constant of the PSD (10.47 $\mu\text{sec.}$). Since the PSD does not respond instantaneously, there is an initial discrepancy between the feedback and setpoint signals at the instant the LED is selected. This discrepancy, which is present even if the applied value of V_{CS} is correct, causes the circuit to overshoot the desired value of V_{CS} . By inserting resistor R_3 , capacitor C_1 is slowly discharged during the time interval that the LED is off. When the LED is switched on, the initial discrepancy between the feedback and setpoint signals tends to restore V_{CS} to the correct value.

Figure 4.8 illustrates the response of the Intensity Control Circuit with nonlinear control. The middle curve corresponds to the case where the LED has remained stationary at a range of 1.0969 meters from the detector during the time interval that the LED was off. In this case, the Intensity Signal, Σ , reaches the setpoint value of 3.5 volts in under 100 $\mu\text{sec.}$ The top curve corresponds to the case where the LED has moved 16.2 mm closer to the detector in the time interval when the LED was off and that the value of V_{CS} held on capacitor C_1 is slightly high. Similarly, the bottom curve corresponds to the case where the LED has moved 16.2 mm further from the detector in the time interval when the LED was off and that the value of V_{CS} held on capacitor

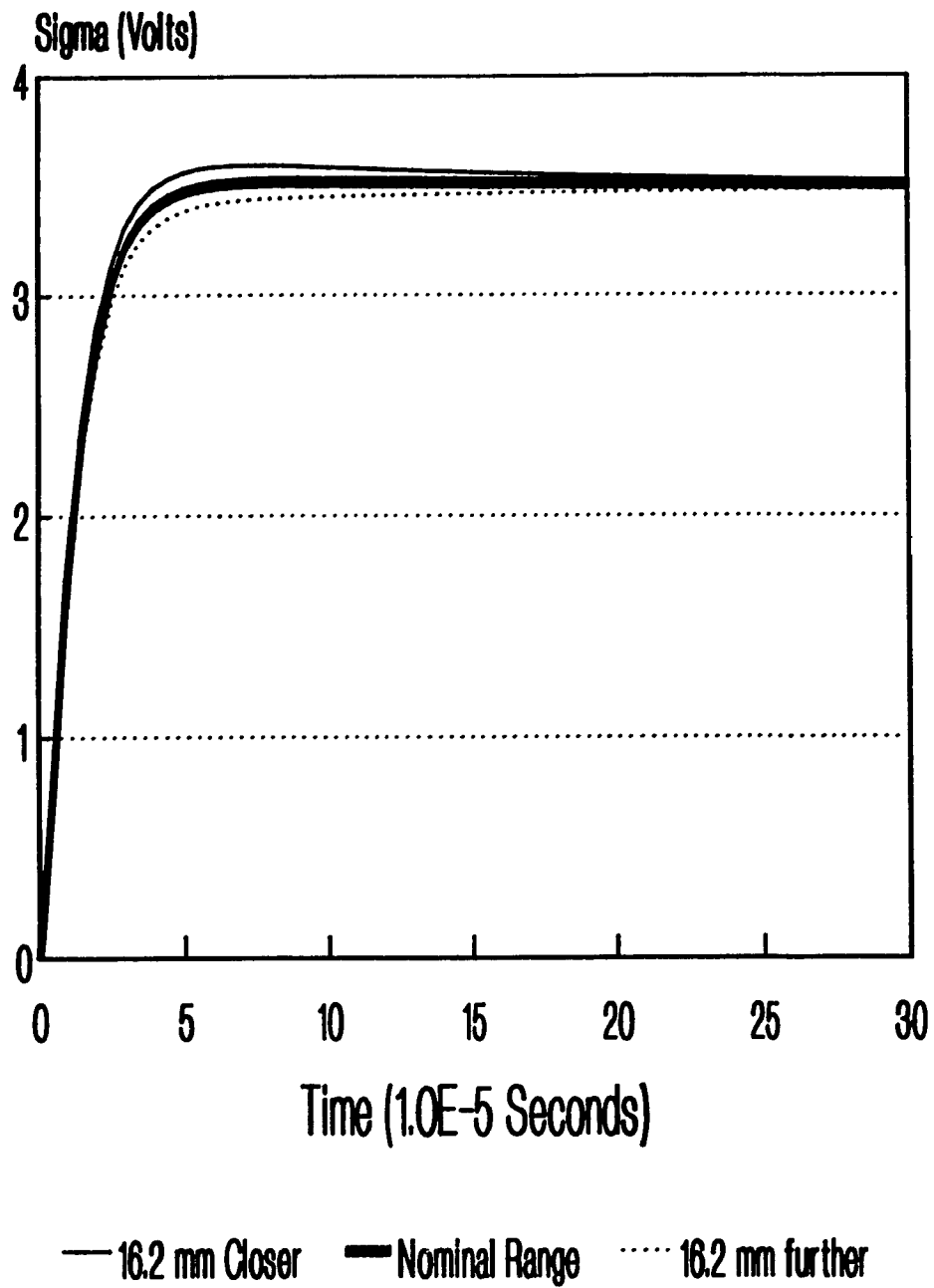


Figure 4.8: Step Response of the Intensity Control Circuit with Nonlinear Control.

C_1 is slightly low. A displacement of 16.2 mm corresponds to the LED travelling at the maximum possible helmet velocity for a period of 16.6 msec. (i.e. one frame). In all three cases the circuit performs adequately, that is, a relatively fast settling time with little or no overshoot.

4.5 System Configuration

Figure 4.9 is a schematic representation of the Optical Position Measurement System. Two Position Sensor Heads are directed at a pattern of six LEDs which is fixed to the rigid body. The single board computer selects the first LED in the sequence and initiates conversion on the A to D board. At the end of conversion the processor stores the coordinates of the LED image in memory and proceeds to process the next LED.

As stated above, the current through each LED is controlled so as to maintain a constant intensity irrespective of the position or orientation of the pattern. Figure 4.10a illustrates the intensity output signal, Σ_1 , of Position Sensor Head 1 (PSH 1). When Σ_1 is used as a feedback signal by the Intensity Control Circuit, the steady-state value of Σ_1 remains constant for all six LEDs. The intensity output signal of PSH 2, however, varies depending on the distance between the LED and the sensor (Figure 4.10b).

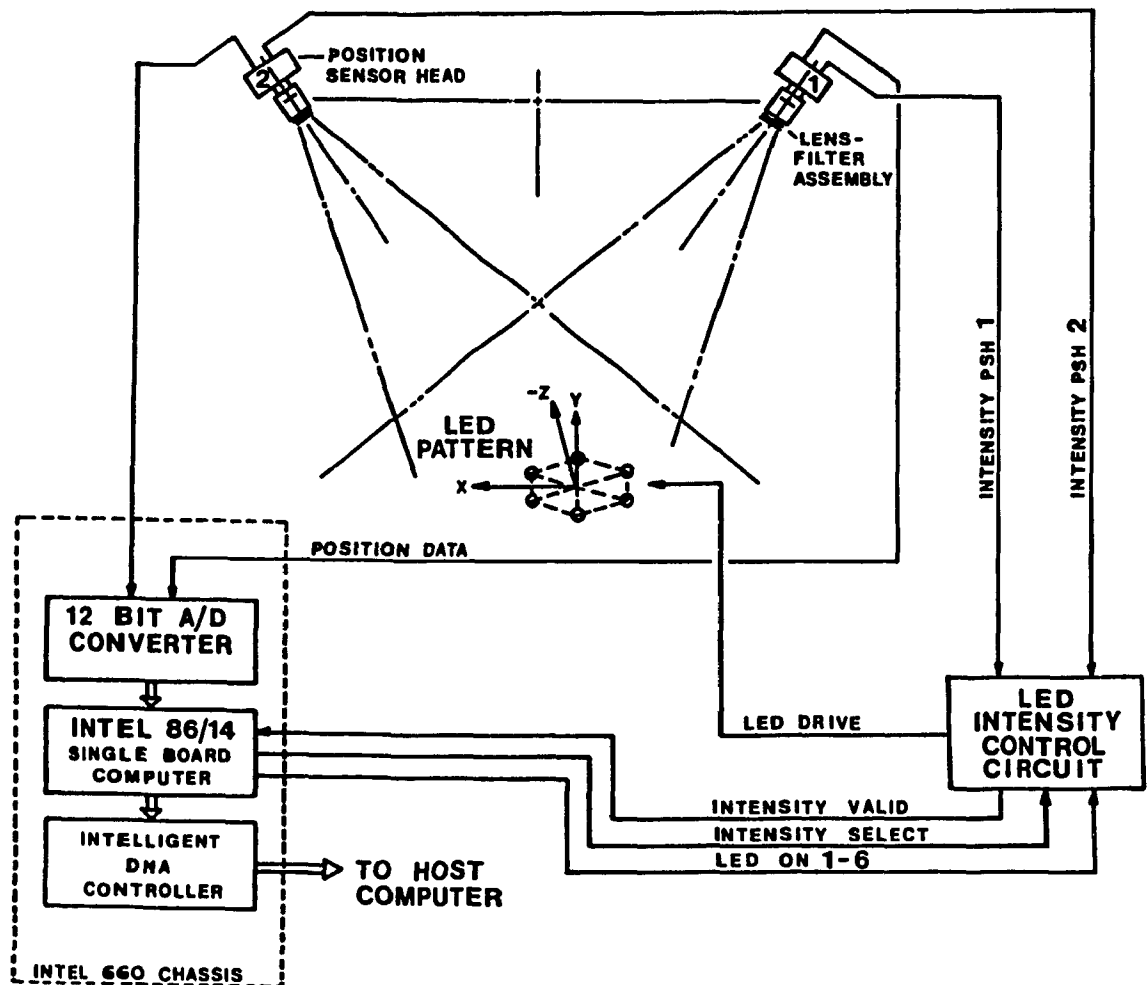
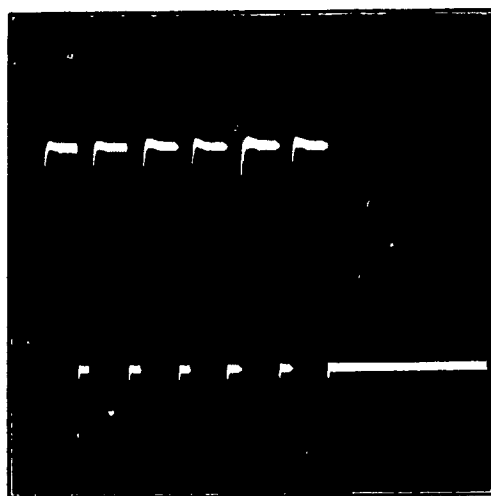
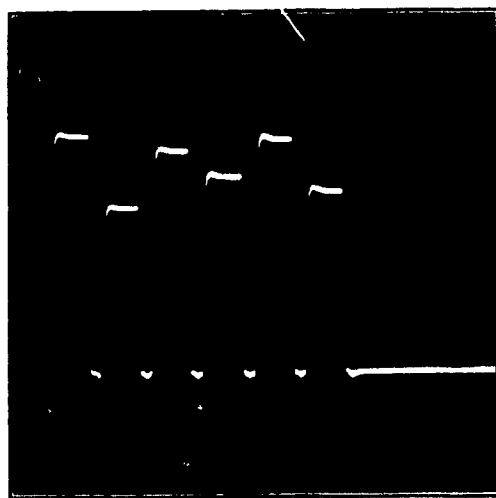


Figure 4.9: Block diagram of Optical Position Measurement System.

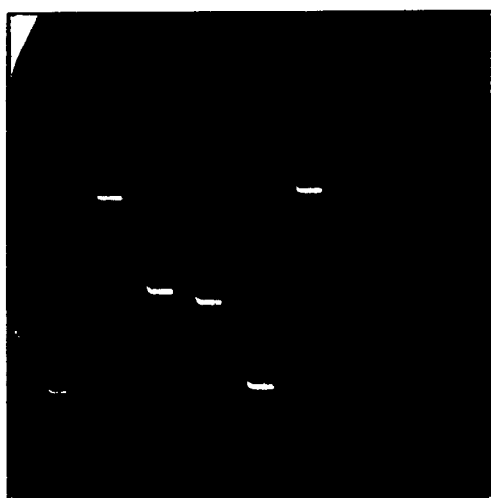
This difficulty is overcome by providing the single board computer with the capability of selecting either Σ_1 or Σ_2 as a feedback signal. The corresponding position output signals from PSH 1, V_{x1} and V_{y1} , are shown in Figures 4.10c and 4.10d respectively.



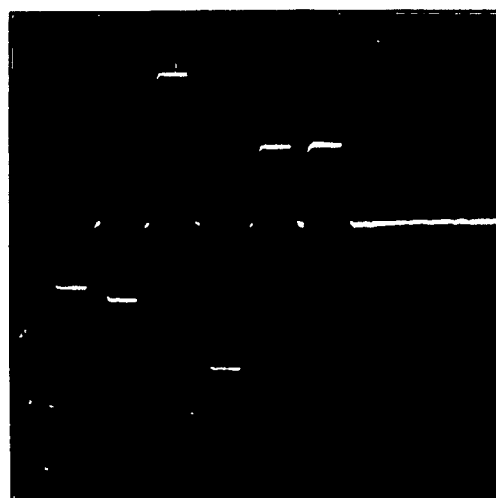
(a)



(b)



(c)



(d)

Sensitivity: 0.5 volts / division (vertical)
Timebase: 0.5 msec. / division (horizontal)

Figure 4.10a: Intensity Output Signal, Σ_1 , of PSH 1.
b: Intensity Output Signal, Σ_2 , of PSH 2.
c: Position Output Signal, V_{x1} , of PSH 1.
d: Position Output Signal, V_{y2} , of PSH 1.

CHAPTER 5

LENS-SENSOR MODEL

5.1 Introduction

The lens-sensor assembly is modeled as an ideal, linear camera (Figure 5.1). Each point (i.e. LED) in the viewing space is projected toward the focal center of the lens and onto the sensitive surface of the detector. The resulting image is a two-dimensional perspective projection of an LED moving in three-dimensional space. Consequently, the three-dimensional position of the LED cannot be recovered from its image coordinates alone. At best, only the direction of the vector between the LED and the sensor can be determined. If the target LED is viewed from two different locations, a triangulation scheme can be used to compute the LED's position in three-dimensions. The objective of this analysis is to find the three-dimensional, cartesian coordinates of an LED in space given two perspective views of that LED.

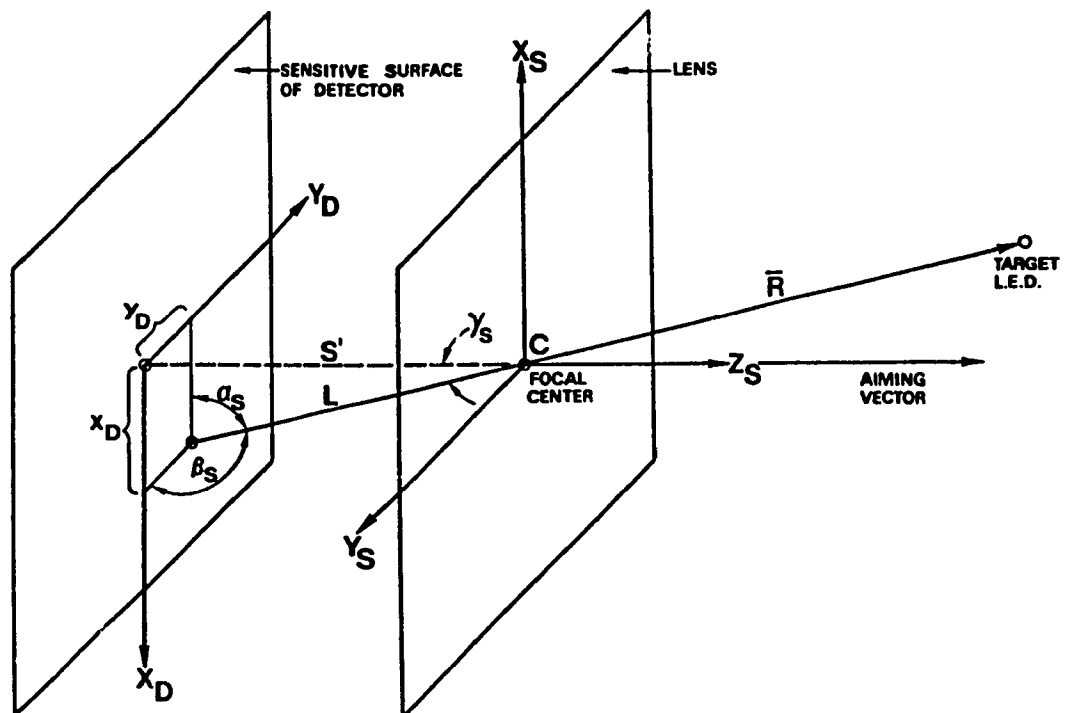


Figure 5.1: Schematic representation of lens-sensor assembly.

5.2 Perspective Geometry

The vector between the LED and the corresponding point on the sensitive surface of the detector always passes through the focal center, C. For this reason, the origin of the sensor coordinate system is located at point C. The orientation is such that the positive Z axis is coincident with the aiming vector of the lens. The sensitive surface of the detector is parallel to, and at a distance S' from, the $X_s - Y_s$ plane. The distance S' varies with the focal setting of the lens.

The location of the LED image on the sensitive surface of the detector is defined by two coordinates; x_D and y_D . These coordinates are proportional to the output voltage signals provided by the sensor.

$$\begin{aligned}x_D &= G_x V_x \\y_D &= G_y V_y\end{aligned}\tag{5.1}$$

The sensitivities G_x and G_y are approximately equal to 1 mm/volt. The sensor output signals, V_x and V_y , are both equal to zero if the target LED is located on the aiming vector of the lens. These signals increase in magnitude to a maximum of 5 volts as the LED image moves towards the edge of the sensitive surface.

Since the image plane is located behind the focal center of the lens, the image is inverted. This is taken into account by reversing the direction of the X_D and Y_D axes as shown in Figure 5.1.

The vector \vec{R} defines the position of the target LED with respect to the focal center of the lens. The angles α_s , β_s , and γ_s are formed by the vector \vec{R} and the X_s , Y_s , and Z_s axes respectively. The cosines of these angles are referred to as the direction cosines of \vec{R} with respect to the sensor coordinate system. The three direction cosines are synonymous with the components of a unit vector having the same direction as \vec{R} . They can be expressed as functions of x_D , y_D , and S' as follows:

$$\begin{aligned}\cos\alpha_s &= x_D / L \\ \cos\beta_s &= y_D / L \\ \cos\gamma_s &= S' / L\end{aligned}\tag{5.2}$$

$$\text{where:} \quad L = \sqrt{S'^2 + x_D^2 + y_D^2}$$

As expected, these functions satisfy the condition:

$$\cos^2\alpha_s + \cos^2\beta_s + \cos^2\gamma_s = \frac{S'^2 + x_D^2 + y_D^2}{S'^2 + x_D^2 + y_D^2} = 1$$

The vector \vec{R} is completely specified by its length, which is as yet unknown, and its direction cosines.

$$\vec{R} = |\vec{R}| (\cos\alpha_s \vec{i}_s + \cos\beta_s \vec{j}_s + \cos\gamma_s \vec{k}_s) \quad (5.3)$$

5.3 Sensing Range

The image coordinates, x_D and y_D , do not change as the target LED moves along the straight line passing through the focal center of the lens. Consequently, additional "depth cues" are required to determine the length of the vector \vec{R} . In a structured environment, these cues are provided by the geometric constraints. For example, if a number of LEDs are fixed to a rigid body then, by definition, the distance between any two LEDs remains constant for all times and for all configurations. This rigidity constraint can be used to determine the three-dimensional position of each LED from a single perspective view. In the discipline of photogrammetry, this is referred to as a single camera resection. This method of determining range is applicable to the Optical Position Sensing System and will be described in a chapter 7.

Range information can also be obtained by monitoring the intensity signal provided by the Position Sensor Head. This signal is proportional to the radiant flux incident on the sensitive surface of the detector. If the LED power output is held constant, then the radiant flux at the detector is

inversely proportional to the square of the distance between the LED and the focal center of the lens. Unfortunately, the radiant flux at the detector is also dependent on the angle between the line of sight and the optical axis of the LED. As a result, variations in the intensity signal can be attributed to either a pure rotation of the LED or a change in the distance between the LED and the focal center of the lens. The intensity signal can only be used to gauge the distance to an ideal point source with a perfectly spherical intensity distribution [32]. Since an ideal point source exists only in theory, the intensity signal cannot be relied on to provide accurate range information.

5.3.1 Sensing Range By Triangulation

The lens-sensor assembly provides enough information to compute the line of sight passing through both the focal center of the lens and the target LED. If the same LED is viewed from a second location, then its position in three-dimensional space is fixed by the intersection of the two lines of sight. This method of determining range is referred to as triangulation and is the method of choice for the Optical Position Measurement System.

Several computer vision systems have been devised which extract three-dimensional information from a stereo pair of

TV cameras [33] [34]. In order to operate at the frame rate of the cameras, these systems require high-performance data acquisition and image processing capabilities. The two video signals must be digitized, the target points identified, and the correspondence between points determined before triangulation can be applied. Determining the correspondence involves matching points in the two images by means of a correlation algorithm. This is a time consuming operation which only provides a reliable match if the disparity between the two images is minimal. The disparity can be decreased by bringing the two viewpoints closer together but not without reducing the accuracy of the range determination. The correspondence problem is further complicated by the disappearance of target points due to the rotation of the rigid body.

In the case of the Optical Position Measurement System, the target LEDs are illuminated sequentially. Since only one point (i.e. LED) is visible to the sensors at any given time, the correspondence between the two images is known. The three-dimensional position of the target LED can be computed directly from the output signals of the two sensors. Since there is no need to match points by means of a correlation algorithm, the disparity between the images can be increased in order to maximize the accuracy of the range determination. The two intensity signals can be used

to detect if the LED is outside the field of view of the sensors or if one of the lines of sight is obstructed.

Figure 5.2 shows the general configuration of the Optical Position Measurement System. Two rigidly connected sensors are directed at an array of three or more target LEDs which are illuminated sequentially. The sensors have a baseline separation d and are angled towards one another in order to maximize the common field of view.

The origin of the fixed coordinate system is arbitrarily placed at the focal center of lens 1. The negative X axis of this coordinate system is coincident with the vector joining the focal centers of the two lenses. This vector, which is denoted by \vec{V}_B , can be written in terms of the fixed unit vectors \vec{i} , \vec{j} , \vec{k} as follows:

$$\vec{V}_B = \begin{bmatrix} -d \\ 0. \\ 0. \end{bmatrix}^T \begin{bmatrix} \vec{i} \\ \vec{j} \\ \vec{k} \end{bmatrix}$$

The vectors \vec{R}_{s1} and \vec{R}_{s2} define the position of the illuminated LED with respect to the coordinate systems of sensors 1 and 2 respectively. As demonstrated previously, the direction of the vector \vec{R}_{s1} can be computed from the image coordinates of sensor 1 (i.e. x_{d1} and y_{d1}). Similarly, the direction of \vec{R}_{s2} can be computed from x_{d2} and y_{d2} . The

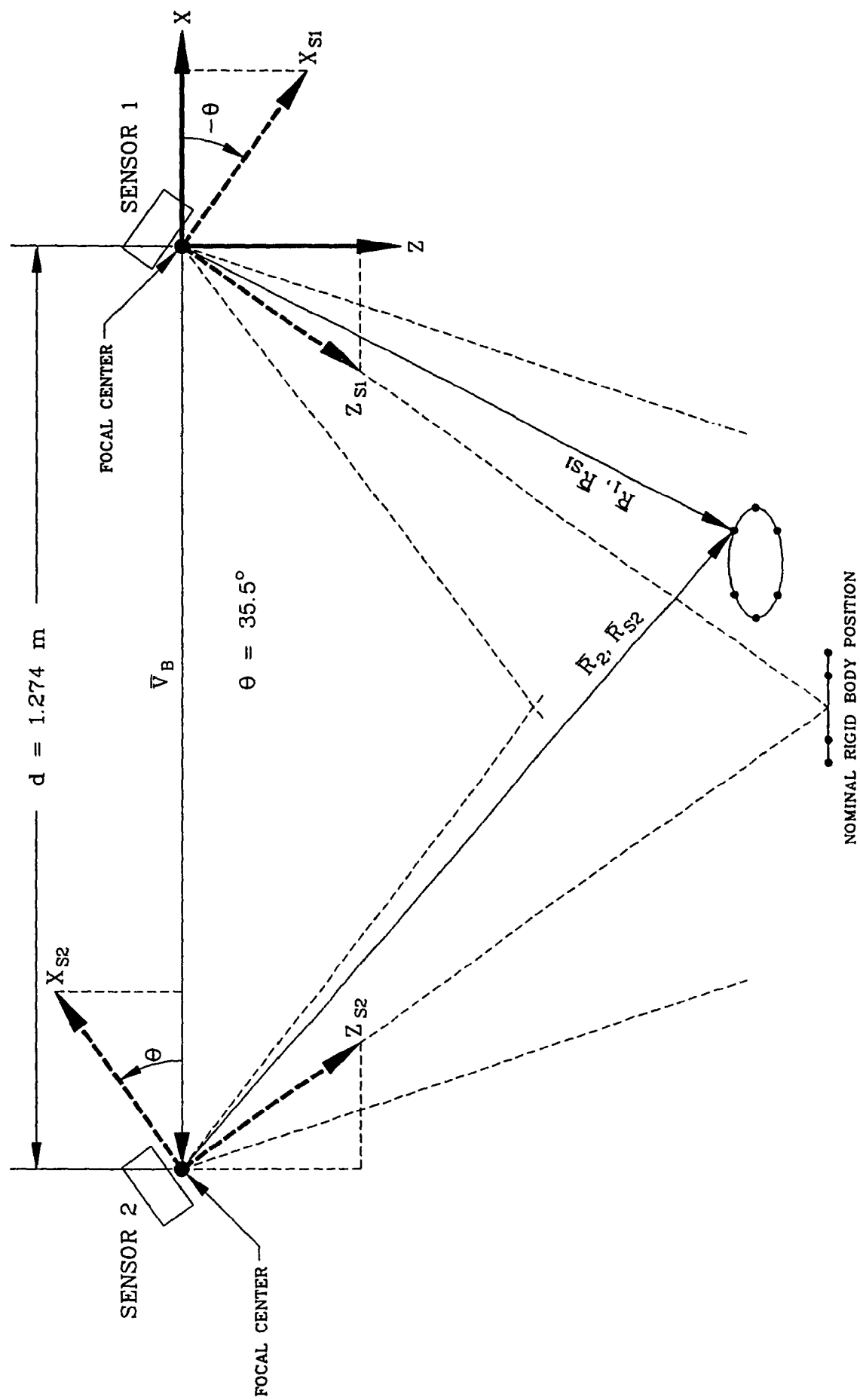


Figure 5.2: General configuration of the Optical Position Measurement System.

length of both of these vectors can be derived from the following vector relationship.

$$\vec{R}_{S1} = \vec{V}_B + \vec{R}_{S2} \quad (5.4)$$

The position vectors \vec{R}_{S1} and \vec{R}_{S2} must be written in terms of the fixed unit vectors \vec{i} , \vec{j} , \vec{k} before the vector addition in equation 5.4 can be performed. This involves multiplying each vector by an orthogonal rotation matrix which relates the unit vectors of the appropriate sensor coordinate system to those of the fixed coordinate system.

As shown in Figure 5.2, a right-handed rotation about the positive Y axis in the amount $-\theta$ defines the coordinate system of sensor 1. The unit vectors of this coordinate system (i.e. \vec{i}_{S1} , \vec{j}_{S1} , \vec{k}_{S1}) can be written in terms of the fixed unit vectors \vec{i} , \vec{j} , \vec{k} as follows:

$$\begin{aligned}
\vec{i}_{s1} &= \cos(\theta)\vec{i} + (0.)\vec{j} + \sin(\theta)\vec{k} \\
\vec{j}_{s1} &= (0.)\vec{i} + (1.)\vec{j} + (0.)\vec{k} \\
\vec{k}_{s1} &= -\sin(\theta)\vec{i} + (0.)\vec{j} + \cos(\theta)\vec{k}
\end{aligned}$$

$$\begin{bmatrix} \vec{i}_{s1} \\ \vec{j}_{s1} \\ \vec{k}_{s1} \end{bmatrix} = \begin{bmatrix} T_1 \end{bmatrix} \begin{bmatrix} \vec{i} \\ \vec{j} \\ \vec{k} \end{bmatrix} \quad (5.5)$$

$$\text{where } \begin{bmatrix} T_1 \end{bmatrix} = \begin{bmatrix} \cos(\theta) & 0. & \sin(\theta) \\ 0. & 1. & 0. \\ -\sin(\theta) & 0. & \cos(\theta) \end{bmatrix}$$

The rotation matrix which relates the coordinate system of sensor 2 to the fixed coordinate system can be derived in a similar manner.

$$\begin{aligned}
\vec{i}_{s2} &= \cos(\theta)\vec{i} + (0.)\vec{j} - \sin(\theta)\vec{k} \\
\vec{j}_{s2} &= (0.)\vec{i} + (1.)\vec{j} + (0.)\vec{k} \\
\vec{k}_{s2} &= \sin(\theta)\vec{i} + (0.)\vec{j} + \cos(\theta)\vec{k}
\end{aligned}$$

$$\begin{bmatrix} \vec{i}_{s2} \\ \vec{j}_{s2} \\ \vec{k}_{s2} \end{bmatrix} = \begin{bmatrix} T_2 \end{bmatrix} \begin{bmatrix} \vec{i} \\ \vec{j} \\ \vec{k} \end{bmatrix} \quad (5.6)$$

$$\text{where } [T_2] = \begin{bmatrix} \cos(\theta) & 0. & -\sin(\theta) \\ 0. & 1. & 0. \\ \sin(\theta) & 0. & \cos(\theta) \end{bmatrix}$$

The rotation matrices $[T_1]$ and $[T_2]$ carry the position vectors \vec{R}_{s1} and \vec{R}_{s2} into the fixed coordinate system.

$$\begin{aligned} \vec{R}_1 &= \vec{R}_{s1} [T_1] \\ \vec{R}_2 &= \vec{R}_{s2} [T_2] \end{aligned} \quad (5.7)$$

The vectors \vec{R}_1 and \vec{R}_2 differ by the vector constant \vec{v}_B .

$$\vec{R}_1 = \vec{v}_B + \vec{R}_2$$

or in terms of the direction cosines:

$$|\vec{R}_1| \begin{bmatrix} \cos\alpha_1 \\ \cos\beta_1 \\ \cos\gamma_1 \end{bmatrix}^T \begin{bmatrix} \vec{i} \\ \vec{j} \\ \vec{k} \end{bmatrix} = \begin{bmatrix} -d \\ 0. \\ 0. \end{bmatrix}^T \begin{bmatrix} \vec{i} \\ \vec{j} \\ \vec{k} \end{bmatrix} + |\vec{R}_2| \begin{bmatrix} \cos\alpha_2 \\ \cos\beta_2 \\ \cos\gamma_2 \end{bmatrix}^T \begin{bmatrix} \vec{i} \\ \vec{j} \\ \vec{k} \end{bmatrix} \quad (5.8)$$

By collecting the coefficients of the fixed unit vectors \vec{i} , \vec{j} , \vec{k} a system of three equations in two unknowns can be formulated.

$$\begin{aligned}
|\vec{R}_1| \cos \alpha_1 - |\vec{R}_2| \cos \alpha_2 &= -d & (a.) \\
|\vec{R}_1| \cos \beta_1 - |\vec{R}_2| \cos \beta_2 &= 0 & (b.) \\
|\vec{R}_1| \cos \gamma_1 - |\vec{R}_2| \cos \gamma_2 &= 0 & (c.)
\end{aligned} \tag{5.9}$$

The two unknowns, \vec{R}_1 and \vec{R}_2 , can be determined by solving equations a and b or a and c simultaneously (equations b and c are not independent).

$$\begin{aligned}
|\vec{R}_1| &= \frac{d \cos \gamma_2}{\cos \alpha_2 \cos \gamma_1 - \cos \alpha_1 \cos \gamma_2} \\
|\vec{R}_2| &= \frac{d \cos \gamma_1}{\cos \alpha_2 \cos \gamma_1 - \cos \alpha_1 \cos \gamma_2}
\end{aligned} \tag{5.10}$$

The vector \vec{R}_1 , which represents the position of the illuminated LED with respect to the fixed coordinate system, is completely defined by its length (equation 5.10) and its direction cosines (equations 5.2 and 5.7).

5.4 Summary

This chapter details a procedure for determining the three-dimensional position of an LED from a stereo pair of two-dimensional images. The equations which describe the measurement process are derived on the assumption of a linear camera model. This simple model is valid for most

corrected camera lenses (wide angle, high aperture lenses excluded).

Unlike most stereo imaging systems, the Optical Position Measurement System is not disposed to the low-level problems of image segmentation, correspondence, occlusion, etc. The unique, three-dimensional position of an LED can be readily determined by triangulation.

CHAPTER 6

FORMULATION OF ALGORITHMS

6.1 Introduction

In the previous chapter, a procedure for computing the three-dimensional, cartesian coordinates of a number of points (i.e. LEDs) in space was described. Since three generalized coordinates are necessary and sufficient to specify the position of a single unconstrained point in space, a system of n unconstrained points requires $3n$ coordinates to uniquely define its kinematic state. If the points represent particles of a rigid body then the system is constrained and fewer generalized coordinates are required.

In general, a system of n points subject to L independent holonomic constraints is uniquely defined by $(3n-L)$ generalized coordinates. In the case of a rigid body, the distance between any two points is fixed for all times and for all configurations. This yields exactly $(3n-6)$ independent constraints for $n \geq 3$. Therefore, exactly $3n-(3n-6)=6$ generalized coordinates are required to uniquely define the kinematic state of a rigid body in three-dimensional space [13].

The rigidity constraints reduce the dimension of the configuration space from $3n$ to 6. Nevertheless there exists a wide choice as to the specific quantities to be used in the kinematic description of the rigid body. For instance, the kinematic configuration can be completely specified by the cartesian coordinates of three noncolinear points.

A more convenient scheme is suggested by Euler's theorem which states that the most general displacement of a rigid body with a fixed point A is equivalent to a rotation of that body about an axis through A [35]. In order to apply this theorem, a cartesian triad of unit vectors with origin at point A is fixed to the rigid body. Three generalized coordinates are required to describe the translation of point A with respect to a fixed (Galilean) frame. An additional three coordinates define the rotation of the body-fixed triad about A.

In the mathematical analysis of the mechanical position measurement system, the translation of the point A is defined by the vector \vec{V}_{OA} . The remaining three coordinates are obtained from the transformation matrix [T] which relates the body coordinate system to the fixed coordinate system. This kinematic description is the most appropriate since it best represents the geometry of the mechanical system. The measured variables represent angular displacements, therefore the simplest procedure is to

evaluate the orthogonal rotation matrices corresponding to each joint of the linkage, and then compute the equivalent transformation matrix $[T]$.

In the case of the optical position measurement system, the measured variables represent rectilinear displacements. Therefore a kinematic analysis based on rotation matrices and Euler angles is not appropriate. A different choice of generalized coordinates could conceivably simplify the problem. The problem can be summarized as follows. Given the cartesian coordinates of a minimum of three points, determine the orientative parameters which relate the body coordinate system to the fixed coordinate system. Two methods of solution are considered; the vector equation method and the statistical (Schut) method.

The vector equation method utilizes the cartesian coordinates of exactly three noncolinear points to determine the orientation of the rigid body. If ideal point coordinate data is available, then the vector equation method constitutes the simplest and most efficient means of computing the orientative parameters.

The statistical method acknowledges the inaccuracies in the measurement data. It employs regression analysis to find the orientative parameters which best describe the kinematic state of any number of body-fixed points. In order to minimize the computational effort, the regression model

should be linear in terms of the orientative parameters. The choice of generalized coordinates is therefore critical.

If the regression model is formulated in terms of Euler angles, the resulting equations contain terms which involve the product of transcendental functions. Finding a closed-form solution for such a system of nonlinear equations is very difficult. Consequently, the use of a numerical technique is mandated. In reference 36, Roach and Aggarwal address the problem of determining the three-dimensional model and movement of an object from a sequence of noisy images. A modified finite difference Levenberg-Marquardt algorithm [37] [38] is used to minimize the least-squared error of 18 nonlinear equations. Considerable computational effort is required (in the order of 15 seconds on a Cyber 170/75). This clearly demonstrates the need for a linear regression model when working in a real-time environment. The remainder of the chapter is devoted to the derivation of just such a model.

6.2 The Rodrigues Formulas

As stated previously, the most general displacement of a rigid body with a fixed point A is equivalent to a rotation of that body about an axis through A. In the analysis which follows, the axis through A is represented by the unit vector \vec{n} and the amount of rotation is given by the

angle θ . The Rodrigues vector, denoted by $\vec{\rho}$, has direction \vec{n} and magnitude $\tan(\theta/2)$. Thus the vector $\vec{\rho}$ contains all the information necessary to describe the orientation of the rigid body [39]. Both the vector equation method and the statistical (Schut) method are formulated in terms of the Rodrigues vector.

It will be shown that the components of the Rodrigues vector constitute a set of generalized coordinates which are particularly well suited to the problem under consideration. Nevertheless there are a number of difficulties associated with the use of these coordinates. For instance, there is the question of human perception. It is difficult to visualize the kinematic state of a rigid body given the components of the Rodrigues vector. Of greater significance is the problem of calibration. While the Euler angles can be accurately generated using a standard device such as a dividing head, there is no simple way of generating the components of the Rodrigues vector. Consequently, the orientation of the rigid body must be expressed in terms of a more appropriate set of coordinates. This can be accomplished by deriving the matrix of direction cosines in terms of the Rodrigues vector. The Euler angles can then be calculated from the elements of this matrix (refer to chapter 2).

Figure 6.1 is a schematic representation of a rigid body in three-dimensional space. The point P is fixed to the body. The vector \vec{r} defines the position of P with respect to a fixed reference frame with origin at point O. The body is rotated through an angle θ about the axis defined by the unit vector \vec{n} . As a result of the rotation, the point P is displaced to P'. This displacement is represented by the vector $\vec{\Delta r}$. The angle between the vectors \vec{r} and \vec{n} is denoted by α .

The vector \vec{q} represents the component of \vec{r} normal to \vec{n} . Since \vec{n} has unit length, the magnitude of \vec{q} can be expressed as the vector product of \vec{n} and \vec{r} .

$$|\vec{q}| = |\vec{r}| \sin\alpha = |\vec{n} \times \vec{r}| \quad (6.1)$$

The displacement vector $\vec{\Delta r}$ can be decomposed into two components, \vec{PB} and \vec{BP}' . Since the vector \vec{BP}' is normal to both \vec{n} and \vec{r} it has the direction $(\vec{n} \times \vec{r})$. Its magnitude is equal to $|\vec{q}| \sin\theta$ or by substituting $(\vec{n} \times \vec{r})$ from equation 6.1:

$$\vec{BP}' = \sin\theta (\vec{n} \times \vec{r}) \quad (6.2)$$

The component \vec{PB} is normal to both \vec{BP}' and \vec{n} consequently it has the direction $\vec{n} \times (\vec{n} \times \vec{r})$. Its magnitude is given by:

$$|\vec{PB}| = |\vec{q}| (1 - \cos\theta)$$

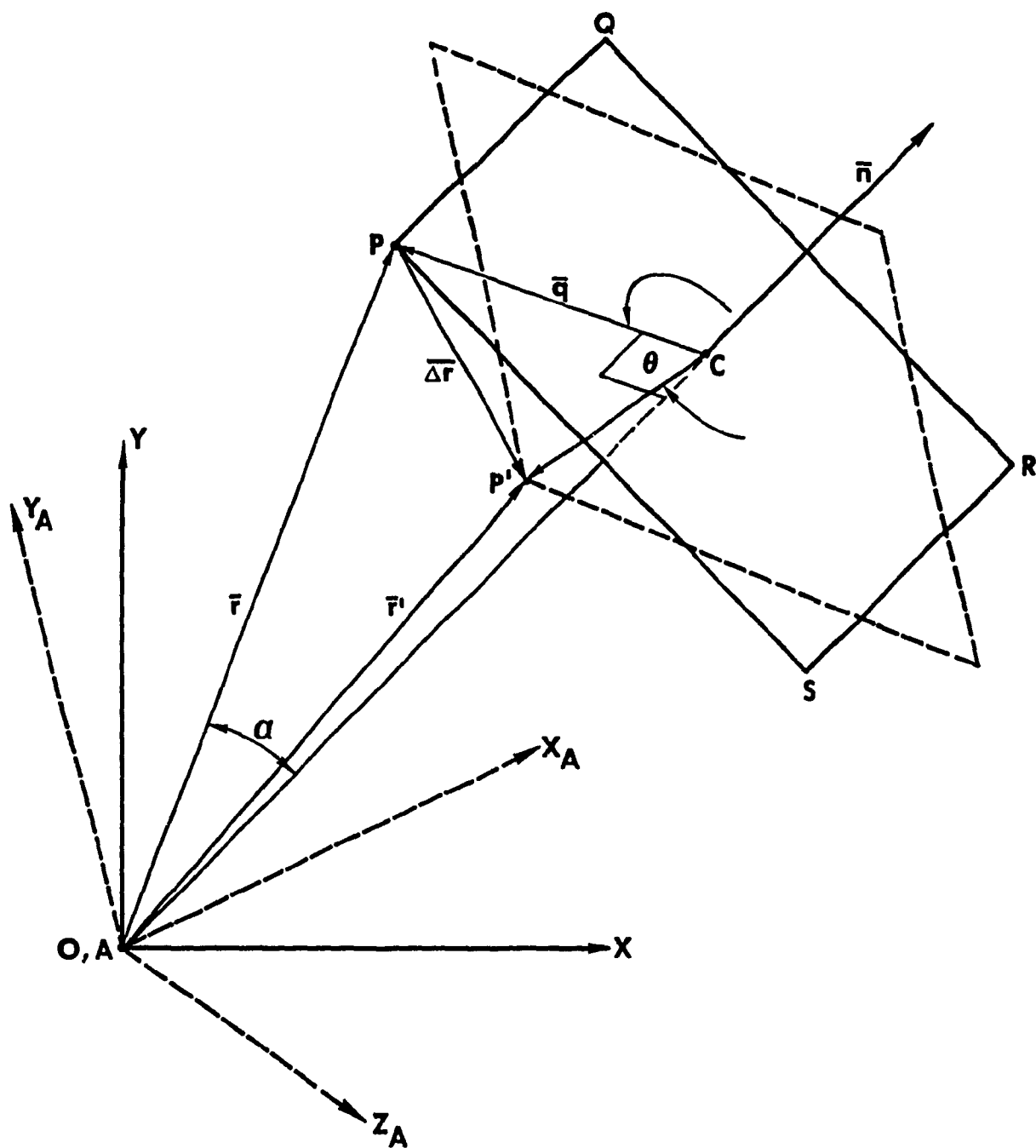


Figure 6.1: Schematic representation of Euler's theorem.



Since the unit vector \vec{n} is normal to $(\vec{n} \times \vec{r})$, the magnitude of \vec{q} can also be expressed as:

$$|\vec{q}| = |\vec{n} \times (\vec{n} \times \vec{r})|$$

Thus the vector \overrightarrow{PB} can also be written in terms of \vec{n} , \vec{r} and θ .

$$\begin{aligned}\overrightarrow{PB} &= (1 - \cos\theta) [\vec{n} \times (\vec{n} \times \vec{r})] \\ &= 2\sin^2(\theta/2) [\vec{n} \times (\vec{n} \times \vec{r})]\end{aligned}\quad (6.3)$$

The displacement vector $\overrightarrow{\Delta r}$ is equal to the vector sum of its components, i.e.

$$\begin{aligned}\overrightarrow{\Delta r} &= \overrightarrow{PB} + \overrightarrow{BP}' \\ &= 2\sin^2(\theta/2) [\vec{n} \times (\vec{n} \times \vec{r})] + \sin\theta(\vec{n} \times \vec{r})\end{aligned}\quad (6.4)$$

The Rodrigues vector was previously defined as having direction and magnitude $\tan(\theta/2)$.

$$\vec{\rho} = \tan(\theta/2) \vec{n} \quad (6.5)$$

The trigonometric functions in equation 6.4 can be expressed in terms of the Rodrigues vector $\vec{\rho}$ as follows:

$$\sin\theta = 2\sin(\theta/2)\cos(\theta/2) = \frac{2\tan(\theta/2)}{1+\tan^2(\theta/2)} = \frac{2|\vec{\rho}|}{1+|\vec{\rho}|^2}$$

$$\sin^2(\theta/2) = \frac{\tan^2(\theta/2)}{1+\tan^2(\theta/2)} = \frac{|\vec{\rho}|^2}{1+|\vec{\rho}|^2}$$

Substituting the above expressions into equation 6.4:

$$\begin{aligned}\overrightarrow{\Delta r} &= \frac{2|\vec{\rho}|^2}{1+|\vec{\rho}|^2} [\vec{n} \times (\vec{n} \times \vec{r})] + \frac{2|\vec{\rho}|}{1+|\vec{\rho}|^2} (\vec{n} \times \vec{r}) \\ \overrightarrow{\Delta r} &= \frac{2}{1+|\vec{\rho}|^2} [\vec{\rho} \times (\vec{\rho} \times \vec{r}) + (\vec{\rho} \times \vec{r})] \quad (6.6)\end{aligned}$$

The vector $\overrightarrow{\Delta r}$ defines the displacement of the point P following a change in orientation of the rigid body, i.e.

$$\begin{aligned}\overrightarrow{\Delta r} &= \vec{r}' - \vec{r} \\ \vec{r}' &= \frac{2 [\vec{\rho} \times (\vec{\rho} \times \vec{r}) + (\vec{\rho} \times \vec{r})] + [1 + |\vec{\rho}|^2] \vec{r}}{1 + |\vec{\rho}|^2} \quad (6.7)\end{aligned}$$

Let the components of the vectors \vec{r}' , \vec{r} and $\vec{\rho}$ be represented by:

$$\begin{aligned}\vec{r}' &= x' \vec{i} + y' \vec{j} + z' \vec{k} \\ \vec{r} &= x \vec{i} + y \vec{j} + z \vec{k} \\ \vec{\rho} &= \rho_1 \vec{i} + \rho_2 \vec{j} + \rho_3 \vec{k}\end{aligned}$$

By carrying out the vector arithmetic and collecting the coefficients of \vec{i} , \vec{j} and \vec{k} , equation 6.7 can be written in matrix form.

$$[r'] = \begin{bmatrix} x \\ y \\ z \end{bmatrix}^T \frac{\begin{bmatrix} 1+\rho_1^2-\rho_2^2-\rho_3^2 & 2(\rho_1\rho_2+\rho_3) & 2(\rho_1\rho_3-\rho_2) \\ 2(\rho_1\rho_2-\rho_3) & 1-\rho_1^2+\rho_2^2-\rho_3^2 & 2(\rho_2\rho_3+\rho_1) \\ 2(\rho_1\rho_3+\rho_2) & 2(\rho_2\rho_3-\rho_1) & 1-\rho_1^2-\rho_2^2+\rho_3^2 \end{bmatrix}}{1 + \rho_1^2 + \rho_2^2 + \rho_3^2} \begin{bmatrix} \vec{i} \\ \vec{j} \\ \vec{k} \end{bmatrix} \quad (6.8)$$

The vector \vec{r} represents the position, relative to the fixed reference frame, of the point P prior to rotation. This is analogous to defining a body coordinate system which is initially coincident with the fixed reference frame. The components of the vector \vec{r} with respect to this coordinate system are given by:

$$\vec{r} = x\vec{i}_A + y\vec{j}_A + z\vec{k}_A$$

The transformation matrix given in equation 6.8 relates \vec{i}_A , \vec{j}_A , and \vec{k}_A to the fixed reference frame.

$$\begin{bmatrix} \vec{i}_A \\ \vec{j}_A \\ \vec{k}_A \end{bmatrix} = [T] \begin{bmatrix} \vec{i} \\ \vec{j} \\ \vec{k} \end{bmatrix}$$

$$\text{where } [T] = \frac{\begin{bmatrix} 1+\rho_1^2-\rho_2^2-\rho_3^2 & 2(\rho_1\rho_2+\rho_3) & 2(\rho_1\rho_3-\rho_2) \\ 2(\rho_1\rho_2-\rho_3) & 1-\rho_1^2+\rho_2^2-\rho_3^2 & 2(\rho_2\rho_3+\rho_1) \\ 2(\rho_1\rho_3+\rho_2) & 2(\rho_2\rho_3-\rho_1) & 1-\rho_1^2-\rho_2^2+\rho_3^2 \end{bmatrix}}{1 + \rho_1^2 + \rho_2^2 + \rho_3^2}$$

Therefore, the elements of the matrix $[T]$ represent the direction cosines expressed in terms of the Rodrigues vector $\vec{\rho}$. The kinematic state of the rigid body can be expressed in terms of the Euler angles by applying equation 2.19.

$$\alpha = \text{ATAN2}(T_{12}, T_{11})$$

$$\beta = \text{ATAN2}(T_{23}, T_{33})$$

$$\gamma = \text{ASIN}(-T_{13})$$

6.3 The Vector Equation Method

The Rodrigues vector $\vec{\rho}$ contains all the information necessary to describe the orientation of a rigid body. The vector $\vec{\rho}$ can be found by substituting the cartesian coordinates of three noncolinear points into a single vector equation. The derivation of this equation follows.

Figure 6.2 is a normal view of the plane PQRS. The displacement vector $\vec{\Delta r}$ is given by:

$$\vec{\Delta r} = \tan(\theta/2) \vec{PD}$$

The vector \vec{PD} is equal to the vector sum of $(\vec{rx}\vec{r})$ and $(\vec{rx}\vec{r}')$, therefore:

$$\begin{aligned}
\vec{\Delta r} &= \tan(\theta/2) \{ (\vec{n} \times \vec{r}') + (\vec{n} \times \vec{r}) \} \\
\vec{\Delta r} &= \tan(\theta/2) \{ \vec{n} \times (\vec{r}' + \vec{r}) \} \\
\vec{\Delta r} &= \vec{r}' - \vec{r} = \vec{\rho} \times (\vec{r}' + \vec{r})
\end{aligned} \tag{6.10}$$

Equation 6.10 describes the rotation of the vector \vec{r} through an angle θ about the axis \vec{n} . Two such equations are required in order to compute the Rodrigues vector $\vec{\rho}$.

Let A be a body-fixed point on the axis of rotation. The vectors \vec{r}_1 and \vec{r}_2 define the position of points P_1 and P_2 with respect to A. After rotation these vectors become \vec{r}'_1 and \vec{r}'_2 . For convenience, the following notation is adopted.

$$\begin{aligned}
\vec{r}'_1 + \vec{r}_1 &= \vec{a}_1 \\
\vec{r}'_1 - \vec{r}_1 &= \vec{b}_1 \\
\vec{r}'_2 + \vec{r}_2 &= \vec{a}_2 \\
\vec{r}'_2 - \vec{r}_2 &= \vec{b}_2
\end{aligned}$$

Equation 6.10 relates \vec{b}_1 to \vec{a}_1 and \vec{b}_2 to \vec{a}_2 as follows.

$$\begin{aligned}
\vec{b}_1 &= \vec{\rho} \times \vec{a}_1 \\
\vec{b}_2 &= \vec{\rho} \times \vec{a}_2
\end{aligned}$$

The vector product of \vec{b}_1 and \vec{b}_2 is given by:

$$\begin{aligned}
\vec{b}_1 \times \vec{b}_2 &= (\vec{\rho} \times \vec{a}_1) \times (\vec{\rho} \times \vec{a}_2) \\
&= \{\vec{\rho} \cdot (\vec{a}_1 \times \vec{a}_2)\} \vec{\rho} - \{\vec{\rho} \cdot (\vec{a}_1 \times \vec{\rho})\} \vec{a}_2 \quad (6.11)
\end{aligned}$$

Since $\vec{\rho}$ is perpendicular to $(\vec{a}_1 \times \vec{\rho})$, the second term in equation 6.11 is equal to zero. Therefore,

$$\begin{aligned}
\vec{b}_1 \times \vec{b}_2 &= \{\vec{\rho} \cdot (\vec{a}_1 \times \vec{a}_2)\} \vec{\rho} \\
&= - \{\vec{a}_1 \cdot (\vec{\rho} \times \vec{a}_2)\} \vec{\rho} \\
&= - (\vec{a}_1 \cdot \vec{b}_2) \vec{\rho}
\end{aligned}$$

Thus the Rodrigues vector $\vec{\rho}$ is given by:

$$\vec{\rho} = \frac{\vec{b}_2 \times \vec{b}_1}{\vec{a}_1 \cdot \vec{b}_2} \quad (6.12)$$

Equation 6.12 provides a simple means of computing the Rodrigues vector $\vec{\rho}$ from the cartesian coordinates of three noncolinear points [39] [40].

The components of the Rodrigues vector are only one of several possible choices of "screw parameters" which can be used to specify the spatial displacement of a rigid body. The problem of determining screw parameters from the initial and final coordinates of three noncollinear points has attracted the attention of many researchers [41] [42]. A number of algorithms for this purpose have been developed in recent years. These algorithms, although based on different concepts, yield equivalent results. The primary differences

are in their computational efficiency, computational accuracy, and sensitivity to inexact position data.

The method based on Rodrigues' formula is both computationally efficient and insensitive to measurement error in the position data. Other techniques, notably Angeles' method and the method proposed by Laub and Shiflett [43], provide superior computational accuracy. These methods will not be presented in this thesis, however. Instead, the emphasis will be on techniques for determining the screw parameters from the initial and final coordinates of three or more body-fixed points.

6.4 The Schut Method

The science of photogrammetry is concerned with the determination of structure or spacial orientation from one or more photographic images. Typically, photogrammetric techniques are applied to topographic mapping of the earth's surface. In the construction of a map, a number of independent images or models are connected to form a continuous strip. Traditionally, strips are formed by analog triangulation on a stereoscopic plotter [44]. A viable alternate to this is the numerical formation of strips.

In this scheme, a reference coordinate system is arbitrarily established with respect to the first model.

Each subsequent model is mathematically rotated and, if necessary, scaled so that it matches the first model. The mathematical formulation of the rotation is of particular interest in this study.

It has been shown that the cartesian coordinates of a point before and after rotation can be related through a set of linear equations. The coefficients of these equations are the nine entries in the matrix of direction cosines. The nine direction cosines can be expressed as functions of three independent parameters (i.e. generalized coordinates). Unfortunately, these functions are always nonlinear and an iterative procedure must be used to compute the three orientative parameters.

In reference 45, Thompson derives a set of exact linear equations for computing the three independent parameters which describe the orientation of a model or strip. This formulation is computationally efficient in comparison with conventional nonlinear methods, however the coefficients of the equations are complicated and a solution by the method of least squares is not recommended.

Thompson's most significant discovery was that the problem of absolute orientation could be reduced to the solution of a system of linear equations. This led Schut to derive a set of four simple equations which are homogeneous with respect to four parameters [46]. Only the ratios of the

four parameters are defined, thus they represent three independent quantities. Schut's equations are extremely simple; one coefficient in each is equal to zero and the others are linear functions of the point coordinates before and after rotation. If these equations are solved by the method of least squares, then the coefficients of the resulting normal equations can be expressed as simple functions of the point coordinates.

Schut's method was initially applied to the numerical formation of strips from independent models [47]. Since then it has been used in the solution of a wide variety of photogrammetric problems. In reference 48, Lenox describes the development of a clinical procedure for the measurement and analysis of human eyeball movement. Close-range photogrammetric techniques are employed to determine the coordinates of a minimum of three points on the eyeball's surface. Schut's method is then used to compute the eyeball's position and orientation from the coordinate data. Lenox concludes that Schut's method should be applied to all problems involving measured point coordinate data.

Since most photogrammetric problems involve the off-line processing of data, even a small improvement in accuracy will usually justify an increase in computing time. This is not necessarily the case in a real-time environment. In the work described in this thesis, the applicability of

Schut's method to a real-time measurement system was investigated.

6.4.1 Derivation of the Schut Equations

In reference 46 Schut presents a set of exact linear equations for computing the rotational parameters which describe the orientation of a model or strip. These simple equations are derived in two ways. The first derivation is based on elementary matrix algebra and leads to three equations. The second derivation employs quaternion algebra and results in a complete set of four linear equations. Only the second more thorough derivation will be presented here. Since the algebra of quaternions is not widely known, a brief introduction is in order.

Let the set $A = \{1, \vec{i}, \vec{j}, \vec{k}\}$ be a basis of a vector space V of dimension four over the set of real numbers. The first element in the set is the scalar unit 1. The other three elements are mutually perpendicular unit vectors which obey the following laws of combination [49].

$$\begin{aligned}
 \vec{i}^2 &= \vec{j}^2 = \vec{k}^2 = -1 \\
 \vec{i}\vec{j} &= \vec{k}, \quad \vec{j}\vec{i} = -\vec{k} \\
 \vec{j}\vec{k} &= \vec{i}, \quad \vec{k}\vec{j} = -\vec{i} \\
 \vec{k}\vec{i} &= \vec{j}, \quad \vec{i}\vec{k} = -\vec{j}
 \end{aligned}
 \tag{6.13}$$

The quaternion q is a linear combination of the elements of the basis A , i.e.

$$q = d + a\vec{i} + b\vec{j} + c\vec{k}, \quad a, b, c, d \in \mathbb{R} \quad (6.14)$$

Every nonzero quaternion has a multiplicative inverse given by:

$$q^{-1} = \frac{q^*}{q q^*} \quad (6.15)$$

$$\text{where } q^* = d - a\vec{i} - b\vec{j} - c\vec{k} \quad (6.16)$$

The quaternions q^{-1} and q^* are referred to as the reciprocal and conjugate of q respectively [50] [51].

Consider the following quaternion expression:

$$\vec{r}' = q \vec{r} q^{-1} \quad (6.17)$$

The vectors \vec{r}' and \vec{r} are given by:

$$\vec{r}' = x'\vec{i} + y'\vec{j} + z'\vec{k}$$

$$\vec{r} = x\vec{i} + y\vec{j} + z\vec{k}$$

In this analysis, a vector is equivalent to a quaternion whose scalar part d is equal to zero. By performing the indicated multiplications and collecting the coefficients of 1 , \vec{i} , \vec{j} and \vec{k} , equation 6.17 can be written in matrix form.

$$[\mathbf{r}'] = \frac{\begin{bmatrix} x \\ y \\ z \end{bmatrix}^T \begin{bmatrix} d^2 + a^2 - b^2 - c^2 & 2(ab+cd) & 2(ac-bd) \\ 2(ab-cd) & d^2 - a^2 + b^2 - c^2 & 2(bc+ad) \\ 2(ac+bd) & 2(bc-ad) & d^2 - a^2 - b^2 + c^2 \end{bmatrix} \begin{bmatrix} \hat{i} \\ \hat{j} \\ \hat{k} \end{bmatrix}}{a^2 + b^2 + c^2 + d^2} \quad (6.18)$$

Since the coefficient of the scalar component in equation 6.18 is equal to zero, \vec{r}' is a vector.

If the substitutions $a=\rho_1$, $b=\rho_2$, $c=\rho_3$ and $d=1$ are made, then the matrix in equation 6.18 is exactly equal to the transformation matrix $[T]$ given by equation 6.8. Consequently, the quaternion equation 6.17:

$$\vec{r}' = q \vec{r} q^{-1}$$

is equivalent to the previously derived Rodrigues formula. That is it represents a rotation in three-dimensional space about an axis through the origin. If both sides of this equation are multiplied by q , then:

$$\vec{r}' q = q \vec{r} \quad (6.19)$$

Since this is a statement of equality between two quaternions, their corresponding components must be equal. There are four components, hence four equations which are linear with respect to the parameters a , b , c and d . These equations can be found by performing the two multiplications and collecting the coefficients of 1 , \hat{i} , \hat{j} and \hat{k} .

$$\begin{aligned}
1 &\longrightarrow -ax' - by' - cz' = -ax - by - cz \\
\vec{i} &\longrightarrow dx' - bz' + cy' = dx - cy + bz \\
\vec{j} &\longrightarrow dy' + az' - cx' = cx + dy - az \\
\vec{k} &\longrightarrow dz' - ay' + bx' = -bx + ay + dz
\end{aligned} \tag{6.20}$$

Further simplification is possible by collecting terms of the same parameter, i.e.

$$\begin{aligned}
(x' - x)a + (y' - y)b + (z' - z)c &= 0 \\
- (z' + z)b + (y' + y)c + (x' - x)d &= 0 \\
(z' + z)a - (x' + x)c + (y' - y)d &= 0 \\
- (y' + y)a + (x' + x)b + (z' - z)d &= 0
\end{aligned} \tag{6.21}$$

Note that these homogeneous equations are not only linear in the parameters a , b , c and d but also in the point coordinates before and after rotation. The determinant of the matrix formed by the coefficients of the parameters equals zero, as does the determinant of every submatrix of order three, hence there are only two independent equations in this set.

A cursory study of Schut's equations suggests that a complete kinematic description can be obtained from the coordinates of only two points. This is clearly impossible from a kinematics standpoint since the rotation about the line joining the points cannot be detected. The apparent

contradiction can be easily explained.

According to Euler's theorem, a kinematic description must be formulated in terms of a fixed point A. By definition, this point remains stationary during a pure change in orientation. If only one body point is observed, then it is assumed to be fixed and all the coefficients of Schut's equations are equal to zero.

If two points are considered, then there are eight linear equations. Since one point must be selected as the fixed point A, the coefficients of four of the equations are equal to zero. Of the remaining equations, only two are independent. Therefore the orientative parameters cannot be determined. If three or more points are considered, then there are enough independent equations to obtain a solution.

In a more recent reference [47], Schut derives the identical set of four equations by considering the coordinate transformation of a point in four-dimensional space. Such a transformation can be represented by an orthogonal skew matrix of order four. Since the algebra of quaternions is nothing more than a convenient set of algorithms for the manipulation of such matrices, the two derivations are analogous.

6.4.2 Solution by the Method of Least Squares

Schut recommends that the rotational parameters be computed from the linear equations by the method of least squares. If all of the available equations are included in the regression model, then the coefficients of the resulting normal equations become very simple functions of the point coordinates before and after rotation. Thus it is preferable to use four equations per point even though only two are independent.

Let n represent the number of points included in the regression model. Schut's equations can be written in a more appropriate form by placing the coefficients of the rotational parameters into a matrix of order $4n$ by 4 .

$$\begin{bmatrix}
(x'_1 - x_1) & (y'_1 - y_1) & (z'_1 - z_1) & 0 \\
0 & -(z'_1 - z_1) & (y'_1 + y_1) & (x'_1 - x_1) \\
(z'_1 + z_1) & 0 & -(x'_1 + x_1) & (y'_1 - y_1) \\
-(y'_1 + y_1) & (x'_1 + x_1) & 0 & (z'_1 - z_1) \\
\hline
(x'_2 - x_2) & (y'_2 - y_2) & (z'_2 - z_2) & 0 \\
0 & -(z'_2 - z_2) & (y'_2 + y_2) & (x'_2 - x_2) \\
(z'_2 + z_2) & 0 & -(x'_2 + x_2) & (y'_2 - y_2) \\
-(y'_2 + y_2) & (x'_2 + x_2) & 0 & (z'_2 - z_2) \\
\hline
. & . & . & . \\
. & . & . & . \\
. & . & . & . \\
. & . & . & . \\
\hline
(x'_n - x_n) & (y'_n - y_n) & (z'_n - z_n) & 0 \\
0 & -(z'_n - z_n) & (y'_n + y_n) & (x'_n - x_n) \\
(z'_n + z_n) & 0 & -(x'_n + x_n) & (y'_n - y_n) \\
-(y'_n + y_n) & (x'_n + x_n) & 0 & (z'_n - z_n)
\end{bmatrix}
\begin{bmatrix} a \\ b \\ c \\ d \end{bmatrix} = \begin{bmatrix} 0 \\ 0 \\ 0 \\ 0 \\ . \\ . \\ . \\ . \\ 0 \\ 0 \\ 0 \\ 0 \end{bmatrix}
\tag{6.22}$$

In the subsequent analysis, the matrix of coefficients is denoted by $[A]$ and the vector of parameters by $[\beta]$.

Since equation 6.22 is overdetermined, a solution can only be found if exact coordinate data is used to compute the coefficients. In this study the coordinate data is subject to measurement error, therefore a single set of rotational parameters cannot satisfy all of the available

equations. An error term must be introduced into equation 6.22 in order to account for the inaccuracies in the measurement data.

$$[A] [\beta] = [\delta] \quad (6.23)$$

The error associated with each equation is contained in the column vector $[\delta]$. The objective is to find the parameters which minimize the vector $[\delta]$ given the coordinates of three or more points.

The square of the norm of $[\delta]$ can be conveniently represented by the following matrix equation.

$$\begin{aligned} [\delta]^T [\delta] &= ([A] [\beta])^T [A] [\beta] \\ &= [\beta]^T [A]^T [A] [\beta] \end{aligned} \quad (6.24)$$

The vector $[b]$ is the least squares estimate of $[\beta]$ which minimizes $[\delta]^T [\delta]$. It can be found by differentiating equation 6.24 with respect to $[\beta]$ and setting the resulting matrix equation equal to zero. Differentiating with respect to a vector quantity is equivalent to differentiating with respect to each element of the vector separately and arranging the results in matrix form. This provides the following set of normal equations [52].

$$\begin{aligned} [0] &= [A]^T [A] [b] \\ &= [S] [b] \end{aligned} \quad (6.25)$$

The matrix multiplication $[A]^T[A]$ results in a symmetric matrix of order four which is denoted by $[S]$. The elements of $[S]$ are simple functions of the point coordinates before and after rotation.

$$\begin{aligned}
 s_{11} &= \sum_{i=1}^n [(x'_i - x_i)^2 + (y'_i + y_i)^2 + (z'_i + z_i)^2] \\
 s_{22} &= \sum_{i=1}^n [(x'_i + x_i)^2 + (y'_i - y_i)^2 + (z'_i + z_i)^2] \\
 s_{33} &= \sum_{i=1}^n [(x'_i + x_i)^2 + (y'_i + y_i)^2 + (z'_i - z_i)^2] \\
 s_{44} &= \sum_{i=1}^n [(x'_i - x_i)^2 + (y'_i - y_i)^2 + (z'_i - z_i)^2] \\
 s_{12} &= s_{21} = -2 \sum_{i=1}^n (y_i x'_i + y'_i x_i) \\
 s_{13} &= s_{31} = -2 \sum_{i=1}^n (x_i z'_i + x'_i z_i) \\
 s_{23} &= s_{32} = -2 \sum_{i=1}^n (z_i y'_i + z'_i y_i) \\
 s_{14} &= s_{41} = 2 \sum_{i=1}^n (z_i y'_i - z'_i y_i) \\
 s_{24} &= s_{42} = 2 \sum_{i=1}^n (x_i z'_i - x'_i z_i) \\
 s_{34} &= s_{43} = 2 \sum_{i=1}^n (y_i x'_i - y'_i x_i)
 \end{aligned} \tag{6.26}$$

The four normal equations can be solved by applying Gaussian elimination to the matrix $[S]$. The reduced matrix $[S']$ is given by:

$$[S'] = \begin{bmatrix} s_{11} & s_{12} & s_{13} & s_{14} \\ 0 & s'_{22} & s'_{23} & s'_{24} \\ 0 & 0 & s'_{33} & s'_{34} \\ 0 & 0 & s'_{34} & s'_{44} \end{bmatrix} \quad (6.27)$$

where:

$$\begin{aligned} s'_{22} &= s_{22} - s_{12}s_{12}/s_{11} \\ s'_{23} &= s_{23} - s_{13}s_{12}/s_{11} \\ s'_{24} &= s_{24} - s_{14}s_{12}/s_{11} \\ s'_{33} &= s_{33} - s_{13}s_{13}/s_{11} - s'_{23}s'_{23}/s'_{22} \\ s'_{34} &= s_{34} - s_{14}s_{13}/s_{11} - s'_{24}s'_{23}/s'_{22} \\ s'_{44} &= s_{44} - s_{14}s_{14}/s_{11} - s'_{24}s'_{24}/s'_{22} \end{aligned} \quad (6.28)$$

Since only the ratios of the four parameters are defined, d can be arbitrarily set to 1 and the remaining parameters can be computed by means of backward substitution.

$$\begin{aligned} d &= 1 \\ c &= \rho_3 = -s'_{34}/s'_{33} \\ b &= \rho_2 = -(s'_{24} + s'_{23}c)/s'_{22} \\ a &= \rho_1 = -(s_{14} + s_{13}c + s_{12}b)/s_{11} \end{aligned} \quad (6.29)$$

6.5 Translation Measurement

Theoretically, any one of the measured points can be chosen as the origin of the body coordinate system. The translation of the rigid body is defined by the cartesian coordinates of this point. In reference 48, Lenox states that the point whose coordinate can be determined with the greatest accuracy is the three-dimensional mean of the measured points. This imaginary point, which is denoted by Q , is defined as:

$$\vec{Q} = Q_x \vec{i} + Q_y \vec{j} + Q_z \vec{k} \quad (6.30)$$

where:

$$Q_x = \sum_{i=1}^n x_i / n$$

$$Q_y = \sum_{i=1}^n y_i / n$$

$$Q_z = \sum_{i=1}^n z_i / n$$

Clearly it is advantageous to select the point Q as the origin of the body coordinate system.

6.6 Formulation in Terms of Euler Parameters

The primary disadvantage with expressing finite rotations in terms of the Rodrigues parameters is that the resulting rotation matrix (equation 6.18) is singular when θ

is equal to π . For this reason, the following alternative parameters are extensively used in the general computer implementation of dynamic systems [42].

$$e_0 = \cos \frac{\theta}{2}, \quad e_1 = n_1 \sin \frac{\theta}{2}, \quad e_2 = n_2 \sin \frac{\theta}{2}, \quad e_3 = n_3 \sin \frac{\theta}{2} \quad (6.31)$$

In accordance with Euler's theorem, n_1, n_2, n_3 represent the components of a unit vector along the axis of rotation, and θ the angle of rotation. These four quantities are customarily referred to as the Euler parameters. The components of the Rodrigues vector can be regarded as normalized Euler parameters, i.e.:

$$\rho_1 = \frac{e_1}{e_0}, \quad \rho_2 = \frac{e_2}{e_0}, \quad \rho_3 = \frac{e_3}{e_0} \quad (6.32)$$

In one defines the following unit quaternion in terms of the Euler parameters:

$$q = e_0 + e_1 \vec{i} + e_2 \vec{j} + e_3 \vec{k} \quad (6.33)$$

then the vectors \vec{r} and \vec{r}' which define the position of a point before and after rotation are related by the quaternion representation of the finite rotation formula (equation 6.17):

$$\vec{r}' = q \vec{r} q^{-1}$$

Consequently, the Euler parameters can be obtained in much the same way as the Rodrigues parameters, that is, by solving the set of normal equations which result from the matrix multiplication $[A]^T[A]$ in equation 6.25.

The Euler parameters are not independent and must satisfy the relation:

$$e_0^2 + e_1^2 + e_2^2 + e_3^2 = 1 \quad (6.35)$$

If the magnitude of the rotation is small, then the parameter d (i.e. e_0) can be arbitrarily set to 1 and the remaining (Rodrigues) parameters solved in accordance with equation 6.29.

As the angle of rotation about the unit vector \vec{n} approaches π , parameter d approaches 0. In this case, the parameter c can be arbitrarily set to 1 and the remaining parameters solved as follows:

$$\begin{aligned} c &= 1 \\ d &= -s'_{34}/s'_{44} \\ b &= - (s'_{24}d + s'_{23}c)/s'_{22} \\ a &= - (s'_{14}d + s'_{13}c + s'_{12}b)/s'_{11} \end{aligned} \quad (6.36)$$

The elements of the transformation matrix $[T]$ can then be computed according to equation 6.16 and the Euler angles recovered through the application of equation 2.19.

6.7 Numerical Considerations

The least-squares solution of an estimation problem by means of "normal equations" can lead to inadmissibly large roundoff error. In general, the accuracy of the computed estimate is indicated by the condition number of the matrix to be solved. The condition number of the symmetric matrix of order four which results from the matrix multiplication $[A]^T[A]$ in section 6.4.2 is approximately the square of the condition number of the original matrix, $[A]$. This ill-conditioning can lead to inadmissibly large roundoff error. Consequently, although it is common, the use of normal equations is often not the most efficient or accurate method of solving least squares problems [53] [54].

Several more robust methods appear in the literature. One such method is based on Householder reflections. Instead of multiplying the original rectangular matrix by its transpose, this method renders the matrix upper-triangular by a set of orthogonal transformations [55]. From the point of view of computational accuracy, such methods are preferable for computing the least squares estimate of overdetermined systems of linear equations.

CHAPTER 7

SINGLE CAMERA RESECTION

7.1 Introduction

The main disadvantage of sensing range by triangulation is that the target l.e.d. must be within the field of view of two sensors in order to provide any useful information. This constraint effectively reduces the operating envelope of the system. The common field of view can be increased by reducing the disparity between the two images (i.e. by bringing the two viewpoints closer together) but not without also reducing the accuracy of the range determination. For these reasons, a stereoscopic configuration is impractical in robotic applications where the sensors are "outwardly looking" from the robot's end-effector.

7.2 Formulation of Single-Camera Algorithm

If only one "outwardly looking" sensor is employed, then additional "depth cues" are required to determine the distance between the l.e.d. and the focal centre of the lens. In a structured environment, these cues are provided by geometric constraints. For example, if a number of l.e.d.s are fixed to a rigid body then, by definition, the

distance between any two l.e.d.s remains constant independent of time or configuration. This rigidity constraint can be used to determine the three-dimensional position of each l.e.d. from a single perspective view. In the discipline of photogrammetry, this process is referred to as a single camera resection [44].

For the purposes of this analysis, six target l.e.d.s are arranged in a circular pattern 6 inches (0.1524 m) in diameter. A seventh l.e.d. is placed at the centre of the circle and is arbitrarily chosen as the origin of the movable or body-fixed coordinate system. The coordinates of the target l.e.d.s with respect to this coordinate system are denoted by:

$$[P_{x0I}, P_{y0I}, P_{z0I}] \quad I=1,2,\dots,6.$$

These coordinates are independent of the orientation of the rigid body and are known a priori.

Matrix $[A]$ is an orthogonal rotation matrix which relates the body-fixed coordinate system to the sensor (i.e. global) coordinate system.

$$\begin{bmatrix} P_{x0I} \\ P_{y0I} \\ P_{z0I} \end{bmatrix}^T \begin{bmatrix} a_{11} & a_{12} & a_{13} \\ a_{21} & a_{22} & a_{23} \\ a_{31} & a_{32} & a_{33} \end{bmatrix} = \begin{bmatrix} P_{xI} \\ P_{yI} \\ P_{zI} \end{bmatrix}^T \quad (7.4)$$

The R.H.S. of equation 7.4 represents the vector from the origin of the movable coordinate system (i.e. l.e.d. 7) to each l.e.d. measured with respect to the sensor coordinate system. The rotation matrix $[A]$ is a function of three generalized coordinates, namely the Euler angles α , β , γ .

$$\begin{aligned}
a_{11} &= \cos(\gamma)\cos(\alpha) \\
a_{12} &= \cos(\gamma)\sin(\alpha) \\
a_{13} &= -\sin(\gamma) \\
\\
a_{21} &= \sin(\beta)\sin(\gamma)\cos(\alpha) - \cos(\beta)\sin(\alpha) \\
a_{22} &= \sin(\beta)\sin(\gamma)\sin(\alpha) + \cos(\beta)\cos(\alpha) \\
a_{23} &= \sin(\beta)\cos(\gamma) \\
\\
a_{31} &= \cos(\beta)\sin(\gamma)\cos(\alpha) + \sin(\beta)\sin(\alpha) \\
a_{32} &= \cos(\beta)\sin(\gamma)\sin(\alpha) - \sin(\beta)\cos(\alpha) \\
a_{33} &= \cos(\beta)\cos(\gamma)
\end{aligned} \tag{7.5}$$

The vector from the origin of the sensor coordinate system, S, to the origin of the body-fixed coordinate system, Q, is denoted by:

$$\vec{R}_{SQ} = [R_{x7}, R_{y7}, R_{z7}]$$

and the location vectors of the six target l.e.d.s with respect to the sensor coordinate system are given by:

$$\vec{R}_I = \vec{P}_{OI}[A] + \vec{R}_{SQ} \quad I=1,2,\dots,6. \quad (7.6)$$

$$\begin{bmatrix} R_{XI} \\ R_{YI} \\ R_{ZI} \end{bmatrix}^T = \begin{bmatrix} P_{XOI} \\ P_{YOI} \\ P_{ZOI} \end{bmatrix}^T \begin{bmatrix} a_{11} & a_{12} & a_{13} \\ a_{21} & a_{22} & a_{23} \\ a_{31} & a_{32} & a_{33} \end{bmatrix} + \begin{bmatrix} R_{X7} \\ R_{Y7} \\ R_{Z7} \end{bmatrix}^T$$

The direction of the vector \vec{R}_{SQ} can be determined from the image coordinates of l.e.d. 7 (x_{D7} and y_{D7}), however, the magnitude, $|\vec{R}_{SQ}|$, is unknown.

The direction cosines of the vector between each l.e.d. and the origin of the sensor coordinate system are given by:

$$\begin{aligned} \cos(A_I) &= R_{XI} / |\vec{R}_I| \\ \cos(B_I) &= R_{YI} / |\vec{R}_I| \\ \cos(C_I) &= R_{ZI} / |\vec{R}_I| \end{aligned} \quad (7.7)$$

$$|\vec{R}_I| = \sqrt{R_{XI}^2 + R_{YI}^2 + R_{ZI}^2}$$

The direction cosines, which are nonlinear functions of the four unknown parameters, can be computed from the image coordinates of the six l.e.d.s (equation 5.2). The four nonlinear parameters can be determined by applying Newton's method to the following system of nonlinear equation.

$$\begin{aligned} F_{AI} &= f(\alpha, \beta, \gamma, |\vec{R}_{SQ}|) = R_{XI} / |\vec{R}_I| - \cos(A_I) = 0 \\ F_{BI} &= f(\alpha, \beta, \gamma, |\vec{R}_{SQ}|) = R_{YI} / |\vec{R}_I| - \cos(B_I) = 0 \\ F_{CI} &= f(\alpha, \beta, \gamma, |\vec{R}_{SQ}|) = R_{ZI} / |\vec{R}_I| - \cos(C_I) = 0 \end{aligned} \quad (7.8)$$

The Jacobian matrix, J , for this system of equations is given by:

$$\left[\begin{array}{cccc} \frac{\partial F_{A1}}{\partial \alpha} & \frac{\partial F_{A1}}{\partial \beta} & \frac{\partial F_{A1}}{\partial \gamma} & \frac{\partial F_{A1}}{\partial |\vec{R}_{SQ}|} \\ \frac{\partial F_{B1}}{\partial \alpha} & \frac{\partial F_{B1}}{\partial \beta} & \frac{\partial F_{B1}}{\partial \gamma} & \frac{\partial F_{B1}}{\partial |\vec{R}_{SQ}|} \\ \frac{\partial F_{C1}}{\partial \alpha} & \frac{\partial F_{C1}}{\partial \beta} & \frac{\partial F_{C1}}{\partial \gamma} & \frac{\partial F_{C1}}{\partial |\vec{R}_{SQ}|} \\ \vdots & & & \end{array} \right] \left. \begin{array}{l} \\ \\ \\ \end{array} \right\} \begin{array}{l} \text{l.e.d. 1} \\ \\ \text{l.e.d. 2-6} \end{array} \quad (7.9)$$

The method functions in an iterative manner, that is, a vector Y is found which satisfies:

$$J(X^{(K-1)}) Y = - F(X^{(K-1)}) \quad (7.10)$$

where $X^{(K-1)}$ is the last approximation to the unknown parameters. The new approximation is then computed as follows:

$$X^{(K)} = X^{(K-1)} + Y \quad (7.11)$$

The procedure continues until the vector on the right-hand-side of equation 7.10 is 0. However, since 6 l.e.d.s represent an overdetermined set of equations, and since the coordinate data is subject to measurement error, a single set of parameters can never satisfy all of the available equations exactly. It is therefore advantageous to find the least-squares estimation of the nonlinear

parameters which minimize the right-hand side of equation 7.10. This is accomplished by multiplying both sides of equation 7.10 by the transpose of the Jacobian as follows:

$$\begin{aligned} [J]^T [J] [Y] &= -[J]^T [F] \\ [M] [Y] &= [\delta] \end{aligned} \tag{7.12}$$

The set of normal equations is defined by the 4 by 4 matrix $[M]$ and the 4 by 1 vector $[\delta]$. The solution process consists of iteratively solving the set of normal equations for the vector $[Y]$ and updating the estimation of the nonlinear parameters according to equation 7.11 [56].

7.3 Convergence of Algorithm

Based on an arbitrary starting point, the rotational parameters can generally be determined within 5 iterations. If the velocity (both translational and rotational) of the rigid body is small, and if it is being tracked continuously, then the initial starting point is already accurate and significantly fewer iterations are required. Table 1 shows the values of the rotational parameters after each iteration for a typical trial run. The exact solution is $\alpha = 30$, $\beta = 60$, and $\gamma = 70$ degrees.

TABLE 7.1 : Convergence of 'Single-Camera' Alogorithm

ITER.#	α DEG.	β DEG.	γ DEG.
START	28.64789	28.64789	28.64789
1	27.51714	38.64191	49.02898
2	28.39637	51.77376	65.01199
3	29.85752	59.51184	69.98208
4	30.00208	60.00474	70.00044
5	30.00000	60.00000	70.00000

CHAPTER 8

PERFORMANCE EVALUATION

8.1 Introduction

In Chapter 5, the three-dimensional cartesian coordinates of a point (i.e. LED) in space were calculated from two perspective views of that point. An algorithm to compute the unique six degree-of-freedom position and orientation of a rigid body in space given the cartesian coordinates of a minimum of three non-colinear body-fixed points was formulated in Chapter 6. An iterative technique based on a single perspective view was derived in Chapter 7. As mentioned previously, the single-camera algorithm is essential for robotic applications where the sensor is "outwardly looking" from the robot's end-effector. However, in the case of the Fiber Optic Helmet Mounted Display, the two-camera or stereoscopic approach is more appropriate.

Fundamentally there is twice as much information in two perspective views as there is in one. Although much of this information is redundant, measurement error can still be reduced by employing regression analysis to find the orientative parameters which best describe the kinematic state of any number of body-fixed points. By applying Schut's method, the orientative parameters can be determined

uniquely by solving a set of exact linear equations. In the case of the single-camera algorithm, the four unknown parameters are determined through the iterative solution of a system of nonlinear equations. For these reasons, the stereoscopic approach is the method of choice for the Optical Helmet Position Measurement System.

This chapter deals with the influence of various parameters on system performance assuming a stereoscopic approach. The primary performance index is the accuracy of the measurement as defined by the standard deviation, σ_e . The standard deviation is equal to the positive square root of the variance, σ_e^2 . If X_1, X_2, \dots, X_n represent a random sample of size n , then the sample variance, σ_e^2 , is defined by the statistic:

$$\sigma_e^2 = \frac{n \sum_{i=1}^n X_i^2 - \left(\sum_{i=1}^n X_i \right)^2}{n (n - 1)} \quad (8.1)$$

The significance of this statistic in terms of a measurement system is that the measured quantity will be within $\pm\sigma_e$ of the true value with a 68% confidence interval [57].

A statistical simulation program was developed to quantitatively determine the accuracy of the Optical Position Measurement System as a function of several parameters. These parameters include the number of points

(i.e. LEDs) included in the regression model and the number of "noise-free" bits provided by the A/D converter. The same program can be used to investigate the influence of other parameters such as the size and shape of the LED pattern and the placement of the sensors. Such parameters are generally invariant, however, since the application normally dictates the geometry of the system. The placement of the sensors, for example, is generally fixed by the installation and by the required operating envelope of the system.

8.2 Program Description

The LED pattern used in this study consists of six coplanar LEDs equally spaced on a 6" (152.4 mm) circle. The X axis of the body coordinate system passes through LED 2 as shown in Figure 8.1. When in the nominal rigid body position, the body coordinate system is coincident with fixed reference frame (i.e. $\alpha=\beta=\gamma=0$) and the origin of the body coordinate system is coincident with the intersection of the aiming vectors of the two lenses (Figure 5.2).

Figure 8.2 is a two-dimensional perspective projection of the LED pattern as viewed from Sensor 1. The geometric configuration is as shown in Figure 5.2 with the LED pattern in the nominal rigid body position. The location of the image of each LED on the sensitive surface of the detector

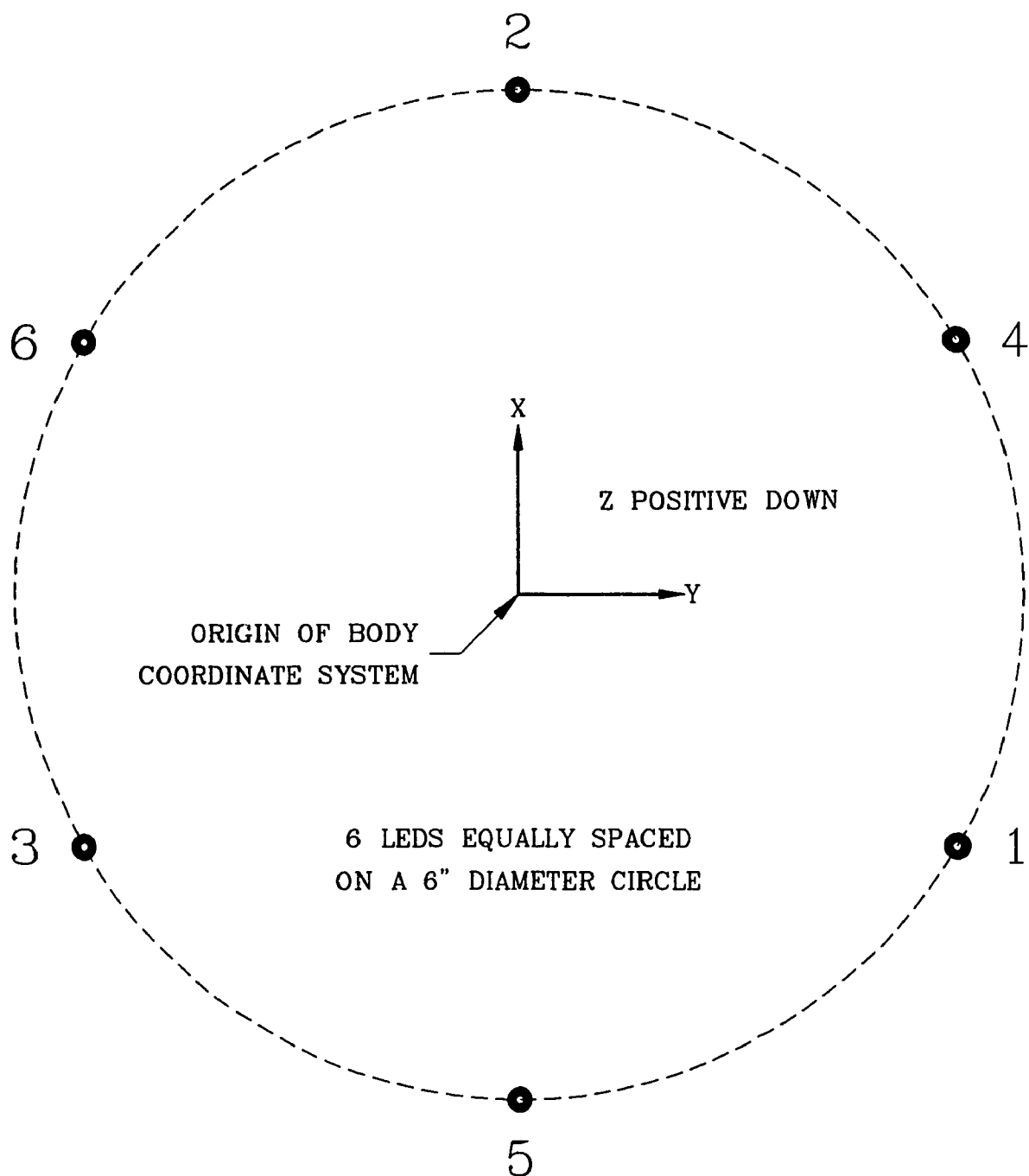


Figure 8.1: Schematic representation of the LED pattern used in this study.

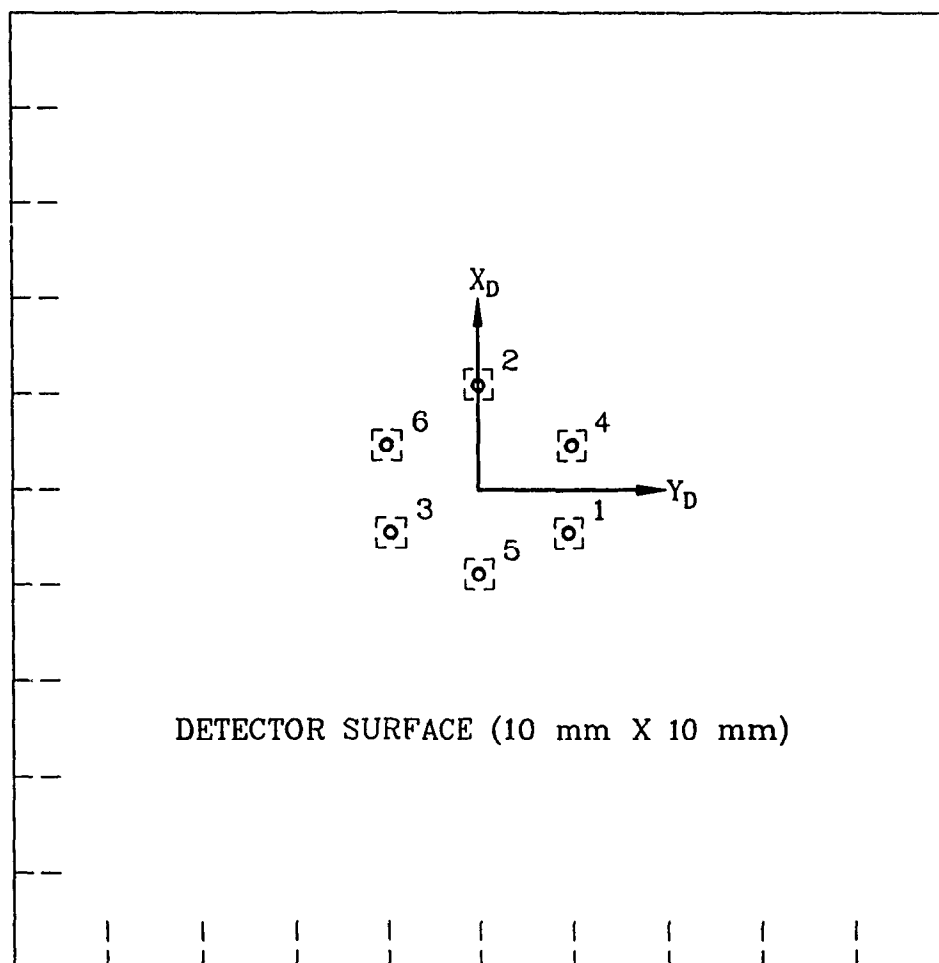


Figure 8.2: Two-dimensional perspective projection of the LED pattern as viewed from Sensor 1.

is defined by two coordinates, x_D and y_D , which are proportional to the output voltage signals provided by the sensor. Uncertainty is introduced into the measurement process when the output voltage signals, V_x and V_y , are digitized. The degree of uncertainty is dependent on the number of "noise-free" bits provided by the A/D converter.

The dashed square surrounding the image of each LED in Figure 8.2 represents the area of uncertainty which results when the output voltage signals are digitized with a resolution of 5 bits. The LED image can travel anywhere within that area of uncertainty without producing a noticeable change in the output of the A/D converter.

The statistical simulation program operates by computing the image coordinates of the six target LEDs with respect to the two sensors for a given position and orientation of the rigid body. The program then computes the area of uncertainty surrounding each point on the sensitive surface of the detector. If N represents the number of "noise-free" bits provided by the A/D converter, then the range of uncertainty, \mathcal{R} , in both the X_D and Y_D directions is defined by:

$$\mathcal{R} = \frac{10}{2^N} \text{ mm} \quad (8.2)$$

The simulation program randomly relocates the image of each LED within a square of \mathcal{R} by \mathcal{R} mm. This is accomplished

by generating random numbers which are uniformly distributed across the interval from 0 to 1. If $\epsilon_1, \epsilon_2, \dots, \epsilon_i$ represents a sequence of such numbers, then the error term, δ_i , added to the image coordinates of each LED is given by:

$$\delta_i = \mathcal{R} (\epsilon_i - 0.5) \quad (8.3)$$

A FORTRAN routine which generates random numbers uniformly distributed across the interval from 0 to 1 is given below.

```

      SUBROUTINE RANDOM(SEED, RANDX)
      *
      *   This subroutine generates random values between 0.0
      *   and 1.0 using an integer seed
      *
      INTEGER SEED
      REAL RANDX
      SEED=2045*SEED+1
      SEED=SEED-(SEED/1048576)*1048576
      RANDX=REAL(SEED+1)/1048577.0
      RETURN

```

This routine operates by calculating integers which are too large for the processor to store. The portion of the number that can be stored forms a random sequence. This number generator is typically used to model the noise that might occur in a piece of instrumentation [58].

The image coordinates of the LEDs as viewed from both sensors are randomly relocated within the area of uncertainty in accordance with the procedure outlined above. Using the relocated image coordinates as input, the simulation program then computes the position and

orientation of the rigid body by applying the stereoscopic techniques developed in Chapters 5 and 6. This is done repetitively in order to arrive at an accurate estimate of the standard deviation for each of the output quantities.

Figure 8.3 shows the discrete probability distributions generated by the simulation program for Yaw assuming 3 and 6 LEDs in the regression model and a resolution of 9 bits. The LED pattern is assumed to be in the nominal rigid body position. The Y axis (i.e. the frequency of occurrence) is scaled so that the area under the curve bounded by the X axis is equal to 1. The continuous curve in Figure 8.3 is the theoretical normal distribution based on the mean and standard deviation provided by the simulation program.

The normal distribution closely approximates the discrete frequency distribution generated by the simulation program. The "goodness of fit" between the two distributions can be quantitatively evaluated by means of the Chi-Square Test. The deviation between the simulated frequency of occurrence, s_i , and the theoretical frequency of occurrence, t_i , can be represented by the random variable κ^2 .

$$\kappa^2 = \sum_{i=1}^k \frac{(s_i - t_i)^2}{t_i} \quad (8.4)$$

where k is the number of intervals along the X axis with at least 5 sample values.

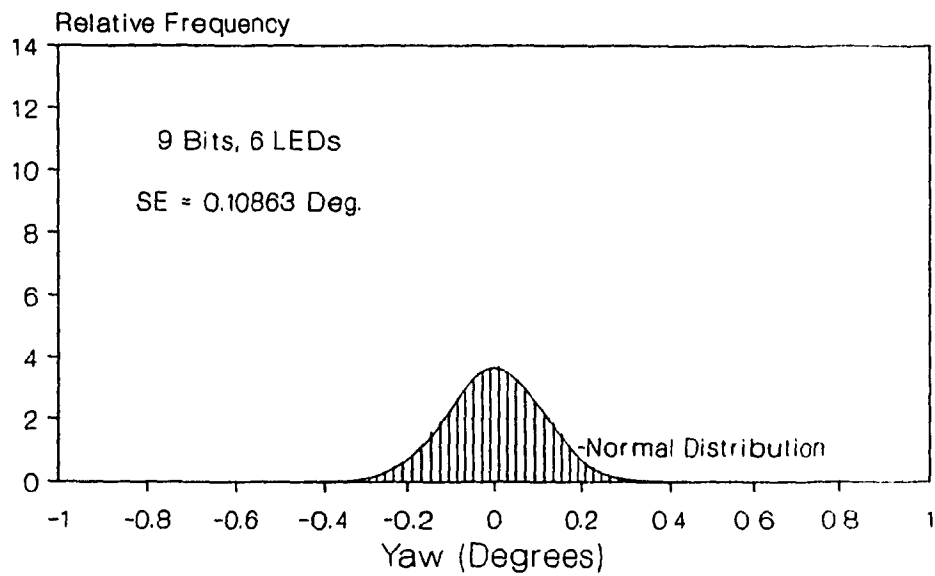
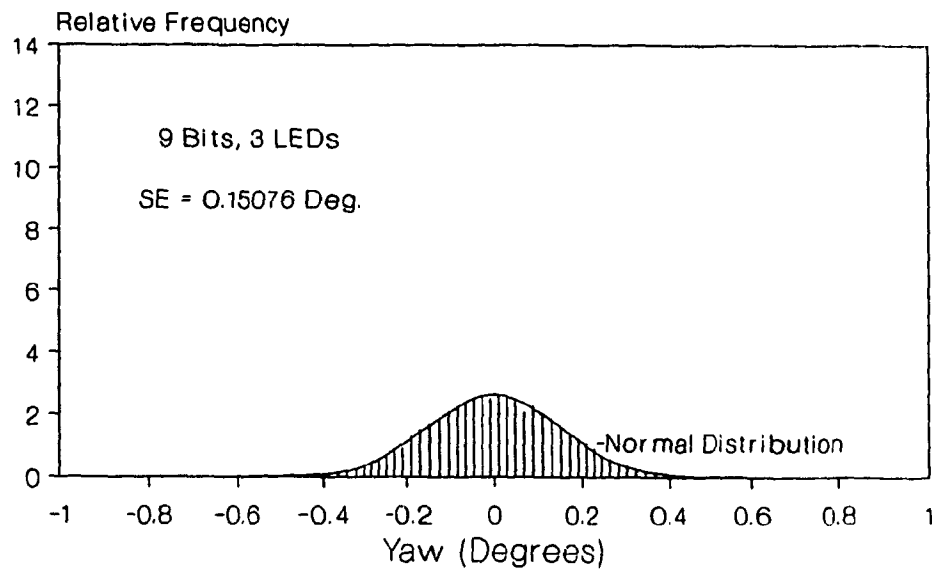


Figure 8.3: Probability distributions generated by the simulation program for Yaw assuming 3 and 6 LEDs and a resolution of 9 bits.

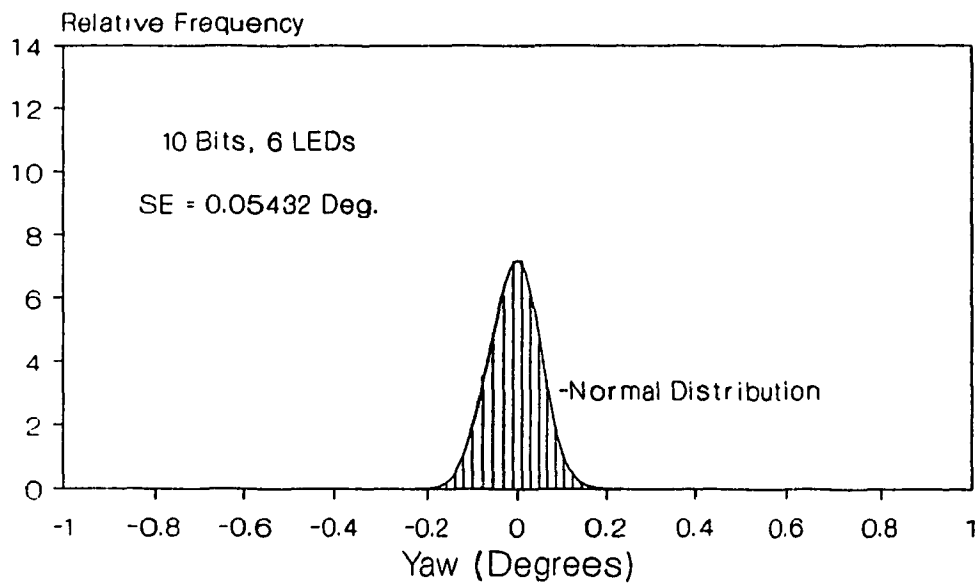
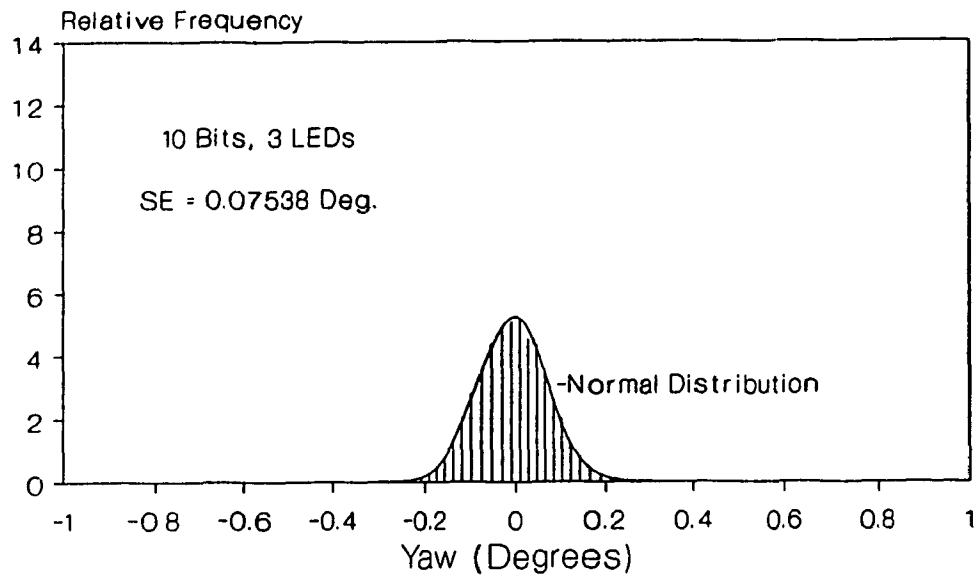


Figure 8.4: Probability distributions generated by the simulation program for Yaw assuming 3 and 6 LEDs and a resolution of 10 bits.

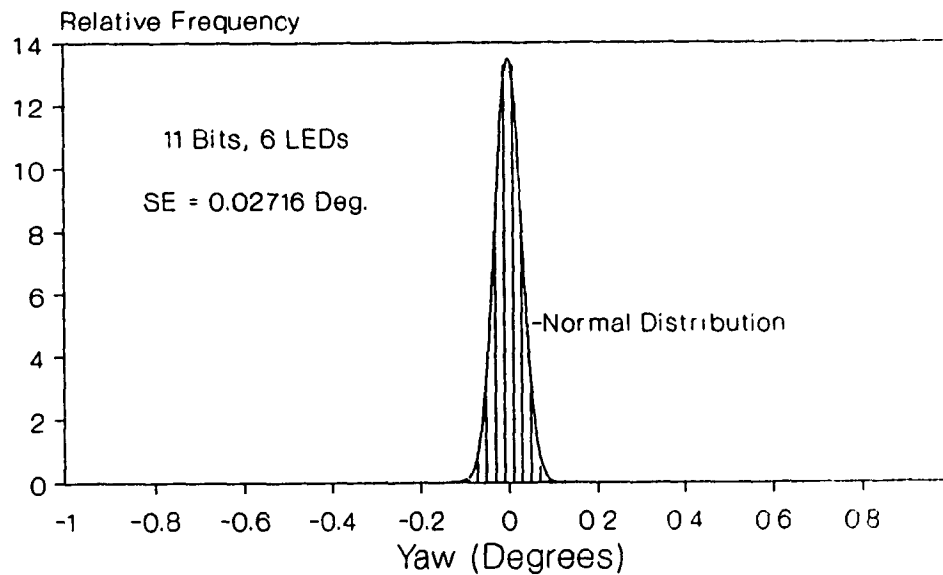
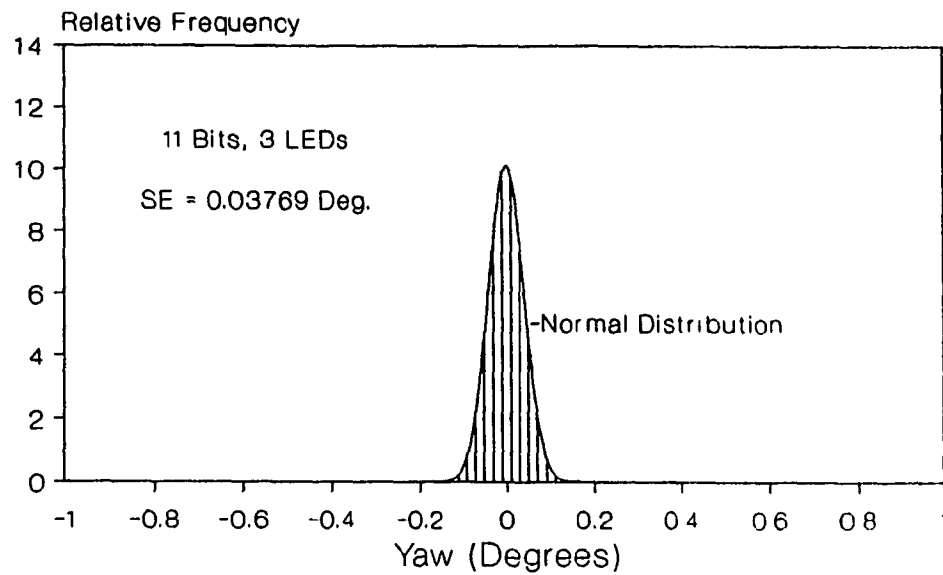


Figure 8.5: Probability distributions generated by the simulation program for Yaw assuming 3 and 6 LEDs and a resolution of 11 bits.

The number of degrees of freedom for the purposes of the Chi-Square test is equal to $(k-3)$ since three parameters, namely, the total frequency, mean, and standard deviation of the simulation data are required to calculate the theoretical normal frequency distribution [24] [59].

The computed value of κ^2 for 3 LEDs and a resolution of 9 bits is 42.131. The critical value of the Chi-Square Distribution assuming a significance level of 5% and 40 degrees of freedom is 55.8. Therefore, the normal distribution provides a good fit to the discrete frequency distribution generated by the simulation program. The same conclusion can be drawn for the frequency distributions of Figure 8.4 and 8.5 as well as for those of Pitch and Roll.

The equation for the normal distribution curve is a function of two parameters, μ and σ , the mean and standard deviation respectively. When the LED pattern is in the nominal rigid body position, the mean of the random variable (i.e. Yaw, Roll, or Pitch) is zero and the frequency distribution is uniquely defined by the standard deviation. Table 8.1 summarizes the results obtained from the statistical simulation program. The standard deviation in Yaw, Roll, and Pitch is tabulated as a function of two parameters; the number of LEDs in the regression model and the number of "noise-free" bits provided from the A/D converter.

Table 8.1: Summary of Results Obtained from the Statistical Simulation Program.

STANDARD DEVIATION IN YAW

LEDS →	1 to 3	1 to 4	1 to 5	1 to 6
System*	0.07274	0.06845	0.06517	0.05935
9 Bits	0.15076	0.13492	0.12205	0.10863
10 Bits	0.07538	0.06746	0.06103	0.05432
11 Bits	0.03769	0.03373	0.03051	0.02716

STANDARD DEVIATION IN ROLL

LEDS →	1 to 3	1 to 4	1 to 5	1 to 6
System*	-	-	-	0.10341
9 Bits	0.28651	0.24777	0.24791	0.20043
10 Bits	0.14325	0.12389	0.12395	0.10022
11 Bits	0.07162	0.06194	0.06198	0.05011

STANDARD DEVIATION IN PITCH

LEDS →	1 to 3	1 to 4	1 to 5	1 to 6
System*	-	-	-	0.10497
9 Bits	0.28497	0.27232	0.21865	0.20180
10 Bits	0.14249	0.13617	0.10932	0.10090
11 Bits	0.07125	0.06808	0.05466	0.05045

* "System" denotes values obtained experimentally.

8.3 Analysis of Results

Several important conclusions can be drawn from the data of Table 8.1. Assuming five significant digits, the standard deviation in Yaw, Roll, and Pitch is reduced by exactly half for each additional "noise-free" bit provided by the A/D converter. Since each additional bit reduces the bound of the error added to the image coordinates of each LED by half, this conclusion may appear obvious. However, the orientation of the rigid body is not a linear function of the image coordinates of the target LEDs. A number of nonlinear and transcendental functions must be evaluated in order to determine the Euler angles. In addition, the number of "noise-free" bits provided by the A/D converter affects the range of uncertainty surrounding each LED image. The error term introduced into the measurement process is *uniformly distributed* across this range. In contrast, the resulting Euler angles are *normally distributed*. It is the standard deviation of this normal distribution which decreases by half for each additional "noise-free" bit provided by the A/D converter. Therefore the conclusion drawn is not necessarily an obvious one.

For small perturbations about an operating point, a linear relationship between the image coordinates and the Euler angles can be formulated. Such a relationship yields

accurate results when the number of "noise-free" bits is high resulting in a small range of uncertainty. The statistical simulation program suggests that this is the case for 9 or more "noise-free" bits.

The relationship between the standard deviation of the random variable and the number of LEDs in the regression model is not straightforward. As expected, the reduction in standard deviation due to the addition of an LED is dependent on the distance between that LED and the axis of rotation for the specific Euler angle under consideration. In simple terms, the larger the LED pattern, the more accurate the results.

In the case of Yaw, the six LEDs are equidistant from the Yaw axis of rotation. Consequently, each LED reduces the standard deviation by approximately the same amount. As the number of LEDs is increased further, the relative improvement in standard deviation decreases. For a finite number of LEDs in the regression model, the standard deviation will always be greater than zero. Therefore the relative improvement in standard deviation associated with each LED must decrease.

In the case of Roll, the addition of LED 5 results in no improvement in standard deviation since LED 5 lies on the axis of rotation (Figure 8.1). Similarly, the relative improvement in Pitch due to LED 5 is significantly greater

than for LED 4 or LED 6 since LED 5 is the furthest from the axis of rotation.

In general, the addition of LEDs 4, 5, and 6 in the regression model reduces the standard deviation in Yaw, Roll, and Pitch by approximately 30%. By way of comparison, an additional "noise-free" bit reduces the standard deviation by 50%.

8.4 Experimental Results

The standard deviations in Yaw, Roll, and Pitch were determined experimentally through direct calibration of the Optical Position Measurement System. A dividing head was used as a "calibration standard." The orientation of the LED pattern was varied about the nominal rigid body position as the measured yaw, roll, and pitch were recorded. A summary of the calibration results appears in Table 8.1 under the heading "System." For the purpose of validating the statistical simulation program, the standard deviation in Yaw as a function of the number of active LEDs was also experimentally determined. It should also be noted that of the 12 bits provided by the A/D converter, only 10 were observed to be "noise-free."

The statistical simulation program accurately predicts the standard deviation in Yaw, Roll and Pitch assuming 10

"noise-free" bits and 6 LEDs. In the case of Yaw, it also predicts the improvement in standard deviation as the number of active LEDs in the regression model is increased.

8.5 Summary

In Chapter 3, the theoretical signal to noise ratio based on the shot noise for the Optical Position Measurement System was found to be 11030 or 81 db. This value imposes an absolute limit on the accuracy that can be obtained without increasing the radiant flux incident on the sensitive surface of the detector. A signal to noise ratio of 81 db corresponds to 13.5 significant bits on an A/D converter. As stated previously, it was experimentally determined that of the 12 bits provided by the A/D converter, only 10 are significant (i.e. "noise-free"). An additional "noise-free" bit would reduce the standard deviation in Yaw, Roll, and Pitch by 50% without increasing the computational effort. Including more LEDs in the regression model would also decrease the standard deviation, but at the cost of a significant increase in execution time.

Based on these findings, an improvement in accuracy can best be realized by increasing the number of "noise-free" bits provided by the A/D converter. Methods of accomplishing this are discussed in detail in the next chapter.

CHAPTER 9

CONCLUSIONS AND RECOMMENDATIONS FOR FUTURE WORK

9.1 General

The main objective of this thesis was to develop techniques for determining, in real-time and with a high degree of accuracy, the absolute position and orientation of a rigid body in space. The development of these techniques was originally motivated by the recent trend towards high resolution area-of-interest visual systems for high performance tactical aircraft simulators. Such visual system need only display the "instantaneous" image currently within the pilot's field of view. This approach significantly reduces the amount of imagery which must be generated at any instant. However, in order for the computer generated image to appear stationary as the pilot moves his head, the position and orientation of the pilot's helmet must be measured in six degrees-of-freedom, with a resolution comparable to the acuity of the human eye, and at a rate of 60 Hz.

The Optical Helmet Tracking System, which was a direct result of the work described in this thesis, has been successfully applied to the prototype Fiber Optic Helmet Mounted Display (FOHMD) at the Human Resources Laboratory of

Williams Air Force Base in Arizona [60] [61]. Currently, CAE Electronics Ltd. is incorporating the FOHMD and Helmet Tracking System into several high-performance tactical aircraft simulators including the German Multi Roll Combat Aircraft (MRCA) Tornado. It has also been successfully used in a number of experimental facilities including the U.S. Army's Simulator Complexity Test Bed and NASA's Crewstation Research and Development Facility [62] [63].

Although the performance of the Optical Position Measurement System falls short of the required 2 to 3 arc minutes of accuracy, it is nevertheless the most accurate system available [64]. Techniques for improving the performance of the system are presented in section 9.3.1.

The Mechanical Position Measurement System described in Chapter 2 is currently used by CAE Electronics Ltd. for in-house development and demonstration purposes. It provides an accurate, low cost alternative to the Optical Position Measurement System in applications where a noncontact approach is not required.

9.2 Summary

Fundamentally there are a number of difficulties inherent in acquiring accurate spatial information in real-time from conventional image sensors (CCDs, vidicons,

etc). In general, real-time measurement systems based on these devices are either not accurate enough because of the limited resolution of the sensor, or not fast enough because of the volume of data that must be processed.

A planar PIN photodiode which meets the conflicting requirements of high accuracy and real-time response is analyzed and evaluated in Chapter 3. The evaluation criteria include linearity, resolution, response, and sensitivity to spurious inputs. Of these, the primary performance limiting criterion is resolution. The resolution of the device is ultimately limited by the shot noise which is present due to the discrete nature of the photocurrent. The theoretical signal to noise ratio based on the shot noise can be derived from the intensity signal, Σ . This signal to noise ratio imposes an absolute limit on the resolution that can be obtained without increasing either the integration time or the radiant flux incident on the sensitive surface of the detector. Since a long integration time is impractical in a real-time application, the logical alternative is to maximize the radiant power output delivered by the target light source.

Chapter 4 deals primarily with the selection of the target light source and the design of the Intensity Control Circuit. The purpose of the Intensity Control Circuit is to maximize the radiant power delivered by the target light

source while maintaining the radiant flux incident on the sensitive surface of the detector constant irrespective of the position or orientation of the rigid body. The second objective was met through a closed loop control system which regulates the radiant power emitted from the target light source based on a feedback signal from the detector. A nonlinear control strategy which effectively reduces the settling time of the system without introducing steady-state error was implemented.

Chapters 5, 6, and 7 are devoted to the problem of determining the absolute position and orientation of a rigid body in space given the image coordinates of three or more body-fixed points. Two methods of solution are presented.

In the case of the stereoscopic approach, the body-fixed points are viewed from two different locations and a triangulation scheme is used to compute the three dimensional cartesian coordinates of each point. Once these coordinates are known, the rotational parameters are found by applying the method of least squares to an overdetermined system of exact, linear equations.

In Chapter 7, the "rigidity constraint" is used to determine the position and orientation of the rigid body from a single perspective view. In this case the orientative parameters are determined through the iterative solution of a system of nonlinear equations. While the single-camera

algorithm is essential for robotic applications where the sensor is outwardly looking from the robot's end-effector, the two-camera or stereoscopic approach is more appropriate for the Fiber Optic Helmet Mounted Display.

In chapter 8 a statistical simulation program was developed to quantitatively investigate the influence of various parameters on system performance assuming a stereoscopic approach. It was found that the standard deviation of the random variable was reduced by exactly half for each additional "noise-free" bit provided by the A/D converter. This is attributable to the fact that for small perturbations about an operating point, a linear relationship between the image coordinates and the Euler angles can be formulated.

The relationship between the standard deviation of the Euler angles and the number of points in the regression model is not as straightforward. In general, as the number of points in the regression model is increased, the configuration space becomes smaller, that is, the range of general displacements which satisfy all of the available equations is reduced.

Based on both the experimental and simulation results it can be concluded that an improvement in accuracy can best be realized by increasing the number of "noise-free" bits provided by the A/D converter and not by increasing the

number of points in the regression model.

9.3 Recommendations for Future Work

The recommendations for future work fall into two general areas.

- i) enhancing the performance of the measurement system by implementing data acquisition and signal processing functions within the sensor itself
- ii) applying the measurement techniques originally developed for the area-of-interest visual system to other disciplines which require the accurate, real-time determination of position and orientation (e.g. robotics)

9.3.1 Enhancements

In Chapter 3, the theoretical signal to noise ratio based on the shot noise for the Optical Position Measurement System was found to be 81 db which corresponds to a resolution of 13.5 bits. It was experimentally determined that of the 12 bits provided by the A/D converter, only 10 are significant. The sensor falls short of ideal shot-noise

limited performance primarily because of the influence of other noise sources. For example, there is approximately 0.6 mV (rms) of noise superimposed on the output of the Integrated Circuit Multiplier (Analog Devices AD532) used in the Analog Position Processing Circuit. This noise is amplified by a factor of 10 in the subsequent stage of the circuit. Therefore, this noise source alone contributes 6 mV of noise to the output voltage signals, V_x and V_y . A noise level of 6 mV on a full-scale range of ± 5 volts, represents a resolution of under 11 bits.

An alternative configuration which minimizes the number of secondary noise sources is shown schematically in Figure 9.1. The current signals from the four electrodes are conditioned by a current-to-voltage converter with a first-order transfer function. The resulting voltage signals are then immediately digitized by an A/D converter. Since analog signals are susceptible to electromagnetic interference when transmitted over a long distance, it is preferable to incorporate the A/D converter directly into the sensor housing.

To provide a full-scale output of 10 volts, the current-to-voltage converter must have a gain of approximately 5×10^6 V/A. This necessitates a feedback resistor of 5 M Ω between the output and non-inverting input of the operational amplifier. Such a large value of feedback

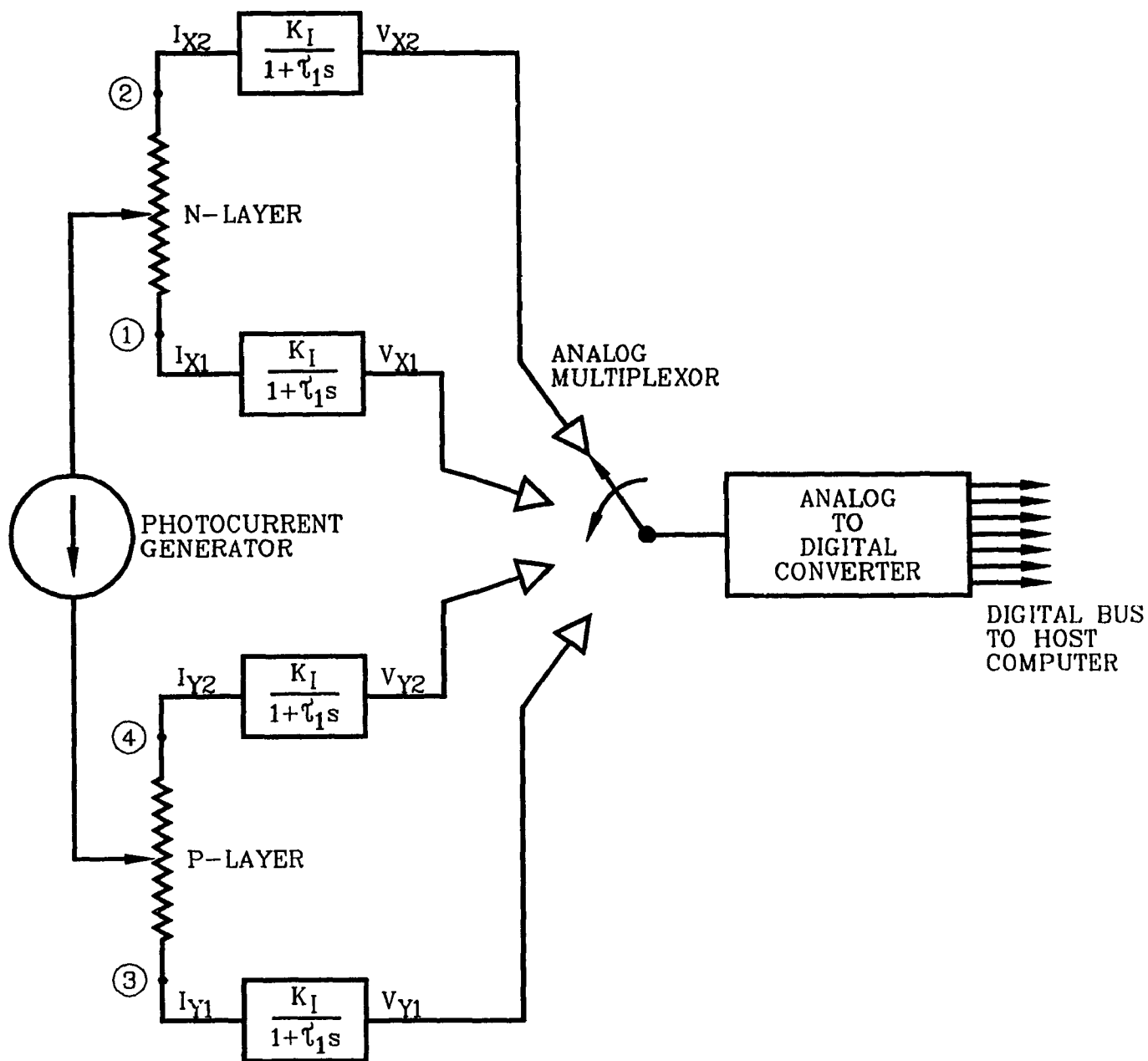


Figure 9.1: Alternative sensor configuration which minimizes the number of secondary noise sources.

resistance is not recommended even on high performance JFET-input operational amplifiers. The required gain could be accommodated in two stages of amplification, however, this would introduce an additional noise source.

A viable solution is to use an electrometer operational amplifier (Analog Devices AD549) in the design of the current-to-voltage converter. Due to the extremely low input current and input offset voltage exhibited by these devices, feedback resistances as high as $10^9 \Omega$ can be used.

The proposed configuration shown in Figure 9.1 offers a number of advantages in addition to reducing the number of secondary noise sources. The two position signals, V_x and V_y , are based on the *normalized* current flowing from the light spot to each pair of opposing electrodes located on the top and bottom surfaces of the photodiode. That is,

$$V_x \propto \frac{V_{x1} - V_{x2}}{V_{x1} + V_{x2}}, \quad V_y \propto \frac{V_{y1} - V_{y2}}{V_{y1} + V_{y2}} \quad (9.1)$$

The existing Analog Position Processing Circuit relies on operational amplifier circuits to perform the additions and subtractions and an Integrated Circuit Multiplier to perform the division. In the proposed configuration, these analog devices have been eliminated and all the data processing is done numerically. This arrangement is inherently more accurate and less susceptible to noise. It also offers the

possibility of minimizing the effects of background illumination.

The two dimensional current flow through the resistive layer on the surface of the photodiode is governed by Laplace's equation. Since Laplace's equation represents a linear, homogeneous, partial differential equation, the superposition principle applies. The current flowing to each electrode when two current sources are applied to the photodiode is equal to the sum of the currents for each source acting independently. Background illumination can effectively be eliminated by sampling the four current signals with the target light source off and then subtracting these readings from the current signals sampled with the light source on.

Proposed enhancements to the Intensity Control Circuit are shown in Figure 9.2. This configuration forces the forward current through the LED to be proportional to the voltage signal, V_{IN} , applied to the non-inverting input of the operational amplifier. A D/A converter is used to generate V_{IN} . Since only one LED is active at any one time, the same D/A can be used to control several LEDs through an analog multiplexer. The host computer is continuously calculating the position of each LED, therefore, it can accurately predict the current required to maintain the intensity at the setpoint value. Basically the required

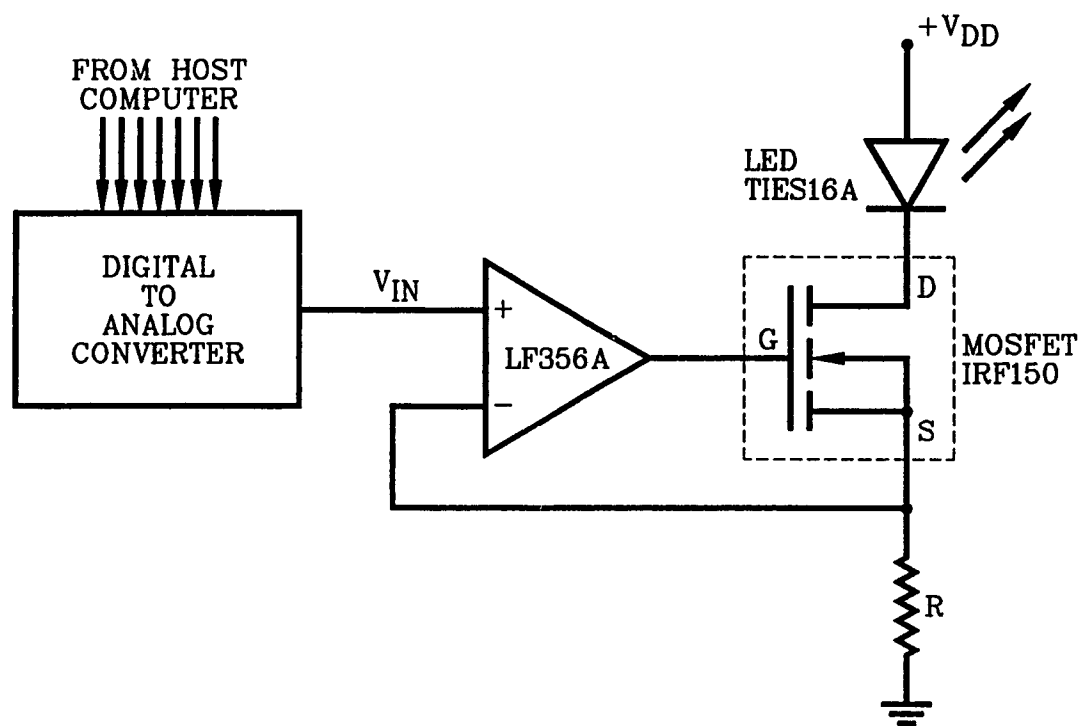


Figure 9.2: Proposed enhancements to the Intensity Control Circuit.

current is inversely proportional to the square of the distance between the LED and the sensor. A new value of V_{IN} would be computed at each iteration to correct for any discrepancies between the feedback and setpoint values.

9.3.2 Applications

As stated in Chapter 1, sensory feedback techniques offer the greatest potential for improving the accuracy of industrial robots. If the position and orientation of the robot's end-effector could be precisely measured and rapidly fed back to the robot control computer, a potentially lighter, more compliant robot could be realized without sacrificing repeatability or positioning accuracy. The measurement techniques described in this thesis can be used to investigate robot control strategies based on real-time sensory feedback.

In a project that has recently been initiated, a single "outwardly looking" sensor is used to measure the position and orientation of the end-effector of a high performance electro-hydraulic servo manipulator. The manipulator, currently under development at Concordia, employs hydraulic actuators with conical hydrostatic bearings to improve control accuracy by minimizing Coulomb friction. The combination of the manipulator and measurement system

provides an ideal vehicle to investigate robot control strategies and parameter identification based on real-time sensory feedback with the goal of improving robot performance. This work is particularly relevant to large, light-weight manipulators where considerations such as link compliance, backlash, friction, etc., are especially significant [65].

An integral part of this study is an investigation into the influence of various parameters on the accuracy of Optical Position Measurement System assuming a single-camera approach.

REFERENCES

- [1] H.W. Stone and A.C. Sanderson, "Arm Signature Identification," The Robotics Institute 1986 Annual Research Review, Carnegie Mellon University, Pittsburgh, Pennsylvania, 1986, pp. 21-31.

- [2] M. Ishii, S. Sakane, M. Kakikura, and Y. Mikami, "A 3-D Sensor System for Teaching Robot Paths and Environments," The International Journal of Robotics Research, Vol. 6, No. 2, Summer 1987, pp. 45-59

- [3] A.M. Spooner, "The Trend Towards Area of Interest in Visual Simulation Technology," Proceedings of the Fourth Interservice/Industry Training Equipment Conference, November 1982, pp. 205-214.

- [4] L.A. Haworth and N.M. Bucher, "Helmet-Mounted Display System for Flight Simulation," SAE Aerospace Technical Conference and Exposition, Anaheim, California, September 25-28, 1989.

- [5] S.R. Stober, B. Welch, and R.V. Kruk, "The Fiber Optic Helmet Mounted Display," Proceedings of the Royal Aeronautical Society Conference, London, Spring 1984.

- [6] W.L. Polhemus and C.B. Langford, "The Integration of Helmet Mounted Sight and Display Systems with Automated Target Hand-Off Technology," NAECON '77 Record, 1977, pp. 962-967.
- [7] F.H. Raab, E.B. Blood, T.O. Steiner, and H.R. Jones, "Magnetic Position and Orientation Tracking System," IEEE Transactions on Aerospace and Electronic Systems, Vol. AES-15, No. 5, September 1979, pp. 709-718.
- [8] C.J.G. Lewis, "Helmet Mounted Display and Sight Development," Proceedings of the American Helicopter Society, May 1979, pp. 79.17.1-79.17.13.
- [9] C.J.G. Lewis, "Light Weight Solid State Helmet Symbol Display and Position System," Conference Proceedings of the Optics/Laser Society, October 1977, pp. 366-373.
- [10] M.D. Stephenson, "A Helmet-Mounted Sight Using C.C.D. Technology," The Radio and Electronic Engineer, Vol. 19, No. 10, October 1979, pp. 511-513.
- [11] A.I. Borisenko and I.E. Tarapov, Vector and Tensor Analysis with Applications, Prentice-Hall, Inc., 1968, pp. 45-46.

- [12] M. Jeger and B. Eckmann, Vector Geometry and Linear Algebra, John Wiley and Sons, 1967, pp. 161-163.
- [13] R.M. Rosenberg, Analytical Dynamics of Discrete Systems, Plenum Press, 1977, pp. 66-80.
- [14] H. Lowe, "Sensor Selection and Coordination," Proceedings of the Canadian Conference on Industrial Computer Systems, Ottawa, May 1984, pp. 87-1 - 87-6.
- [15] S. Larach, (Editor), Photoelectronic Materials and Devices, D. Van Nostrand Company, Inc., Princeton, 1965, pp. 100-108.
- [16] G.M. Glasford, Fundamentals of Television Engineering, McGraw-Hill Book Company Ltd., New York, 1955, pp. 108-116.
- [17] O.D. Faugeras, "A Few Steps Toward Artificial 3-D Vision," Robotics Science (Edited by M. Brady), The MIT Press, Cambridge, 1989, pp. 39-137.
- [18] T. Kanada, (Editor), Three-Dimensional Machine Vision, Part I: 3-D Sensors, Kluwer Academic Publishers, Boston, 1987, pp. 3-151.

- [19] D.H. Ballard, and C.W. Brown, Computer Vision, Prentice-Hall, Inc., Englewood Cliffs, New Jersey, 1982.
- [20] H.F.L. Pinkney, "Theory and Development of an On-Line 30 Hz Video Photogrammetry System for Real-Time 3-Dimensional Control," ISP Symposium on Photogrammetry for Industry, Stockholm, August 1978.
- [21] V. Kratky, "Real-Time Photogrammetric Support of Dynamic Three-Dimensional Control," Photogrammetric Engineering and Remote Sensing, Vol. 45, No. 9, September 1979, pp. 1231-1242.
- [22] N.R. Corby, "Machine Vision for Robotics," IEEE Transactions on Industrial Electronics, Vol. IE-30, No. 3, August 1983, pp. 282-291.
- [23] R. Dalven, Introduction to Applied Solid State Physics, Plenum Press, New York, 1980, pp. 188-190.
- [24] R.E. Walpole and R.H. Myers, Probability and Statistics for Engineers and Scientists, MacMillan Publishing Co., Inc., New York, 1972, pp. 95-98.

- [25] J.D.E. Beynon, and D.R. Lamb, (Editors), Charge-Coupled Devices and their Applications, McGraw-Hill Book Company Ltd., London, 1980, pp 80-116.
- [26] Fairchild Charge-Coupled Device (CCD) Catalog - 1989-90.
- [27] F.W. Sears, and M.W. Zemansky, University Physics (Fourth Edition), Addison-Wesley Publishing Company, Inc., Reading, Massachusetts, 1973, pp. 640.
- [28] S. Gage, D. Evans, M. Hodapp, and H. Sorensen, Optoelectronics Applications Manual, McGraw-Hill Book Company Ltd., New York, 1977, pp. 4.1 - 4.11.
- [29] A. Rose, Vision: Human and Electronic, Plenum Press, New York, 1973, pp. 72-77.
- [30] E.B. Brown, Modern Optics, Robert E. Krieger Publishing Company, Huntington, New York, 1974, pp. 256-257.
- [31] P.M. Chirlian, Analysis and Design of Integrated Electronic Circuits, Harper and Row, New York, 1987, pp. 68-72.

- [32] E.H. Williams, and R. Hall, Luminescence and the Light Emitting Diode, Pergamon Press, Oxford, 1978.
- [33] Y. Yakimovsky, and R. Cunningham, "A System for Extracting Three-Dimensional Measurements from a Stereo Pair of TV Cameras," Computer Graphics and Image Processing, Vol. 7, 1978, pp. 195-210.
- [34] N. Alvertos, D. Brzakovic, and R.C. Gonzalez, "Camera Geometries for Image Matching in 3-D Machine Vision," IEEE Transactions on Pattern Analysis and Machine Intelligence, Vol. 11, No. 9, September 1989, pp. 897-915.
- [35] L. Euler, "Formulae Generales pro Translatione Quacunque Corporum Rigidorum," Novi Commentari Acad. Imp. Petrop., Vol. 20, 1775, pp. 189-207.
- [36] J.W. Roach and J.K. Aggarwal, "Determining the Movement of Objects from a Sequence of Images," IEEE Transactions on Pattern Analysis and Machine Intelligence, Vol. 2, No. 6, November 1980, pp. 554-562.

- [37] D.W. Marquardt, "An Algorithm for Least-Squares Estimation of Nonlinear Parameters," J. SIAM, Vol. 11, No. 2, 1963, pp. 431-441.
- [38] K.M. Brown and J.E. Dennis, "Derivative Free Analogues of the Levenberg-Marquardt and Gauss Algorithms for Nonlinear Least Squares Approximation," Numer. Math., Vol. 18, 1972, pp. 289-297.
- [39] K.E. Bisshopp, "Rodrigues' Formula and the Screw Matrix," Journal of Engineering for Industry, Transactions of the ASME, 91(1): 1969, pp. 179-185.
- [40] O. Rodrigues, "Des lois géométriques qui régissent les déplacements d'un système solide dans l'espace, et de la variation des coordonnées provenant de ces déplacements indépendamment des causes qui peuvent les produire," Journal des Mathématiques Pures et Appliquées, Vol. 5, 1st. Series, 1840, pp. 380-440.
- [41] R.G. Fenton and X. Shi, "Comparison of Methods for Determining Screw Parameters of Finite Rigid Body Motion From Initial and Final Position Data," ASME Journal of Mechanical Design, Vol. 112, December 1990, pp. 472-479.

- [42] H. Cheng and K.C. Gupta, "An Historical Note on Finite Rotations," ASME Journal of Applied Mechanics, Vol. 56, March 1989, pp. 139-145.
- [43] J. Angeles, "Automatic Computation of the Screw Parameters of Rigid-Body Motions. Part I: Finitely-Separated Positions," ASME Journal of Dynamic Systems, Measurement, and Control, Vol. 108, March 1986, pp. 32-38.
- [44] F.H. Moffitt, Photogrammetry, International Textbook Company, Scranton, Pennsylvania, 1959, pp. 282-293.
- [45] E.H. Thompson, "An Exact Linear Solution of the Problem of Absolute Orientation," Photogrammetria, 15(4): 1959, pp. 163-179.
- [46] G.H. Schut, "On Exact Linear Equations for the Computation of the Rotational Elements of Absolute Orientation," Photogrammetria, 17(1): 1960, pp. 34-37.
- [47] G.H. Schut, Formation of Strips from Independent Models, AP-PR36, NRC-9695, Division of Physics, National Research Council of Canada, Ottawa, July 1967.

- [48] J.B. Lenox, Six Degree of Freedom Human Eyeball Movement Analysis Involving Stereometric Techniques, Ph.D. Thesis, Stanford University, Stanford, California, 1976.
- [49] N.H. McCoy, Fundamentals of Abstract Algebra, Allyn and Bacon, Inc., Boston, 1972, pp. 436-439.
- [50] R.A. Frazer, W.J. Duncan and A.R. Collar, Elementary Matrices and some Applications to Dynamics and Differential Equations, Cambridge University Press, London, 1938, pp. 35-36.
- [51] B. Hoffman, About Vectors, Prentice-Hall, Inc., Edgewood Cliffs, New Jersey, 1966, pp. 106-110.
- [52] N.R. Draper and H. Smith, Applied Regression Analysis (Second Edition), John Wiley and Sons, Inc., New York, 1981, pp. 85-87.
- [53] J. Angeles, "Rigid-Body Pose and Twist Estimation in the Presence of Noisy Redundant Measurements," Eight CISM-IFTOMM Symposium on Theory and Practice of Robots and Manipulators, Cracow, Poland, July 1990, pp. 71-78.

- [54] G.E. Forsythe and C.B. Moler, Computer Solution of Linear Algebraic Systems, Prentice-Hall Inc., Englewood Cliffs, 1967, pp. 16-26.
- [55] G.H. Golub and C. Van Loan, Matrix Computations, The Johns Hopkins University Press, Baltimore, 1983.
- [56] J.M. Ortega and W.C. Rheinboldt, Iterative Solution of Nonlinear Equations in Several Variables, Academic Press, Inc., New York, 1970, pp. 267-271.
- [57] A.T.J. Hayward, Repeatability and Accuracy, Mechanical Engineering Publications Ltd., 1977.
- [58] S.D. Stearns, A Portable Random Number Generator for Use in Signal Processing, Sandia National Laboratories Technical Report.
- [59] E. Kreyzig, Advanced Engineering Mathematics, John Wiley and Sons, Inc., 1972, pp. 779-781.
- [60] N. Krouglicof, M. McKinnon, and J. Svoboda, "The Design of a Non-Contact Position Sensing System," Proceedings of the 1986 Canadian Conference on Industrial Computer Systems, Montreal, 1986.

- [61] N. Krouglicof, M. McKinnon, and J. Svoboda, "Non-Contact Position and Orientation Measurement Techniques for Real-Time Systems," Proceedings of the 1986 ASME International Computers in Engineering Conference, Chicago, 1986.
- [62] M.A. Fischetti and C. Truxal (Editors), "Simulating 'The Right Stuff'," IEEE Spectrum, March 1985, pp. 38-47.
- [63] C.L. Hanson, "Fiber Optic Helmet Mounted Display: A Cost Effective Approach to Full Visual Flight Simulation," Proceedings of the Fifth Interservice/Industry Training Equipment Conference, November 1983, pp. 262-263.
- [64] N. Krouglicof, M. McKinnon, and J. Svoboda, Optical Position and Orientation Measurement Techniques, Canadian Patent 1 206 617 (June 24, 1986), U.S. Patent 4 649 504 (March 10, 1987).
- [65] N. Krouglicof and J. Svoboda, "Non-Contact Real Time Position Sensor Development for Robotic Applications," Proceedings of the Second Workshop on Military Robotic Applications, Kingston, 1989.

APPENDIX 1

MECHANICAL POSITION MEASUREMENT SYSTEM:

LISTING OF FORTRAN-86 ROUTINES

```

SUBROUTINE HELMET(HPOD,IPASS!)
*
*
* This subroutine reads the 6 angles of the Mechanical Helmet
* Position Sensor and computes the X-Y-Z position and direction
* cosines of the helmet with respect to the cockpit coordinate
* system. The cockpit coordinate system is oriented so that the
* positive X axis coincides with the forward longitudinal axis of
* the cockpit. The positive Y axis is parallel to the right wing
* and positive Z is down. This forms a right-handed coordinate
* system which follows the D.I.G. sign convention. Angle A is a
* positive rotation about the Z axis, B is a positive rotation
* about X, and C about Y. The subscripts 1, 2, and 3 refer to the
* three joints of the mechanism. Joint 1 is nearest to the helmet
* and has three degrees of freedom described by angles A1, B1, C1.
* Joint 2 is described by angles B2 and C2 and joint 3 by C3.
*
*
EXTERNAL ATOD
EXTERNAL DTOA
EXTERNAL DSPLY
*
INTEGER*2 HPOD(12)
INTEGER*2 IANGLE(6)
INTEGER*2 IDELA1(6), IDELC1(6), IOUT(4), IPASS1
*
IF (IPASS1 .EQ. 1) GOTO 10
IPASS1 = 1
*
POT = 14210.153
RVDT = 62582.27010
DEGRAD = 57.29577951
VB = 25.
VC = 17.25
*
10 CONTINUE
**
**
** CALL ATOD(IAngle)
**
**
IDELA1(6) = IDELA1(5)
IDELA1(5) = IDELA1(4)
IDELA1(4) = IDELA1(3)
IDELA1(3) = IDELA1(2)
IDELA1(2) = IDELA1(1)
IDELA1(1) = -IAngle(6)
*
IDELC1(6) = IDELC1(5)
IDELC1(5) = IDELC1(4)
IDELC1(4) = IDELC1(3)
IDELC1(3) = IDELC1(2)

```

```

      IDELC1(2) = IDELC1(1)
      IDELC1(1) = -IANGLE(4)
*
      IOUT(4) = IDELC1(6)
      IOUT(3) = IDELA1(5)
      IOUT(2) = IDELC1(6)
      IOUT(1) = IDELA1(5)
*
      CALL DTOA(IOUT)
*
      A1=FLOAT(-IANGLE(6))/POT
      B1=FLOAT(IANGLE(5))/POT
      C1=FLOAT(-IANGLE(4))/POT
      B2=FLOAT(-IANGLE(3))/RVDT
      C2=FLOAT(IANGLE(2))/RVDT
      C3=FLOAT(-IANGLE(1))/RVDT
*
*
      SINA1=SIN(A1)
      SINB1=SIN(B1)
      SINC1=SIN(C1)
      COSA1=COS(A1)
      COSB1=COS(B1)
      COSC1=COS(C1)
*
      SINB2=SIN(B2)
      SINC2=SIN(C2)
      COSB2=COS(B2)
      COSC2=COS(C2)
*
      SINC3=SIN(C3)
      COSC3=COS(C3)
*
*
      A11 = COSC1*COSA1
      A12 = COSC1*SINA1
      A13 = -SINC1
*
      A21 = SINB1*SINC1*COSA1 - COSB1*SINA1
      A22 = SINB1*SINC1*SINA1 + COSB1*COSA1
      A23 = SINB1*COSC1
*
      A31 = COSB1*SINC1*COSA1 + SINB1*SINA1
      A32 = COSB1*SINC1%*J*E - SINB1*COSA1
      A33 = COSB1*COSC1
*
      B11=COSC2
      B12=SINC2*SINB2
      B13=-SINC2*COSB2
*
      B21=0.
      B22=COSB2

```

```

*      B23=SINB2
*
*      B31=SINC2
*      B32=-COSC2*SINB2
*      B33=COSC2*COSB2
*
*      C11=COSC3
*      C12=0.
*      C13=-SINC3
*
*      C21=0.
*      C22=1.
*      C23=0.
*
*      C31=SINC3
*      C32=0.
*      C33=COSC3
*
*
*
*      AB11=A11*B11 + A12*B21 + A13*B31
*      AB12=A11*B12 + A12*B22 + A13*B32
*      AB13=A11*B13 + A12*B23 + A13*B33
*
*      AB21=A21*B11 + A22*B21 + A23*B31
*      AB22=A21*B12 + A22*B22 + A23*B32
*      AB23=A21*B13 + A22*B23 + A23*B33
*
*      AB31=A31*B11 + A32*B21 + A33*B31
*      AB32=A31*B12 + A32*B22 + A33*B32
*      AB33=A31*B13 + A32*B23 + A33*B33
*
*
*
*      ABC11=AB11*C11 + AB12*C21 + AB13*C31
*      ABC12=AB11*C12 + AB12*C22 + AB13*C32
*      ABC13=AB11*C13 + AB12*C23 + AB13*C33
*
*      ABC21=AB21*C11 + AB22*C21 + AB23*C31
*      ABC22=AB21*C12 + AB22*C22 + AB23*C32
*      ABC23=AB21*C13 + AB22*C23 + AB23*C33
*
*      ABC31=AB31*C11 + AB32*C21 + AB33*C31
*      ABC32=AB31*C12 + AB32*C22 + AB33*C32
*      ABC33=AB31*C13 + AB32*C23 + AB33*C33
*
*
*      Store Helmet Position and Orientation Data in array
*      HPOD(12) in the order X, Y, Z, ABC11, ABC12, ABC13,
*      ABC21, ABC22, ABC23, ABC31, ABC32, ABC33 for transmission
*      to the SEL.
*
*      REHPOD = VC*COSC3 + VB*(SINC2*COSC3 + COSC2*COSB2*SINC3) - VC
*      HPOD(1) = NINT(REHPOD*1000.)
*      REHPOD = -VB*COSC2*SINB2

```

```

      HPOD(2) = NINT(REHPOD*1000.)
      REHPOD = -VC*SINC3 - VB*(SINC2*SINC3 - COSC2*COSB2*COSC3) - VB
      HPOD(3) = NINT(REHPOD*1000.)
*
      HPOD(4) = NINT(ABC11*32752)
      HPOD(5) = NINT(ABC12*32752)
      HPOD(6) = NINT(ABC13*32752)
*
      HPOD(7) = NINT(ABC21*32752)
      HPOD(8) = NINT(ABC22*32752)
      HPOD(9) = NINT(ABC23*32752)
*
      HPOD(10) = NINT(ABC31*32752)
      HPOD(11) = NINT(ABC32*32752)
      HPOD(12) = NINT(ABC33*32752)
*
      RETURN
      END

```

APPENDIX 2

CALIBRATION OF POSITION SENSOR HEAD:

MAP OF THE SENSITIVE SURFACE

Conditions:

- 1.) Sensor Model Number: Hamamatsu C1454-05
(serial #81054767)
- 2.) Intensity of Light Spot: $\Sigma = 5.000 \text{ V}$.
- 3.) No Background Illumination.

Table A2.1: X Output Voltage Signal recorded at 1 mm intervals across detector surface.

X	5.000	4.000	3.000	2.000	1.000	0.000	-1.000	-2.000	-3.000	-4.000	-5.000
Y	5.108	5.124	5.113	5.128	5.123	5.111	5.118	5.103	5.101	5.093	5.093
	4.082	4.082	4.081	4.090	4.090	4.087	4.089	4.085	4.082	4.065	4.059
	3.058	3.061	3.056	3.061	3.062	3.057	3.058	3.054	3.054	3.039	3.031
	2.026	2.031	2.026	2.036	2.043	2.041	2.035	2.020	2.018	2.010	2.007
	1.014	1.014	1.009	1.007	1.014	1.010	1.009	0.999	0.990	0.983	0.983
	0.007	0.003	0.004	0.001	0.007	0.001	-0.006	-0.006	-0.015	-0.025	-0.032
	-1.021	-1.032	-1.020	-1.019	-1.006	-1.012	-1.022	-1.027	-1.027	-1.034	-1.043
	-2.025	-2.035	-2.042	-2.036	-2.030	-2.031	-2.039	-2.038	-2.042	-2.045	-2.046
	-3.023	-3.033	-3.048	-3.054	-3.047	-3.041	-3.044	-3.054	-3.051	-3.060	-3.053
	-4.033	-4.040	-4.044	-4.050	-4.049	-4.049	-4.052	-4.060	-4.056	-4.062	-4.060
	-5.016	-5.031	-5.030	-5.029	-5.034	-5.033	-5.048	-5.050	-5.047	-5.055	-5.053

Table A2.2: Y Output Voltage Signal recorded at 1 mm intervals across detector surface.

X	5.000	4.000	3.000	2.000	1.000	0.000	-1.000	-2.000	-3.000	-4.000	-5.000
Y	5.066	5.065	5.070	5.064	5.072	5.070	5.069	5.068	5.066	5.071	5.079
	4.088	4.084	4.090	4.085	4.096	4.093	4.097	4.092	4.085	4.094	4.099
	3.072	3.067	3.071	3.069	3.079	3.074	3.073	3.072	3.066	3.072	3.075
	2.044	2.044	2.045	2.047	2.055	2.049	2.044	2.047	2.047	2.048	2.046
	1.022	1.023	1.022	1.017	1.030	1.022	1.016	1.012	1.018	1.026	1.030
	0.006	0.011	0.010	0.003	0.014	0.006	0.001	0.006	-0.010	-0.005	0.000
	-1.010	-1.002	-1.002	-1.016	-1.007	-1.005	-1.009	-1.023	-1.027	-1.019	-1.017
	-2.023	-2.022	-2.026	-2.038	-2.026	-2.027	-2.024	-2.038	-2.038	-2.031	-2.037
	-3.046	-3.044	-3.044	-3.050	-3.044	-3.050	-3.048	-3.048	-3.047	-3.040	-3.046
	-4.054	-4.062	-4.060	-4.063	-4.051	-4.056	-4.063	-4.058	-4.058	-4.055	-4.057
	-5.074	-5.076	-5.073	-5.079	-5.067	-5.070	-5.068	-5.075	-5.077	-5.073	-5.067

APPENDIX 3

**INTENSITY CONTROL CIRCUIT:
LISTING OF MIMIC SIMULATION PROGRAM**

```

CON(VSAT, VT, K)
CON(RS, VCC, VJ)
CON(Q, PI)
CON(AP, TRANS, RE)
CON(TAUD, K3, K2)
CON(KI, TAU1, SP)
CON(TAUC)
CON(STEPS)
CON(TERM)
CON(GAIN)
PAR(R)

C
C MOSFET off (i.e. VGS < VT)
C
      OFF      FSW(VGS-VT, TRUE, TRUE, FALSE)
      NOTOFF   NOT(OFF)

C
OFF      VDS      =VCC
OFF      IF       =0.

C
C MOSFET operating below saturation (i.e. VGS > VSAT)
C
      BELOW    FSW(VGS-VSAT, FALSE, FALSE, TRUE)
      NOTBEL   NOT(BELOW)

C
BELOW    B        =-2.*(VGS-VT) - (1./(K*RS))
BELOW    C        =(VCC-VJ) / (K*RS)
BELOW    VDS      =(-B-SQR((B*B)-(4.*C))) / 2.
BELOW    IF       =(VCC-VDS-VJ) / RS

C
C MOSFET operating above saturation (i.e. VT < VGS < VSAT)
C
      ABOVE    AND(NOTBEL, NOTOFF)
      ABOVE    VDS      =VCC - VJ - (RS*K*(VGS-VT)*(VGS-VT))
      ABOVE    IF       =(VCC-VDS-VJ) / RS

C
C Calculate total radiant flux emitted from L.E.D.
C
      PHIE     =Q*IF

C
C Based on the geometry, compute the radiant flux incident
C on the sensitive surface of the P.S.D.
C
      ER       =PHIE / (2.*PI*R*R)
      PHIS     =ER*AP*TRANS
      IP       =INT((RE*PHIS-IP)/TAUD, 0.)
      SIGMA    =INT((2.0*K3*K2*KI*IP-SIGMA)/TAU1, 0.)

C
C Determine the control voltage, VGS, based on the error
C between the set point, SP, and the feedback, SIGMA.
C Include the dynamics of the Operational Amplifier.
C
      ERROR    =SP-SIGMA

```

```

C      VHIGH      =FSW (VGS-12.0,FALSE,TRUE,TRUE)
      VLOW        =FSW (VGS+12.0,TRUE,TRUE,FALSE)
      VNORM       =AND (NOT(VHIGH),NOT(VLOW))

C      POSERR     =FSW (ERROR,FALSE,TRUE,TRUE)
      NEGERR      =NOT (POSERR)

C      INTUP      =AND (VLOW,POSERR)
      INTDWN      =AND (VHIGH,NEGERR)
      ENINT       =IOR (INTUP,INTDWN,VNORM)
      DISINT      =NOT (ENINT)

C      ENINT      AA      =(GAIN*ERROR-VGS) /TAUC
      DISINT      AA      =0.

C      VGS        =0.8*INT(AA,7.3953929)

C      OUT (T,SIGMA,VGS,IF)
C ***      PLO (T,SIGMA)
C
      DTMAX       =STEPS
      DTMIN       =DTMAX
      DT          =STEPS*50.
      FIN (T,TERM)
      END

5.287978      3.0      1.777
0.16          5.0      1.223
0.05          3.141592654
7.853980E-050.5      0.52
10.47000E-060.47      20.0
1.000000E+052.200000E-063.5
0.3
+1.00000E-07
+2.95000E-04
3000.
1.080695
1.0969464
1.1131978

```

APPENDIX 4

OPTICAL POSITION MEASUREMENT SYSTEM: STATISTICAL SIMULATION PROGRAM

```

1      PROGRAM IMAGE
2      *
3      IMPLICIT DOUBLE PRECISION(A-H,O-Z)
4      *
5      INTEGER FREQY(101),FREQR(101),FREQP(101)
6      DIMENSION PX0(6), PY0(6), PZ0(6)
7      DIMENSION PX(6), PY(6), PZ(6)
8      DIMENSION XD1(6), YD1(6), XD2(6), YD2(6)
9      DIMENSION XM1(6), YM1(6), XM2(6), YM2(6)
10     *
11     EXTERNAL SCHUT
12     OPEN (50,FILE='HIST.DAT',STATUS='NEW')
13     *
14     PI = 2.0*DASIN(0.1D1)
15     DEGRAD = 180.0 / PI
16     THETA = 35.5 / DEGRAD
17     CTHETA = DCOS(THETA)
18     STHETA = DSIN(THETA)
19     D = 1.274
20     RSQ = D / (2.0*STHETA)
21     FE = 16.264535
22     NN = 1500
23     NBIT = 9
24     SEED=1
25     CALL RANDOM(SEED,RNUMB)
26     *
27     ***      WRITE(*,*) 'ENTER ANGLES A, B, C'
28     ***      READ(*,*) A, B, C
29     *
30     WRITE(50,*) ' STANDARD ERROR IN YAW, ROLL, PITCH '
31     WRITE(50,*) ' '
32     *
33     A = 0.
34     B = 0.
35     C = 0.
36     *
37     A = A / DEGRAD
38     B = B / DEGRAD
39     C = C / DEGRAD
40     *
41     DO 70 N=3, 6, 1
42     *
43     DO 90 I=1,100
44     FREQY(I)=0
45     FREQR(I)=0
46     FREQP(I)=0
47 90    CONTINUE
48     *
49     *
50     * Define the initial state coordinates
51     *
52     ***      R = 0.1 * DSIN(PI/3.0)
53     R = 0.0762

```

```

54 *
55     PX0(1) = -R / 2.0
56     PX0(2) = R
57     PX0(3) = -R / 2.0
58     PX0(4) = R / 2.0
59     PX0(5) = -R
60     PX0(6) = R / 2.0
61 *
62     PY0(1) = R * DSIN(PI/3.0)
63     PY0(2) = 0.0
64     PY0(3) = -R * DSIN(PI/3.0)
65     PY0(4) = R * DSIN(PI/3.0)
66     PY0(5) = 0.0
67     PY0(6) = -R * DSIN(PI/3.0)
68 *
69     PZ0(1) = 0.0
70     PZ0(2) = 0.0
71     PZ0(3) = 0.0
72     PZ0(4) = 0.0
73     PZ0(5) = 0.0
74     PZ0(6) = 0.0
75 *
76     A11 = DCOS(C)*DCOS(A)
77     A12 = DCOS(C)*DSIN(A)
78     A13 = -DSIN(C)
79 *
80     A21 = DSIN(B)*DSIN(C)*DCOS(A) - DCOS(B)*DSIN(A)
81     A22 = DSIN(B)*DSIN(C)*DSIN(A) + DCOS(B)*DCOS(A)
82     A23 = DSIN(B)*DCOS(C)
83 *
84     A31 = DCOS(B)*DSIN(C)*DCOS(A) + DSIN(B)*DSIN(A)
85     A32 = DCOS(B)*DSIN(C)*DSIN(A) - DSIN(B)*DCOS(A)
86     A33 = DCOS(B)*DCOS(C)
87 *
88     DO 10 I=1, N, 1
89     PX(I) = A11*PX0(I) + A21*PY0(I) + A31*PZ0(I)
90     PY(I) = A12*PX0(I) + A22*PY0(I) + A32*PZ0(I)
91     PZ(I) = A13*PX0(I) + A23*PY0(I) + A33*PZ0(I)
92 10 CONTINUE
93 *
94 * Calculate the image coordinates of the points with
95 * respect to Sensor 1 and Sensor 2.
96 *
97     DO 20 I=1, N, 1
98     RX1 = CTHETA*PX(I) + STHETA*PZ(I)
99     RY1 = PY(I)
100    RZ1 = -STHETA*PX(I) + CTHETA*PZ(I) + RSQ
101 *
102    RMAG1 = DSQRT(RX1*RX1 + RY1*RY1 + RZ1*RZ1)
103 *
104    COSA1 = RX1 / RMAG1
105    COSB1 = RY1 / RMAG1
106    COSC1 = RZ1 / RMAG1

```

```

107 *
108     RD1 = FE / COSC1
109     XD1(I) = RD1 * COSA1
110     YD1(I) = RD1 * COSB1
111 *
112     RX2 = CTHETA*PX(I) - STHETA*PZ(I)
113     RY2 = PY(I)
114     RZ2 = STHETA*PX(I) + CTHETA*PZ(I) + RSQ
115 *
116     RMAG2 = DSQRT(RX2*RX2 + RY2*RY2 + RZ2*RZ2)
117 *
118     COSA2 = RX2 / RMAG2
119     COSB2 = RY2 / RMAG2
120     COSC2 = RZ2 / RMAG2
121 *
122     RD2 = FE / COSC2
123     XD2(I) = RD2 * COSA2
124     YD2(I) = RD2 * COSB2
125 *
126 ***   WRITE(50,2000) I, XD1(I), YD1(I), XD2(I), YD2(I)
127 2000   FORMAT(' Point ', I1, 4X, 4F12.7)
128 20     CONTINUE
129 *
130 *     If the pattern is not symmetric (i.e. N=4 or N=5)
131 *     compute the new origin of the body coordinate system.
132 *
133     IF (N.EQ.4 .OR. N.EQ.5) THEN
134         QX0 = 0.
135         QY0 = 0.
136         QZ0 = 0.
137         DO 30 I=1, N, 1
138             QX0 = QX0 + PX0(I)
139             QY0 = QY0 + PY0(I)
140             QZ0 = QZ0 + PZ0(I)
141 30     CONTINUE
142         QX0 = QX0 / N
143         QY0 = QY0 / N
144         QZ0 = QZ0 / N
145         DO 40 I=1, N, 1
146             PX0(I) = PX0(I) - QX0
147             PY0(I) = PY0(I) - QY0
148             PZ0(I) = PZ0(I) - QZ0
149 40     CONTINUE
150     ENDIF
151 *
152     SUMY = 0.
153     SUMY2 = 0.
154 *
155     SUMR = 0.
156     SUMR2 = 0.
157 *
158     SUMP = 0.
159     SUMP2 = 0.

```

```

160 *
161      DO 60 J=1, NN, 1
162 *
163      DO 50 I=1, N, 1
164          XM1(I) = XD1(I) + RERR(NBIT)
165          YM1(I) = YD1(I) + RERR(NBIT)
166          XM2(I) = XD2(I) + RERR(NBIT)
167          YM2(I) = YD2(I) + RERR(NBIT)
168 50      CONTINUE
169 *
170          CALL SCHUT(N,PX0,PY0,PZ0,XM1,YM1,XM2,YM2,
171      + YAW,ROLL,PITCH)
172 *
173 ***          WRITE(50,3000) YAW, ROLL, PITCH
174 3000  FORMAT(' YAW = ',F12.7,' ROLL = ',F12.7,' PITCH = ',F12.7)
175 *
176          SUMY = SUMY + YAW
177          SUMY2 = SUMY2 + YAW*YAW
178          IND = 50+DINT(50*YAW)
179          IF (YAW.GT.0) IND=IND+1
180          FREQY(IND) = FREQY(IND)+1
181 *
182          SUMR = SUMR + ROLL
183          SUMR2 = SUMR2 + ROLL*ROLL
184          IND = 50+DINT(50*ROLL)
185          IF (ROLL.GT.0) IND=IND+1
186          FREQR(IND) = FREQR(IND)+1
187 *
188          SUMP = SUMP + PITCH
189          SUMP2 = SUMP2 + PITCH*PITCH
190          IND = 50+DINT(50*PITCH)
191          IF (PITCH.GT.0) IND=IND+1
192          FREQP(IND) = FREQP(IND)+1
193 *
194 60      CONTINUE
195 *
196          VARY = (FLOAT(NN)*SUMY2 - SUMY*SUMY) / (FLOAT(NN)*FLOAT(NN-1))
197          SEY = DSQRT(VARY)
198          AVGY = SUMY / FLOAT(NN)
199 *
200          VARR = (FLOAT(NN)*SUMR2 - SUMR*SUMR) / (FLOAT(NN)*FLOAT(NN-1))
201          SER = DSQRT(VARR)
202          AVGR = SUMR / FLOAT(NN)
203 *
204          VARP = (FLOAT(NN)*SUMP2 - SUMP*SUMP) / (FLOAT(NN)*FLOAT(NN-1))
205          SEP = DSQRT(VARP)
206          AVGP = SUMP / FLOAT(NN)
207 *
208          WRITE(*,4000) N, SEY, SER, SEP
209          WRITE(50,4000) N, SEY, SER, SEP
210          WRITE(50,4000) N, AVGY, AVGR, AVGP
211 4000  FORMAT(5X,/, ' # OF POINTS= ', I1, 1X, 3F10.7, /)
212 *

```



```

213      DO 200 I=1,101
214      XLAN=(FLOAT(I)-51.)/50.
215      WRITE(50,5000) XLAN,FREQY(I),FREQR(I),FREQP(I)
216 5000  FORMAT(F6.3, 4I10)
217 200   CONTINUE
218 *
219 70    CONTINUE
220 *
221      STOP
222      END

223 *
224      DOUBLE PRECISION FUNCTION RERR(NBIT)
225      CALL RANDOM(SEED,RNUMB)
226      RANGE = 10.0 / (2.0**NBIT)
227      RERR = RANGE * (RNUMB-0.5)
228      RETURN
229      END

230 *
231      SUBROUTINE RANDOM(SEED, RANDX)
232 *
233 * This subroutine generates random values between 0.0 and 1.0
234 * using an integer seed
235 *
236      INTEGER SEED
237      REAL RANDX
238      SEED=2045*SEED+1
239      SEED=SEED-(SEED/1048576)*1048576
240      RANDX=REAL(SEED+1)/1048577.0
241      RETURN
242      END

```

```

1      SUBROUTINE SCHUT(N,PX0,PY0,PZ0,XD1,YD1,XD2,YD2,
2      + YAW,ROLL,PITCH)
3      *
4      IMPLICIT DOUBLE PRECISION (A-H,O-Z)
5      *
6      DIMENSION PX0(N), PY0(N), PZ0(N)
7      DIMENSION XD1(N), YD1(N), XD2(N), YD2(N)
8      *
9      DIMENSION PX(6), PY(6), PZ(6)
10     *
11     PI = 2.0*DASIN(0.1D1)
12     DEGRAD = 180.0 / PI
13     THETA = 35.5 / DEGRAD
14     CTHETA = DCOS(THETA)
15     STHETA = DSIN(THETA)
16     D = 1.274
17     FE = 16.264535
18     *
19     DO 10 I=1, N, 1
20     *
21     * Compute direction cosines of vector joining l.e.d. and PSH 1.
22     *
23     RD = DSQRT(FE*FE + XD1(I)*XD1(I) + YD1(I)*YD1(I))
24     COSAI = XD1(I) / RD
25     COSBI = YD1(I) / RD
26     COSCI = FE / RD
27     *
28     COSA1 = COSAI*CTHETA - COSCI*STHETA
29     COSB1 = COSBI
30     COSC1 = COSAI*STHETA + COSCI*CTHETA
31     *
32     * Compute direction cosines of vector joining l.e.d. and PSH 2.
33     *
34     RD = DSQRT(FE*FE + XD2(I)*XD2(I) + YD2(I)*YD2(I))
35     COSAI = XD2(I) / RD
36     COSBI = YD2(I) / RD
37     COSCI = FE / RD
38     *
39     COSA2 = COSAI*CTHETA + COSCI*STHETA
40     COSB2 = COSBI
41     COSC2 = -COSAI*STHETA + COSCI*CTHETA
42     *
43     R1 = (D*COSC2) / (COSA2*COSC1 - COSA1*COSC2)
44     *
45     PX(I) = R1*COSA1
46     PY(I) = R1*COSB1
47     PZ(I) = R1*COSC1
48     *
49 10    CONTINUE
50     *
51     * Calculate the Three-Dimensional mean of the measured points
52     *

```

```

53      QX = 0.
54      QY = 0.
55      QZ = 0.
56 *
57      DO 50 I=1, N, 1
58      QX = QX + PX(I)
59      QY = QY + PY(I)
60      QZ = QZ + PZ(I)
61 50    CONTINUE
62 *
63 *   The point Q is the origin of the body coordinate system
64 *
65      QX = QX / FLOAT(N)
66      QY = QY / FLOAT(N)
67      QZ = QZ / FLOAT(N)
68 *
69 *   Redefine PX, PY, PZ as the components of the vector joining
70 *   Q and P
71      DO 60 I=1, N, 1
72      PX(I) = PX(I) - QX
73      PY(I) = PY(I) - QY
74      PZ(I) = PZ(I) - QZ
75 60    CONTINUE
76 *
77 *   Set the elements of the S matrix to zero.
78 *
79      S12 = 0.
80      S13 = 0.
81      S23 = 0.
82      S14 = 0.
83      S24 = 0.
84      S34 = 0.
85      S11 = 0.
86      S22 = 0.
87      S33 = 0.
88      S44 = 0.
89 *
90      DO 70 I=1, N, 1
91      S12 = S12 + PY(I)*PX0(I) + PY0(I)*PX(I)
92      S13 = S13 + PX(I)*PZ0(I) + PX0(I)*PZ(I)
93      S23 = S23 + PZ(I)*PY0(I) + PZ0(I)*PY(I)
94      S14 = S14 + PZ(I)*PY0(I) - PZ0(I)*PY(I)
95      S24 = S24 + PX(I)*PZ0(I) - PX0(I)*PZ(I)
96      S34 = S34 + PY(I)*PX0(I) - PY0(I)*PX(I)
97 *
98      S11 = S11 + (PX0(I)-PX(I))**2 + (PY0(I)+PY(I))**2
99      +      + (PZ0(I)+PZ(I))**2
100     S22 = S22 + (PX0(I)+PX(I))**2 + (PY0(I)-PY(I))**2
101     +      + (PZ0(I)+PZ(I))**2
102     S33 = S33 + (PX0(I)+PX(I))**2 + (PY0(I)+PY(I))**2
103     +      + (PZ0(I)-PZ(I))**2
104
104     S44 = S44 + (PX0(I)-PX(I))**2 + (PY0(I)-PY(I))**2

```

```

105      +      + (PZ0(I)-PZ(I))**2
106 70    CONTINUE
107 *
108      S12 = -2.*S12
109      S13 = -2.*S13
110      S23 = -2.*S23
111      S14 = 2.*S14
112      S24 = 2.*S24
113      S34 = 2.*S34
114 *
115      SP22 = S22 - (S12*S12)/S11
116      SP23 = S23 - (S13*S12)/S11
117      SP24 = S24 - (S14*S12)/S11
118      SP33 = S33 - (S13*S13)/S11 - (SP23*SP23)/SP22
119      SP34 = S34 - (S14*S13)/S11 - (SP24*SP23)/SP22
120      SP44 = S44 - (S14*S14)/S11 - (SP24*SP24)/SP22
121 *
122      ROW3 = SP34 / SP33
123      ROW2 = (SP24 - SP23*ROW3) / SP22
124      ROW1 = (S14 - S13*ROW3 - S12*ROW2) / S11
125 *
126      DENO = 1. + ROW1**2 + ROW2**2 + ROW3**2
127 *
128      T12 = 2.*(ROW1*ROW2 + ROW3) / DENO
129      T11 = (1. + ROW1**2 - ROW2**2 - ROW3**2) / DENO
130      T23 = 2.*(ROW2*ROW3 + ROW1) / DENO
131      T33 = (1. + ROW3**2 - ROW1**2 - ROW2**2) / DENO
132      T13 = 2.*(ROW3*ROW1 - ROW2) / DENO
133 *
134      YAW  = DATAN2(T12, T11) * DEGRAD
135      ROLL = DATAN2(T23, T33) * DEGRAD
136      PITCH = DASIN(-T13) * DEGRAD
137 *
138      RETURN
139      END

```

APPENDIX 5

OPTICAL POSITION MEASUREMENT SYSTEM:

SAMPLE CALIBRATION DATA

ACTUAL ANGLE	YAW 6 LEDs	YAW 5 LEDs	YAW 4 LEDs	YAW 3 LEDs	ROLL 6 LEDs	PITCH 6 LEDs
0°	-0.04°	0.01°	0.03°	-0.03°	0.2°	-0.05°
0°	-0.06°	0.1°	-0.02°	-0.04°	0.02°	0.03°
0°	0.08°	-0.06°	0.05°	-0.22°	-0.05°	-0.2°
0°	-0.04°	0°	-0.01°	-0.11°	0.04°	-0.06°
0°	0.03°	-0.02°	-0.07°	0.07°	0.08°	-0.19°
0°	-0.07°	-0.05°	-0.16°	0.01°	0.26°	-0.09°
0°	-0.02°	-0.04°	0.03°	-0.1°	-0.01°	-0.04°
0°	0.08°	0.06°	-0.09°	0.06°	0.16°	-0.1°
0°	-0.04°	-0.11°	0.01°	-0.01°	0.19°	0.13°
0°	0.06°	0.02°	0.02°	-0.05°	0.1°	-0.09°
15°	14.9°	14.85°	14.83°	15.09°	15.41°	14.73°
15°	14.94°	14.83°	14.81°	15.16°	15.23°	14.77°
15°	14.89°	14.72°	14.95°	15.04°	15.31°	14.93°
15°	15.07°	14.79°	14.91°	15.08°	15.29°	14.59°
15°	14.92°	14.96°	14.93°	14.98°	15.32°	14.75°
15°	14.94°	14.79°	14.98°	15.1°	15.24°	14.77°
15°	14.98°	14.78°	14.82°	14.99°	15.07°	14.57°
15°	15.01°	14.84°	14.87°	15.1°	15.11°	14.79°
15°	14.87°	14.73°	14.92°	15.12°	15.15°	14.58°